ALMA MATER STUDIORUM · UNIVERSITY OF BOLOGNA

School of Science

Department of Physics and Astronomy
Master Degree in Physics

Study of bent Monolithic Active Pixel Sensors for the ALICE Inner Tracking System 3

Master Thesis in Physics

Supervisor:
Prof. Gilda Scioli

Co-Supervisor:
Dr. Francesca Carnesecchi

Submitted by:
Riccardo Ricci

Academic Year 2020/2021

I miei passi diventano pensieri,
e i pensieri diventano Qualcuno,
diventano te Padre, grande e buono,
che per amore hai cominciato il gioco!

Non lasciare che un giorno me ne vada,
dammi sempre la forza di lottare,
è ancora molto lunga questa strada
e ho ancora tanta voglia di cantare!

Claudio Chieffo, *Canzone per te*

A Enrico, Matilde ed Elena

Contents

Abstract

The ALICE experiment at CERN has planned an upgrade of the Inner Tracking System (ITS), named ITS3, for the LHC Long Shutdown 3, in 2025. The cornerstone of the upgrade is a new CMOS pixel sensor built in 65 nm technology and in bent-cylindrical configuration, replacing the inner layers of the existing detector, the ITS2. The ITS3 will reach much better tracking and vertexing performance, thanks to the improved spatial resolution and the much reduced material budget with respect to the previous Inner Tracking System.

The aim of this thesis is to report on the analysis of the data collected at beam tests on new ALPIDE chips (used for ITS2, based on Monolithic Active Pixel Sensor, MAPS) which have been bent in a cylindrical configuration as foreseen for the ITS3. This is the first bending proof of concept for a silicon detector.

In particular, data from beam test taken in 2020 have been studied through a data analysis framework that I have personally written to accomplish this task; the complexity of the data analysis is driven by the fact that each ALPIDE chip has a total of 1024x512 pixel MAPS and by the bent geometry of the sensor.

In this thesis, the promising performances obtained by studying the sensor total efficiency and spatial resolution in different experimental configurations will be presented and discussed.

Introduction

ALICE (A Large Ion Collider Experiment) is one of the major experiments of the Large Hadron Collider (LHC) at CERN. It has been built to study the ultra relativistic heavy-ion collisions; indeed at high energy density or temperature the formation of the Quark Gluon Plasma (QGP) is expected. The ALICE detector was designed to deal with events at very high levels of multiplicity of particles, with a high power PID capability that spans from 20 GeV/c down to very low transverse momentum ($\sim$0.1 GeV/c) thanks to the low material budget. During LHC Long Shutdown 2 (LHC LS2), ALICE has realized a major upgrade, including the upgrade of its Inner Tracking System (ITS) with ITS2, radically increasing tracking and vertexing performance, mainly thanks to the CMOS-180 nm MAPS sensors (ALPIDE) used. In addition, the ALICE collaboration has planned to carry out a further upgrade of the three innermost layers of the ITS2, called ITS3, scheduled for LHC LS3 in 2025.
This upgrade is revolutionary in the field of particle detection, as it will implement for the first time a bent geometry tracker, trulycurved around the beam pipe. This new configuration will drastically reduce the material budget, get even closer to the Interaction Point (IP) and reduce the pixel pitch, dramatically increasing the detector's performance thanks to improved impact parameter resolution and tracking efficiency. In particular, the replaced three innermost layers will be placed at a distance from the IP of 18,23 and 30 mm, respectively. The cornerstone of this upgrade will be a silicon CMOS pixel sensor based on the MAPS (Monolithic Active Pixel Sensors) using a 65 nm technology from Towerjazz.

In this thesis work the ALPIDE has been studied in a bent configuration in a beam test carried at DESY in August 2020. The sensor has been bent down to a radius of R = 18 mm, corresponding to the distance of the innermost layer of ITS3. The chip performance have been determined mainly by studying its detection efficiency and spatial resolution.
In the first chapter, the ALICE LHC detector and the operation of ITS2 are briefly presented, together with an explanation of the operation of the MAPS technology used for the ITS2 pixel sensors.
The second chapter discusses the reasons for an additional upgrade of the ITS, illustrating the technical limitations of ITS2 and the benefits of upgrading to ITS3 in terms

of increased tracking and physics performance. Finally, the ITS3 structure will be described in detail.
In the third and fourth chapters the data analysis work of the ALPIDE chip in bent configuration is introduced. In particular, in the third chapter the Corryvreckan framework will be introduced: the framework has been used for the production of the first graphs from raw data. The graphs that have been used to perform the data analysis will be presented. In the first part of Chapter 4, the experimental setup will be presented, with the methods used to carry out the analysis. Firstly, the changes to the setup in the transition to the bent geometry will be presented with the related code description modifications on the code of the Corryvreckan analysis framework. In the second part, the results of the data analysis carried out in terms of efficiency performance and spatial resolution will be presented.

Chapter 1

The ALICE Inner Tracking System

ALICE (A Large Ion Collider Experiment) is an experiment at the LHC (Large Hadron Collider) optimized to study the Quark-Gluon Plasma (QGP), a state of deconfined quarks and gluons created at energy densities higher than 1GeV/fm^3, as predicted by Quantum Chromo Dynamics (QCD), the theory of strong interactions. Such high energy densities can be reached via high-energy Pb-Pb collisions; the QGP fireball is created and it immediately starts to expand, thermalize and cool down. This state of matter has been produced in the early universe, few μs after the Big Bang. [1].

The ALICE detector has been designed to cope with events with high particle multiplicity, as expected for such collisions. To fully exploit the physics possibilities of these studies it is fundamental to maximize the Particle IDentification (PID) capabilities of the detectors and, to this purpose, ALICE makes use of almost all known PID techniques that allow a comprehensive study of hadrons, muons, electrons and photons produced in the collision, down to very low transverse momentum, thanks to the low material budget.[2].

1.1 LHC - the Large Hadron Collider

The LHC is the world's largest and most powerful particle accelerator and is located at CERN (European Organization for Nuclear Research), near Geneva. The LHC facility consists of an underground ring 26.7 kilometers long in which protons or heavy-ion beams collide going in opposite directions in two separate ultrahigh-vacuum beam pipes. The collider is made of superconducting magnets, in particular almost 1200 dipole magnets for beam bending and 392 quadrupole ones, used for beam focusing.

In Figure 1.1 the full accelerator structure is shown. In the LHC protons and nuclei can be accelerated and collide at center of mass energies up to $\sqrt{s}$ = 13 TeV for pp collisions and $\sqrt{s_{NN}}$ = 5.02 TeV per Pb-Pb nucleons pair.

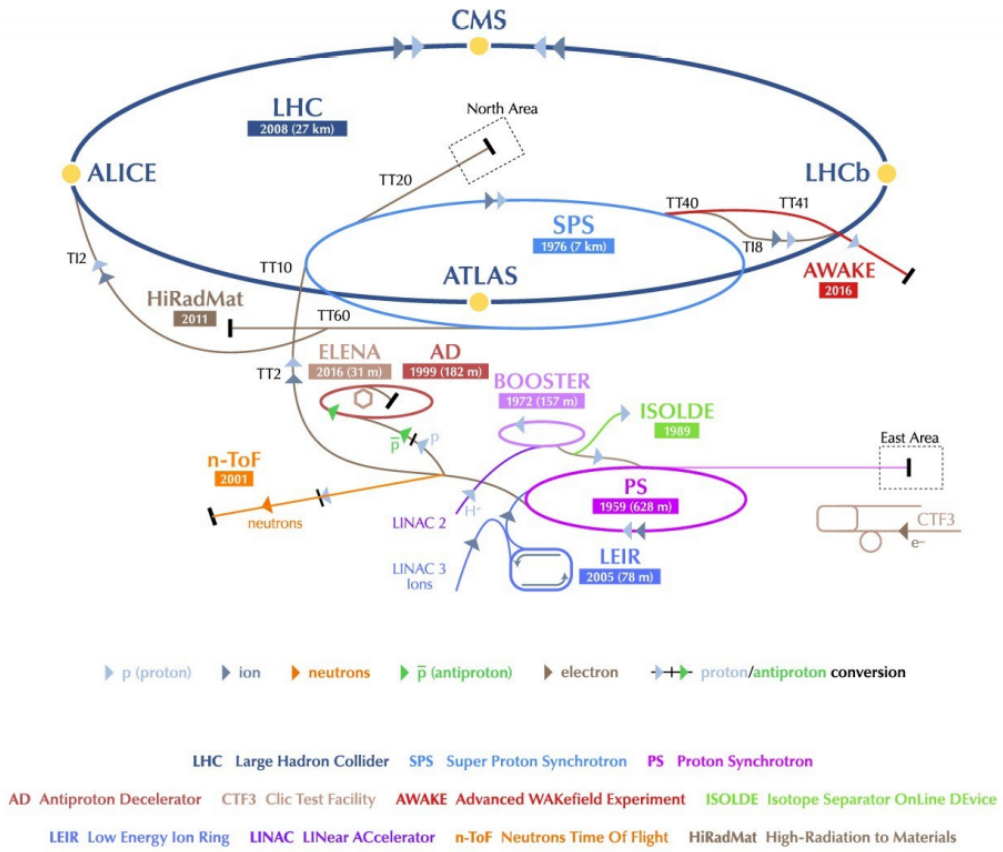

Figure 1.1: CERN accelerators complete view. The four main LHC experiments (ALICE, ATLAS, CMS, LHCb) and other experimental facilities are illustrated.

1.2 The QGP Quark-Gluon Plasma

The QCD describes the strongly interacting matter at a fundamental level thanks to the interaction of quarks via gluons exchange. The relative coupling constant $\alpha_S(q^2)$ follows a logarithmic decrease for short radius or high momentum (q) values and increases for large distances or small momentum values: this behavior causes the **quark confinement** and chiral symmetry breaking.

In Figure 1.2 the QCD phase diagram is shown. The diagram describes the different possible phases of the strongly interacting matter versus the temperature T and the baryo-chemical potential. The latter is defined as the energy necessary to increase the total number of baryons N_B of the system by 1:

$$\mu_B = \frac{\partial E}{\partial N_B} \tag{1.2.1}$$

As it is shown in Figure, 1.2, at low μ_B the number of baryons and anti-baryons have similar values, while for high μ_B only matter is present (as for the case of stars).

Therefore, when reaching high energy density values (high momentum transfer region), the color force between gluons and quarks should sufficiently decrease to form a gas state. In other words, as the temperature gets higher, quanta interact at shorter

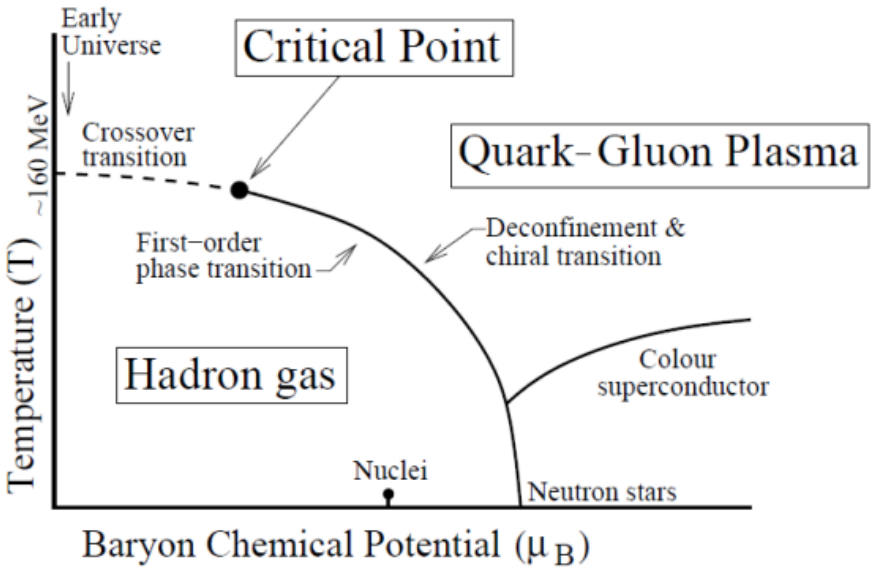

Figure 1.2: The Quantum Chromo Dynamics phase diagram.

ranges, and nuclear matter does not exhibit confinement: and this QCD phase is called *Quark-Gluon Plasma*, or QGP, which is assumed to last for $\sim 10\mu s$ after the Big Bang [3].

For low μ_B values the transition to QGP occurs at the following *critical temperature* value:

$$T_c \sim 160MeV. \tag{1.2.2}$$

Lattice Quantum Chromodynamics, or Lattice QCD confirms this prediction as the critical temperature at which the hadronic gas can undergo the phase transition to QGP.

As it is shown in Figure 1.3, when the interaction occurs, a superposition region arises: here, the formation of QGP occurs. The formed medium reaches thermal equilibrium, then expands in the vacuum due to the strong pressure. In this way, the QGP cools down until it reaches T_c, below which it changes state and hadronizes: this is called *chemical freeze-out*, because the chemical ratios between the particles become fixed. The time the QGP medium takes to achieve the freeze-out is the lifetime of the QGP itself, from 5 to 10 fm/c[1]. Then, the final step of the expansion is characterized by elastic collisions between the different products, while inelastic collisions are no longer allowed. Therefore, the chemical ratios are fixed, while the momentum distributions continue to vary: in the end, when also this process stops, we talk about *kinematic freeze-out*.

The necessary conditions to study the QGP formation are reached in laboratory thanks to ultra-relativistic collisions involving heavy ions, in which a great amount of energy is released by nucleons in a very thin region of space and short time scale,

[1]QGP has also a very small size - about a few *fm* large in diameter.

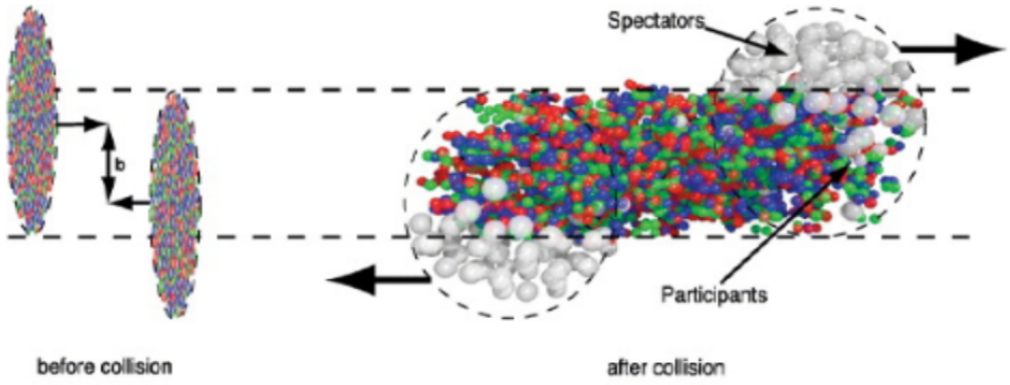

Figure 1.3: Heavy-ion collision schematic view.

generating a "fireball" of fundamental particles at very high temperature and density. In Figure 1.3 a scheme of such collision event is shown: nuclei undergo relativistic Lorentz contraction before colliding. After the collision, the participating nucleons contribute to the formation of the fireball, while the other nucleons, called *spectators*, continue to move along the beam direction.

1.3 ALICE - A Large Ion Collider Experiment

The ALICE detector is about $16 \times 26 \times 16$ m^3 large. It has been optimized to deal with high particle-multiplicity events, which are expected in Pb-Pb collisions. It can study particles down to very low transverse momentum values, about $p_T^{min} = 0.1 GeV/c$, and it features very good PID capabilities up to 20 GeV/c. In Figure 1.4 a complete scheme of the ALICE detector is shown.

The increase in LHC luminosity combined with the upgrade of ALICE - implemented during Long Shutdown 2 - will radically boost its physics-exploiting potential. In particular, the detector will address heavy-flavor hadrons, low mass di-leptons and quarkonia measurements at low p_T.

The complete apparatus of ALICE is composed of the **central barrel detectors**, covering from 45° to 135° polar angle and the **MUON spectrometer** placed in the forward direction, with other smaller detectors devoted to event trigger and characterization.

Central barrel detectors

The central-barrel detectors are the Inner Tracking System (ITS), the Time Projection Chamber (TPC), the Transition Radiation Detector (TRD), the Time Of Flight (TOF), the Photon Spectrometer (PHOS) the Electromagnetic Calorimeter (EMCal) and the High Momentum Particle Identification Detector (HMPID). They are enclosed by the L3 solenoid magnet, which has a nominal magnetic field of 0.5 T. The azimuthal cover-

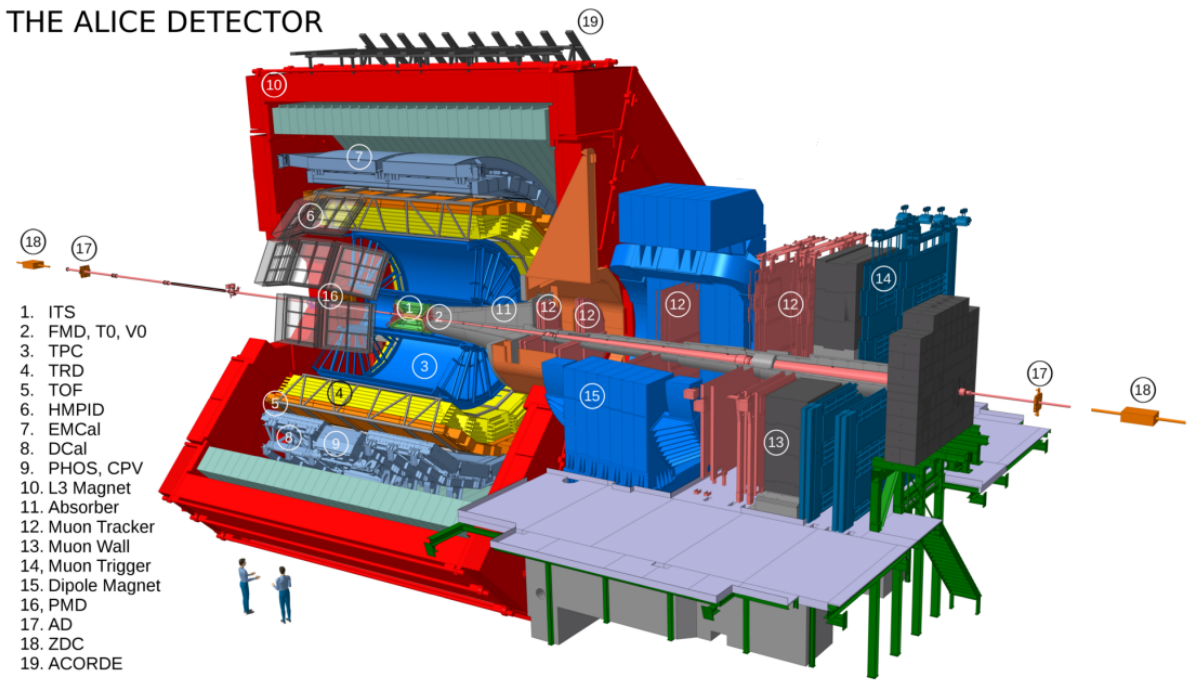

Figure 1.4: Overview of the ALICE detector.

age of the first four detectors of the central barrel is total ($0 < \phi < 2\pi$) and the rapidity has up to $|\eta| < 0.9$ acceptance. They are ordered by increasing radius from the beam pipe, as follows:

- **ITS** (Inner Tracking System), to perform tracking and vertexing. It is located very near to the beam pipe. Its goal is to precisely find the primary and secondary interaction vertices with good low p_T tracking performances. Moreover, also PID is possible in the $1/\beta^2$ non-relativistic region. It will be better discussed in Section 1.4, together with its upgrade, the ITS2, which has been almost completed during the ongoing LHC Long Shut Down 2 (LHC-LS2).

- **TPC** (Time Projection Chamber), a gaseous detector which performs tracking and PID by studying the specific energy loss. With the ITS they are the main charged particle trackers of ALICE. It is a cylinder 5m long, while the inner and the outer radii are about 57 cm and 278 cm, respectively, enclosing an 88 m^3 gas volume [4] It is divided into two parts by a central cathode kept at -100kV, while Multi-Wire Proportional Chambers (MWPCs) are placed on the endplates. Moreover, the MWPCs have been replaced by GEM detectors during the LHC-LS2.

- **TOF** (Time Of Flight detector) [5], with the aim of measuring the flight time from the Interaction Point (IP) to do PID at intermediate momenta by using Multigap Resistive Plate Chambers (MRPC) [6]. It is placed at 370 cm radially from the beam axis.

- **TRD** (Transition Radiation Detector), consisting of six layers of MWPCs and a radiator in front of each chamber. It is used to track charged particles and for electron identification via TR and dE/dx [7].

Moreover, the ITS and the TPC are light in terms of material budget: at LHC, ALICE has the lowest radiation length with respect to the other experiments in the mid-rapidity region [8] [9].

In the cylindrical volume outside the TOF there are an EM calorimeter $\sim 20X_0$ and $1 \sim \lambda_{int}$[2] thick, the PHOS and the HMPID RICH (Ring Imaging CHerenkov) detector, the latter to identify charged hadrons in the intermediate momentum range.

Forward Detectors

The **forward arm** covers a little angle range (from 2° to 9°). Many detectors compose it, including absorbers, a dipole magnet, and 14 planes of triggering and tracking chambers. These systems are detectors focused on triggering or on measuring some global event features.

In particular, the **T0** is a quartz detector delivering information about the interaction time, while **V0** is a plastic scintillator mainly used for triggering and for the determination of the Pb-Pb collisions centrality/event plane. Finally, also the **Zero Degree Calorimeter** (ZDC) can measure centrality. It is composed of two further calorimeters with the aim of counting spectator nucleons at very narrow angles, therefore they are placed at $\sim$ 114 m from the Interaction point.

The **MUON Spectrometer** aims to reconstruct heavy-quark resonances through their single muons and di-muon decay channels. It is located in the forward rapidity region, with η between 4.0 and -2.5. It consists of a hadron absorber ($\sim 10\lambda_{int}$) a dipole magnet of about 3 Tm and tracking and trigger chambers.

[2]Nuclear interaction length.

1.4 The Inner Tracking System 2 (ITS2)

ITS2 is the upgrade of the first Inner Tracking System vertex detector. It has been just installed during LS2 and will work during the LHC Run3. The aim of such a detector is to deal with high rate collision events such Pb-Pb up to 100 kHz and pp at 400 kHz, by improving the pointing resolution, when compared to the first version of the ITS by about 3 and 5 times in $r\phi$ and z direction, respectively.

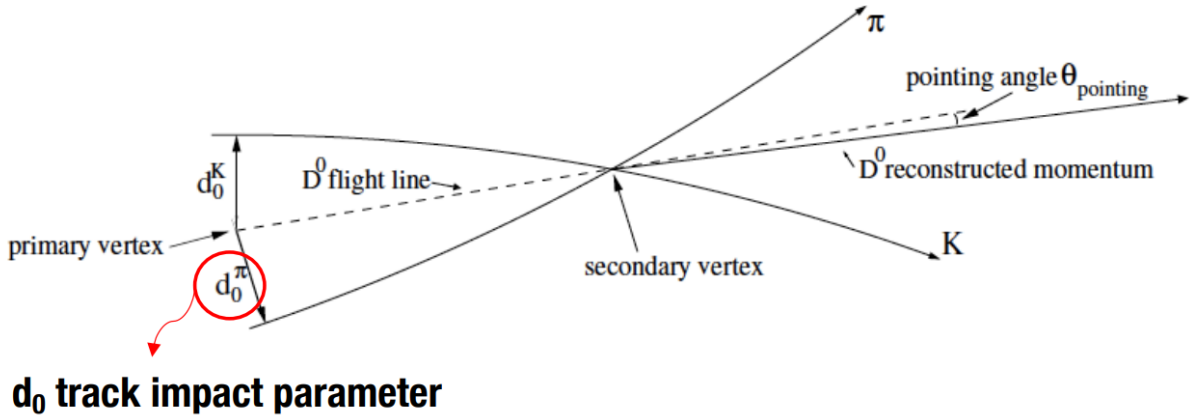

Figure 1.5: Example of Impact parameter (d) and pointing angle (θ) definition.

The resolution on the impact parameter or **pointing resolution** - which is the detector capability to separate the secondary vertices - improves as the spatial resolution ($\sim$ reduced size of the pixel of the silicon sensors) gets better. Moreover, the pointing resolution can improve also with the closeness to the IP (in particular for the first layer) and the reduction of the x/X_0 material budget. An example is shown in Figure 1.5 for the $D^0 \rightarrow K\pi$ decay.

1.4.1 Pointing resolution

To understand which characteristics should have a golden vertex detector like the ITS, let us consider for instance a simple detector configuration composed of an inner layer and an outer layer, at distance r_1 and r_2 from the Interaction Point like in Figure 1.6, respectively. If each layer features a spatial resolution σ_i, a first contribution to the pointing resolution becomes:

$$\sigma_p^{sp} = \sqrt{(\frac{r_2}{r_2 - r_1}\sigma_1)^2 + (\frac{r_1}{r_2 - r_1}\sigma_2)^2} \tag{1.4.1}$$

On the other hand, multiple Coulomb scattering in the beam-pipe and in the layers of the detector (especially the innermost) can furtherly spoil the pointing resolution. This contribution can be written as:

$$\sigma_p^{ms} \sim r_1 \theta_{RMS} \tag{1.4.2}$$

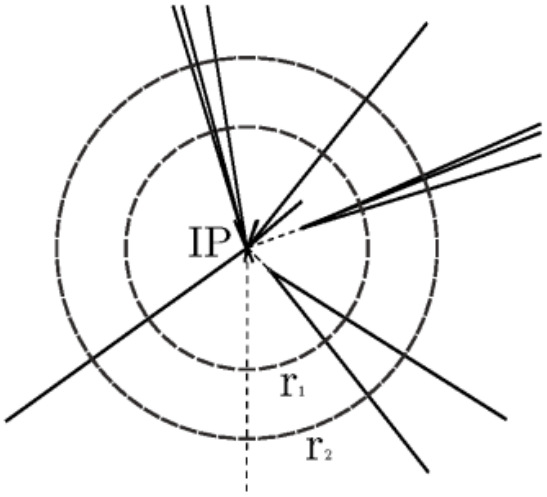

Figure 1.6: Simple 2-layer tracker example.

where

$$\theta_{RMS} = \frac{13.6[MeV]}{\beta cp} z\sqrt{x/X_0}[1 + 0.038ln(x/X_0)] \tag{1.4.3}$$

is the RMS width of the Gaussian approximation describing the angular deflection of the scattering and $p, \beta c, z$ are the momentum, velocity and the charge of the incoming particle respectively, while X_0 the radiation length associated with the material. If we consider a charged particle of unit charge and suppress the logarithmic term, the multiple scattering contribution becomes

$$\sigma_p^{ms} = \frac{13.6[MeV]}{\beta cp}\sqrt{x/X_0} \tag{1.4.4}$$

Finally the pointing resolution σ_p can be written as:

$$\sigma_p \sim \sigma_p^{sp} \oplus \sigma_p^{ms} \tag{1.4.5}$$

thus indicating that is possible to achieve a better σ_p by having a better spatial resolution of the detector, going closer to the IP, and having a lower material budget (in this particular case, of the beampipe and the innermost layer).

Layout

The ITS2 is divided into 2 barrels, the Inner Barrel (IB, from layer 0 to layer 2) and the Outer Barrel (OB, from layer 3 to layer 6) [2]. Each layer is segmented into further components, named Staves. A single Stave unit includes all the structural and functional components, so it constitutes the smallest completely operative unit of the detector. The Staves of the IB differ from the OB ones by their length, since the OB Staves are longer and they have thus a different layout. The ITS2 presents a total number of 48 Staves for the IB and 144 Staves for the OB, respectively.

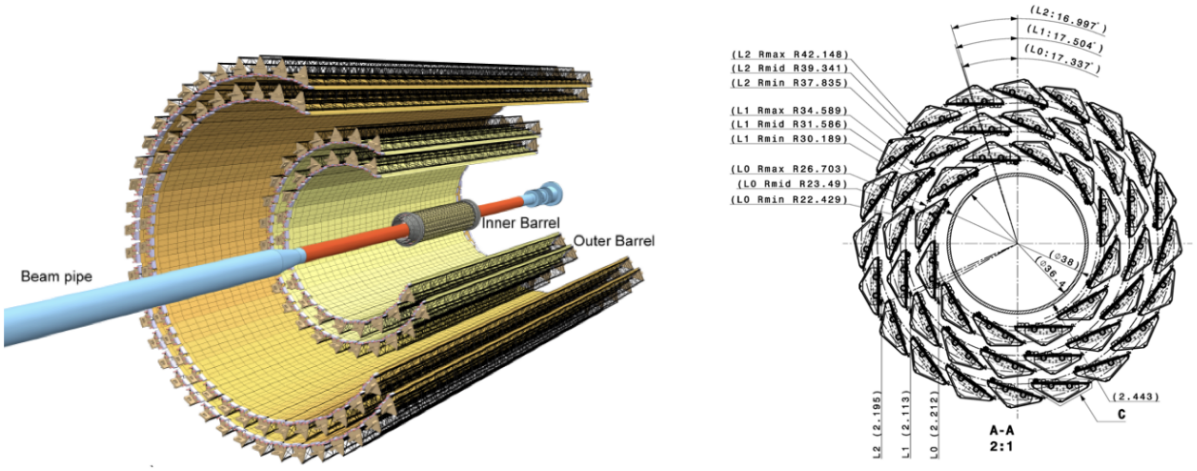

(a) full detector, with 7 layers

(b) close-up of the Inner Barrel (3 layers)

Figure 1.7: Schematic view of the ITS2 structure. [2].

The three layers of the IB are built using identical Staves (Figure 1.8, left.). Each one is divided into:

- **Space Frame**: main mechanical support stiff structure, based on carbon fiber;
- **Cold Plate**: included in the Space Frame, it is a foil of highly thermal-conductive carbon fiber in thermal contact with the Pixel Chips to remove the produced heat;
- **Hybrid Integrated Circuit (HIC)**: structure on which the Pixel Chips and passive components are placed. It consists of a Flexible Printed Circuit (FPC) in polyimide.

In each IB Stave, a HIC unit is placed: each one is made up of nine Pixel Chips arranged in a row connected to the Flexible Printable Circuit. The active area is 15 mm $\times$ 270.8 mm, with 100 μm gap between adjacent chips going along the z longitudinal direction [2]. HIC and the Cold Plate are glued together so that the Pixel Chips can face the Cold Plate to obtain the maximum cooling efficiency. In Figure 1.8 the structure of the staves of both the IB and the OB are illustrated.

The hermeticity of the barrel comes thanks to the partial overlap of contiguous Staves. The highest peaks in X_0 (around 0.5%) correspond to the overlapping structures near the Space Frame edges, and the spikes to the reinforcement in correspondence of the upper vertex. The average $X_0 = 0.35\%$ (Figure 1.9) is the lowest value experienced ever: this is a key point to reach high resolution of the impact parameter at low p_T (transverse momentum) values [2].

The Staves of the OB are similar as a concept to the ones of the IB, but they are divided in Half Staves along the longitudinal direction (Figure 1.8), each one divided in further modules (the modules number increases with the radius) [2]. As for the

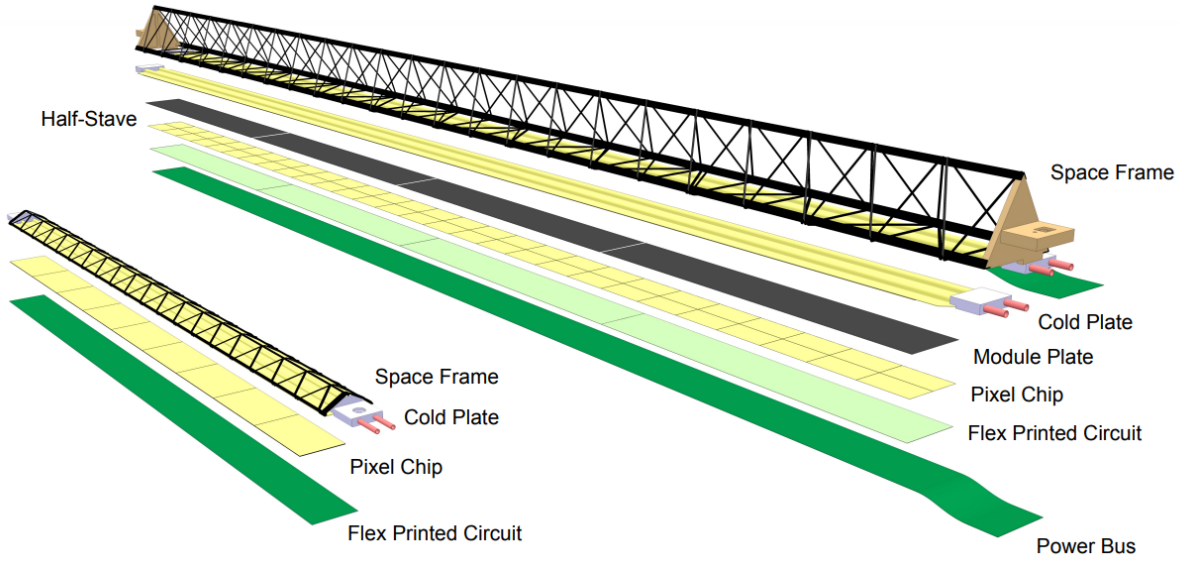

Figure 1.8: On the left and the right, the structure of the Staves of the Inner and the Outer Barrel, respectively. In particular, the FPC, the support structures, and the pixel chip wafers are shown for both cases. [2].

case of the IB Staves, the adjacent Half-Staves of the OB are superimposed over a little region, enough to ensure the hermeticity of the detector. In this case, the material budget peaks are around $\sim 1.25\% X_0$.

1.5 ALPIDE, the Monolithic Active Pixel Sensor for ITS2

The requirements on the particle sensor for vertexing in High Energy Physics are very demanding, especially in terms of material budget, readout capabilities, power management, granularity and radiation hardness.

The Monolithic Active Pixel Sensor (MAPS) technology is the answer to the need to merge both pixel sensor and the CMOS readout into a single Silicon structure - so that an interconnection between the chip and the readout is not necessary anymore - meeting the requirements of higher granularity and lower material budget. Thanks to this technology, very small pixel Si sensors can be produced.

A comparison between hybrid pixel and MAPS pixel structures is shown in 1.10. In the first case, the pixel and the CMOS readout electronics belong to different components which are coupled together, while MAPS has a CMOS-pixel forming a single structure on the substrate. The latter is also called *in-pixel* configuration. In this section, the main properties of MAPS will be presented, mainly concentrating on the chip ALPIDE, the MAPS developed for the ITS2 upgrade [3].

[3]Some fundamental concepts regarding Si detectors are presented in Appendix A.

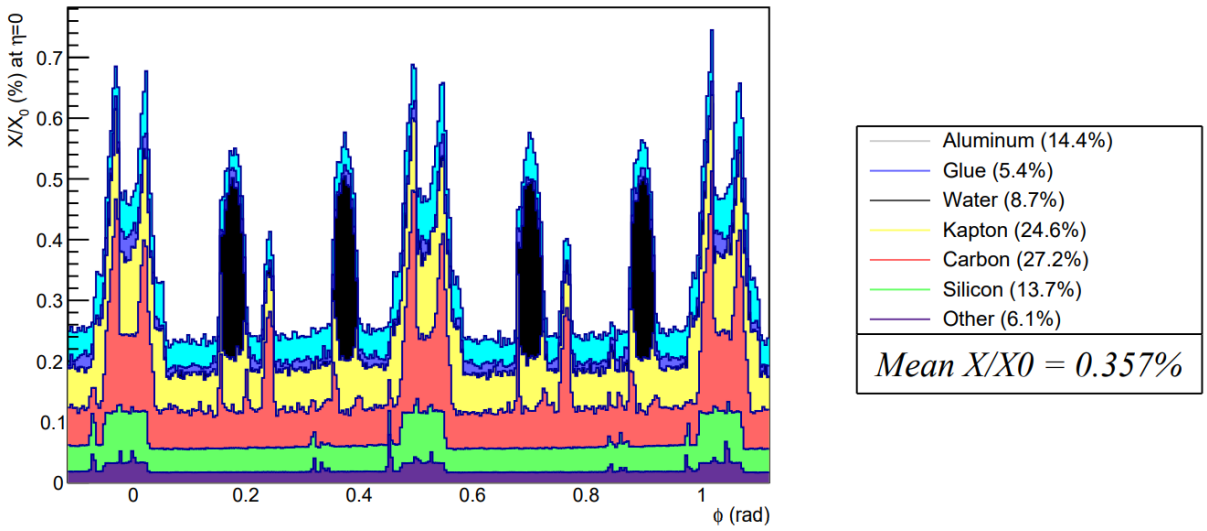

Figure 1.9: Azimuthal distribution of the Layer 0 material budget in ITS2. The value is averaged over the full barrel length. Figure from [10].

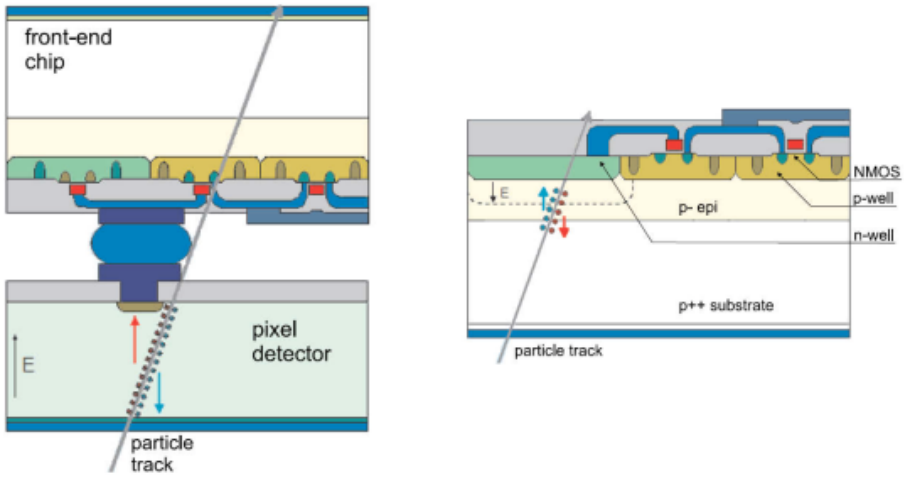

Figure 1.10: Comparison between hybrid pixel (left) and MAPS structure (on the right).

1.5.1 MAPS working principle

Typically, a MAPS implemented for High Energy Physics experiments is composed by three layers, as in Figure 1.11:

1. p^{++} highly doped substrate, acting as mechanical support;
2. epitaxial layer p^{-}, few tens of micrometers thick, implemented as the sensitive volume;
3. Upper layer with:
   - *n-well diode*, the electrode aimed to collect the charge;
   - n-type implant, named *n-well* (PMOS);

- p-type implant, named *p-well* (NMOS).

In addition, the implementation of a *deep p-well* as in Figure 1.11 under the n-well allows isolating the circuits placed on n-doped silicon bulks (for example PMOS) from the epitaxial layer and to host the CMOS in-chip circuitry. The metal layers compose the in-pixel circuits and distribute the signal and bias voltages from the periphery of the chip.

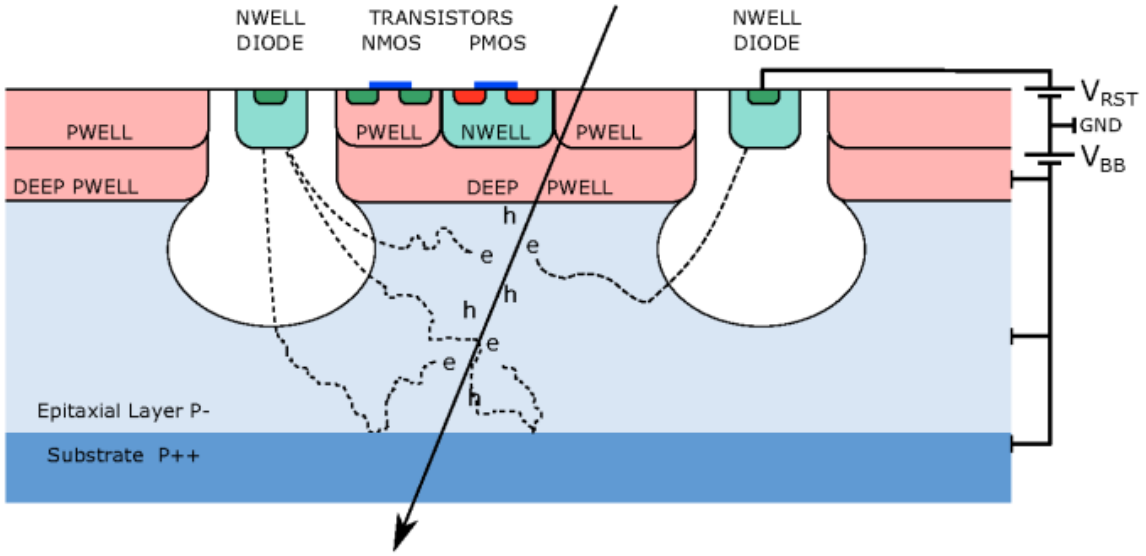

Figure 1.11: MAPS section with a charged particle (black arrow) passing through the sensor. Faltering lines represent diffusing and drifting electrons.

Modern MAPS (Figure 1.11) are mostly fabricated using an high resistivity epitaxial layer, where $\rho > 1k\Omega$cm typically. Applying a small reversed voltage to the diode, the depletion region increases. The unit pixel cell is repeated in both x and y directions forming a matrix.

When a charged particle crosses the pixel sensor it loses energy via ionization with the creation of e-h pairs along the track. The electrons formed in the epitaxial layer get trapped there, because the two junctions (p^--p^{++} and p^--*p-well*) work as barriers. They first move via diffusion through the epitaxial layer, reaching a depletion region of the diode (Figure 1.12) or recombining[4].

Moreover, the electrons of pairs generated in the p-wells or the substrate can move under thermal diffusion in the epitaxial layer[5], and then can be collected too.

Thanks to the small size of the pixel, which is $29.24 \times 26.88\mu m^2$, the MAPS shows excellent spatial resolution values also at high occupancy levels.

On the other hand, a crossing MIP generates $\sim$ 1500 electron-hole pairs for a 25 μm epitaxial layer: this value is ten times lower with respect to a usual silicon sensor

[4]This effect is negligible when considering non-irradiated sensors.
[5]Notice that an e^- can cross the p-p^+ junction only in one direction

of about 100 micrometers. As a consequence, the energy resolution is lower and the related PID possibilities are restricted.

In a MAPS the signal can be described by the following equation:

$$\Delta V = \frac{Q_{coll}}{C_p} \tag{1.5.1}$$

where C_p is the pixel input capacitance[6], ΔV the signal and Q_{coll} corresponds to the total collected charge. Clearly, to get a better signal, C_p should have the lowest possible value, and this is reached by minimizing C_r, the capacitance of the in-pixel readout circuit. The reduction of C_r is achieved by applying a reverse bias voltage to the collection diode and choosing the right diode geometry configuration.

1.5.2 Sensor design

Many parameters determine the design of a MAPS in terms of charge collection and general performances. The most relevant is the **pixel pitch**[7], which should have the smallest reachable value. At the same time, the latter is limited by the in-pixel circuit size and the rate of the readout.

The size of the n-well diode and the spacing from the corresponding p-well - which characterize the geometry of the collection diode and its capacitance - determine the design of the pixel.

Recalling the goal of the Q/C ratio optimization, as the n-well size gets smaller, also the relative capacitance decreases. However, this behavior also leads to a smaller charge collection inside it: the final Q/C value should be determined experimentally.

1.5.3 ALPIDE

The goal of the ITS2 to improve the readout rate and the position and momentum resolution, in particular for low p_T particles, requires a radically light detector with high readout speed capability and granularity. A summary of the requirements for the sensors of the ITS2 is shown in Table 1.1.

The ALICE PIxel DEtector (ALPIDE), the chip chosen for the ITS2, is a large chip ($1.5cm \times 3cm$) structured in 512 rows $\times$ 1024 columns MAPS, with a hit-driven binary readout. It features TowerJazz's 180 nm technology as a CMOS imaging process. A photo of an ALPIDE chip is shown in Figure 1.13.

As mentioned in Section 1.5.1, the presence of the deep p-weel allows, by shielding the corresponding n-well, the fabrication of PMOS transistors without penalizing the related charge collection process.

[6]Given by both the contribution of the capacitance of the readout circuit C_r and the junction capacitance C_j

[7]Distance between the center of adjacent pixels.

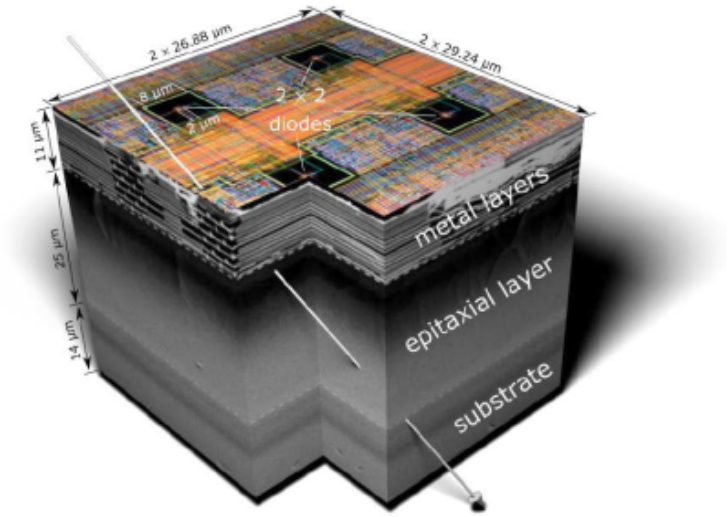

Figure 1.12: 3D section of a 4-pixel MAPS structure

Parameter	**IB**	**OB**
Sensor thickness (μm)	50	50
Spatial resolution (μm)	5	10
Dimensions (mm^2)	15×30	15×30
Power density	300	300
Time resolution	30	30
Detection efficiency (%)	99	99
Fake hit rate [a]	10^{-5}	10^{-5}
TID radiation hardness[b] (krad)	2700	100
NIEL radiation hardness[b] (1 MeVn_{eq}/cm^2)	1.7×10^{13}	10^{12}

[a] Per pixel and readout.
[b] Including a safety factor of 10, revised numbers w.r.t. TDR.

Table 1.1: Requirement for pixel sensors in ALICE ITS2 for Inner and Outer Barrel (IB and OB, respectively). Table from [2].

The in-pixel circuitry is based on a discriminating amplifier (kept continuously active) in combination with a memory where data can be strobed.

The time resolution of the event depends on the rise time of the amplifier (which is below 2 μs).

The readout of the pixel matrix is asynchronous, made by using a priority encoder circuit per double column, thus the process is fast and power-efficient since the occupancy is low and only hit pixels are read [11].

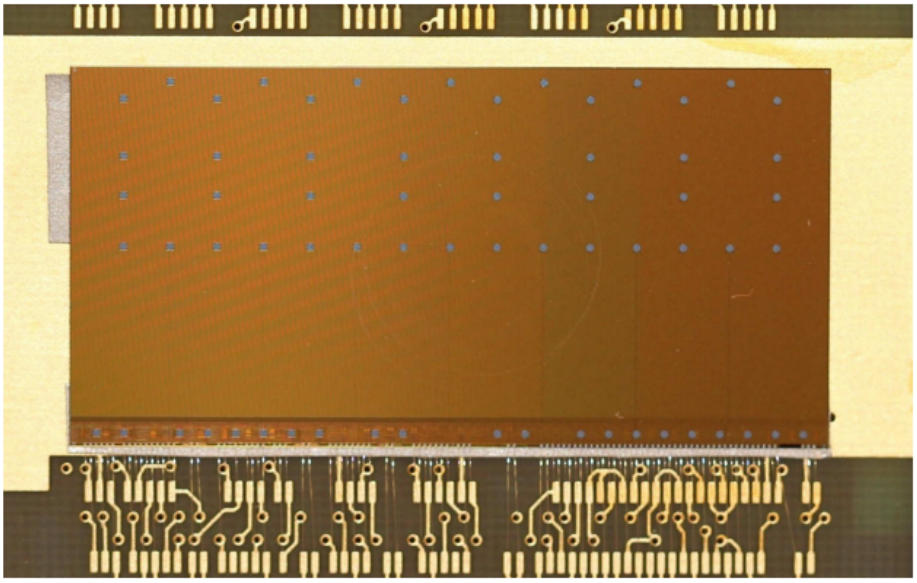

Figure 1.13: ALPIDE chip - wire bonded to a carrier board card. It is 30 mm$\times$ 15 mm^2 large and 50 μ thick.

Chapter 2

The Inner Tracking System 3

2.1 Present limitations of the ITS2

Figure 2.1 (left) shows the material budget breakdown for layer 0 (the innermost) of ITS2. The silicon sensor is responsible for only about the 15% of the total, while the mechanical support, power, and data distribution and the cooling system give the main contribution. The silicon sensor (50 μ thick) should be - ideally - the only needed component, so a natural question is if it is possible to remove the passive components by using new *wafer-scale* and *ultra-thin* CMOS sensors.

The need for a new type of silicon sensor capable to satisfy these new requirements is the guideline towards LS3. Since during the ITS2 R&D it has been shown that further improvements in cooling system, mechanical support structure and power and signal distribution can be made [10], the ALICE collaboration has planned a further upgrade of the Inner Tracking System, named ITS3, for the LHC RUN4 and to be installed in Long Shutdown 3 (LS3) in 2025, replacing the three innermost layers of the existing detector

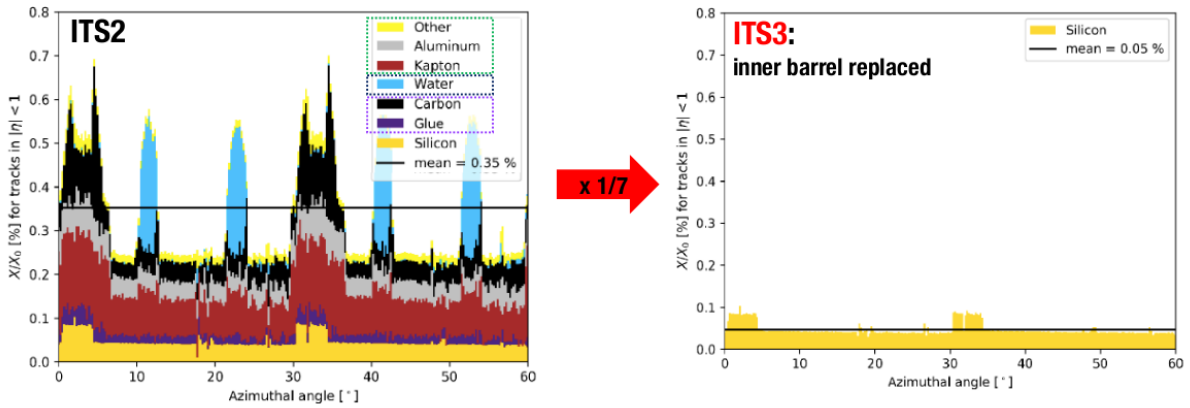

Figure 2.1: Azimuthal distribution of the Layer 0 material budget in ITS2 compared to the expected material budget for the same layer in ITS3. The value is averaged over the full barrel length.

Development of a new wafer-scale bent sensor

The cornerstone of the upgrade is a new CMOS MAPS built using 65 nm technology, instead of the 180 nm technology of ALPIDE, and a **bent-cylindrical configuration**.

The proposed new detector will replace the three innermost layers of the ITS2 (the *Inner Barrel*), with the aim to get closer to the IP, reduce the material budget to the minimum by using a **single** and **thinner** silicon wafer, **bent** around the beam pipe (which will have a lower radius, too). Therefore, thanks to these improvements the ITS3 will achieve better spatial resolution, reaching very high tracking and vertexing performance (as described in Section 1.4).

In ITS2, small sensors are built up edge-to-edge on top of an FPC which provides both power supply and data bus. The goal is to replace this type of module with a single large sensor thanks to the *stitching* technology[1], performing internally the power distribution management and limiting the connections to the outside to the edges.

Since stitching allows the production of a wafer-scale CMOS image sensor, it is possible the fabrication of a novel circuit, 15 mm $\times$ 140 mm large, corresponding to about half the length of the stave. Columns are read out by groups of 16 by sequence, however, is it possible to read out all of them in parallel. Data transmission goes from the bottom of the columns (corresponding to one of the long sides of the chip) to the periphery.

Since the periphery of the sensor is outside the acceptance of the detector, there are not constraints on its size, which will be set depending on the requirements. Concerning the power supply, a flexible PCB (located under the chip digital periphery) will provide it to the sensor.

The final large sensor will be thinner with respect to ALPIDE, reaching value thickness values of about 20 μm to 40 μm, corresponding to radiation length values from 0.02% to 0.04% X_0. [12].

2.2 ITS3

Mechanical structure

The ITS3 will have a considerably reduced material budget and will be closer to the IP thanks to the lower radius of the beam pipe. Also the ITS3 will consist of two distinct barrels, Inner and Outer Barrel, respectively. This upgrade aims at replacing the Inner Barrel of the ITS2 with an even better detector [13], so the four outermost layers - from 3 to 6 - will be the same as ITS2. The Inner Barrel of the ITS3 structure includes two halves, the *half-barrels*, allowing the detector to be placed around the beam pipe, each

[1]Stitching technology allows fabricating silicon sensors of arbitrary dimensions, where the limit is given only by the size of the wafer.

one made of three half-layers, as it is shown in Figure 2.2. At $z = 0$, each half-layer is divided into further two halves, the quarter-layers. Each quarter is a single large pixel chip with a half-cylindrical geometry configuration.

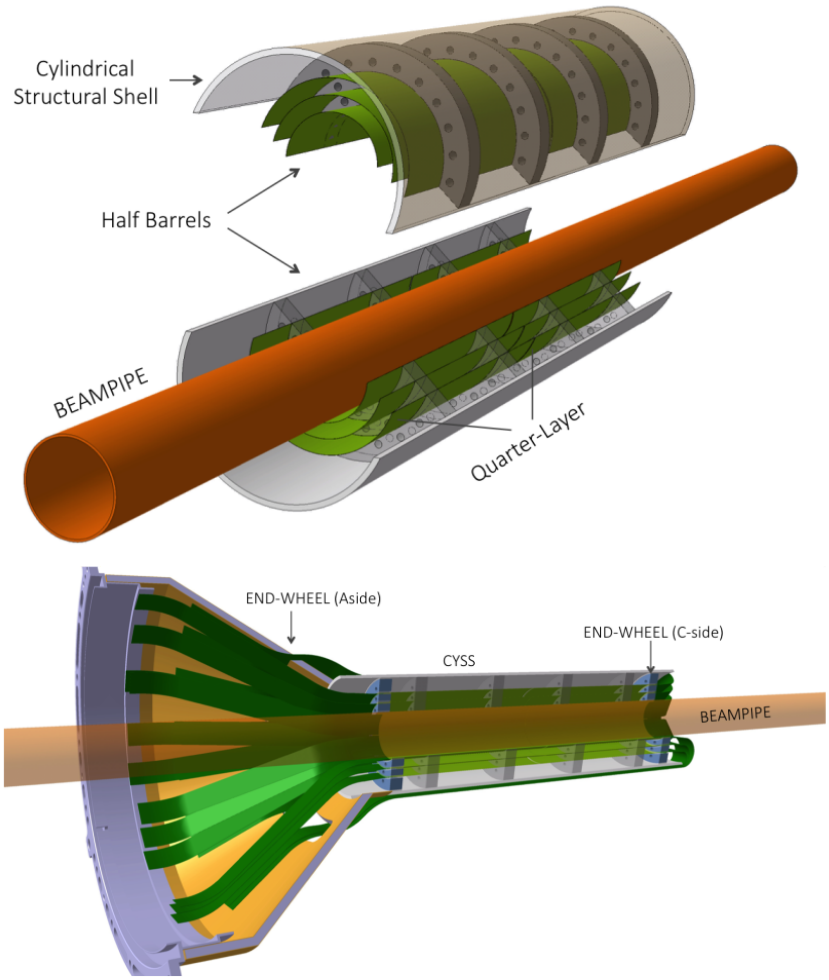

Figure 2.2: ITS3 Inner Barrel scheme. [10].

The integration scheme differs little from the one used for ITS2, in which the detector is decoupled from the beam pipe. The Inner Barrel is supported by the *Service Barrel* (Figure 2.3), bound to the TPC cage.

The ITS3 Inner Barrel is divided into two substructures, the End-Wheels and the external Cylindrical Structural Shell (CYSS), both consisting of Carbon Fibre Reinforced Plastics and connected between each other. In addition, open-cell carbon foam is used for the production of the spacers (Figure 2.4) located between the layers, with the goal to fix their relative radial position. Hence the connection between the 3 IB half-layers is performed by the half-wheel spacers.

Each quarter-layer is made of a large single chip, and on the A-side End-Wheel (Figure 2.2) the relative periphery and interface boards are located. An FPC is glued on the A-side to the chip, over a length of 5 mm. The electrical interconnection is performed by aluminum wedge wire bonding, and finally the FPC goes from the chip

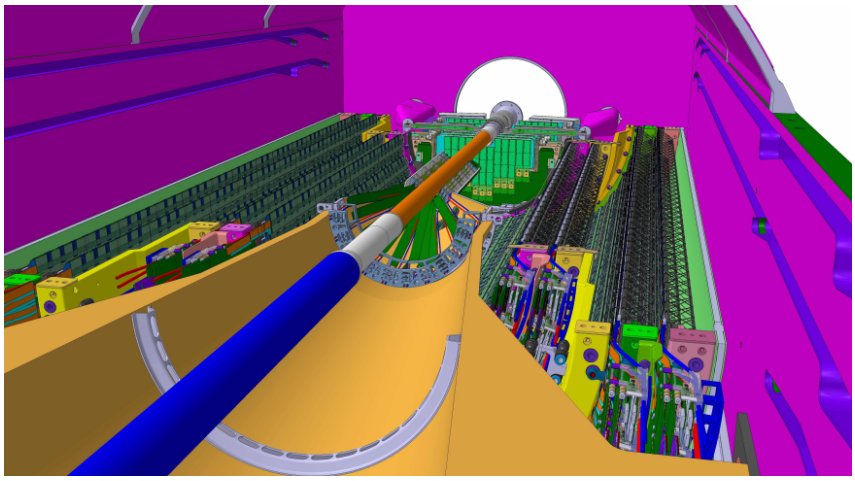

Figure 2.3: Inner Tracking System 3 layout, including the Inner Barrel integration inside the detector. The yellow structure is the service barrel, while the magenta one is the TPC cage. [10].

edge towards a panel located at the terminal of the End-Wheel: here, interconnections to data and power supply cables are completed. On the C-side, the cables exit from the relative End-Wheel, then run towards the A-side from the outside of the CYSS. A summary of the parameters related to the ITS3 Inner Barrel is shown in Table 2.1.

Beam pipe inner / outer radius (mm)			
IB Layer parameters	Layer 0	Layer 1	Layer 2
Radial position (mm)	18.0	24.0	30.0
Length (mm)	270	270	270
Pseudo-rapidity coverage	$\pm$ 2.5	$\pm$ 2.3	$\pm$ 2.0
Active area (cm^2)	305	408	508
Pixel sensors dimensions (mm^2)	280 $\times$ 56.5	280 $\times$ 75.5	280 $\times$ 94
Number of pixel sensors / layers	2	2	2
Pixel size (μm^2)	O(15$\times$15)	O(15$\times$15)	O(15$\times$15)

Table 2.1: Summary of ITS3 foreseen geometrical parameters [10].

Cooling system

Also the cooling circuit contributes, as said above, to the final material budget. To remove the heat produced by the IB layers of the ITS, the possibility also to use a low speed ($< 2m/s$) air flow combined with peripheral liquid cooling has been studied during the R&D for ITS2. It has been experimentally shown that this option is possible only for sensors reaching less than $20mWcm^{-2}$ power density [14]. On the other hand, the higher the airflow, then the stiffer the mechanical structure should be to minimize the sensor vibrations and keep them smaller than the intrinsic value of the spatial resolution. This fact leads to a higher material budget as the airflow increases.

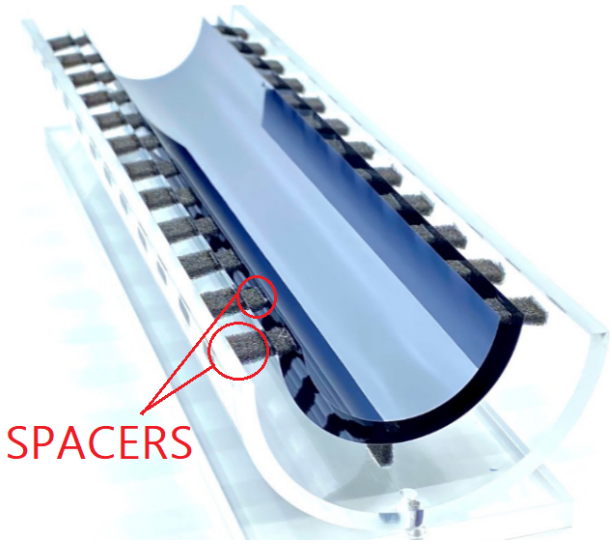

Figure 2.4: Engineering model for the ITS3 Inner Barrel. [13].

The heat dissipation inside the ITS3 IB works by convection, thanks to an artificial airflow running through the layers; a contribution to cooling comes also from the carbon foam rings since they are kept in thermal contact with the chips, leading thus to a reduction of the thermal gradient across the layer. In general, carbon foam materials constitute the best way to perform heat exchange, due to the mix of low density and exceptional thermal conductivity. In order to keep the mechanical stability (vibrations caused by the airflow must be avoided) and the thermal performances, the design process will optimize the speed of the airflow.

Some considerations on the power consumption should also be made. The ALPIDE total power consumption is 180 mW, about 40 $mWcm^{-2}$ power density. Nevertheless, about 150 mW dissipate via the digital interface circuits and the high-speed data output links: their location is near to one of the edges of the chip within a small area. So only $\sim 1/6$ of the total power consumption comes from the pixel matrix, corresponding to a power density of $\sim 7\ mWcm^{-2}$. This would be a good value considering the air flow cooling option [10].

Summary

The main changes introduced in the passage from the ITS2 to the ITS3 are the following:

- the first layer of ITS3 will be closer (R=18 mm) with respect to the one of ITS2 (R=23 mm).
- bending, thinning, and stitching constitute a revolutionary step in chip production. In particular, the chip will be thinned down to 20-40 μm (corresponding to

0.02-0.04%X_0);

- the new chips will implement the new CMOS 65 nm technology instead of the 180 nm used in ALPIDE. The spatial resolution will improve thanks to the reduced pixel size;
- the water cooling can be replaced by air cooling when reaching a power consumption under 20 mW/cm^2 (now ALPIDE is at 40 mW/cm^2) [10];
- the mechanical support can be removed if, by rolling the Silicon wafers, the stiffness increases;
- the readout boards/circuit board can be removed if integrated into the circuit;

Particle density (cm^{-2})				
	LS2 upgrade		LS3 upgrade	
Layer	Hadronic[a]	QED electrons[b]	Hadronic[a]	QED electrons[b]
0	43	7	73	12
1	25	3	43	8
2	17	2	29	6
[a]calculated for central Pb-Pb collisions and including secondaries production in the material, with a 0.2 T magnetic field.				
[b]calculated at 50 kHz of interaction rate and for 10 microseconds of integration time, with a 0.2 T magnetic field.				

Table 2.2: Summary of the maximum expected particle density per each ITS Inner Barrel Layer [10].

2.3 Performance of the detector

The new ITS will radically improve the ALICE tracking performances in terms of vertexing precision and tracking efficiency. To study the ITS3 performances many simulations have been made: some considerations about the experimental conditions should be made before this.

2.3.1 Experimental conditions

The value of the particle flux traversing the detector (Layer 0 in particular) and the corresponding radiation load will increase due to the closer position of the inner layers with respect to the interaction point.

In addition, a further contribution to the radiation load comes from e^+e^- pairs (QED electrons), coming out when the crossing ions interact electromagnetically. In Table 2.2 the values of the particle density for both the ITS3 and ITS2 Inner Barrel are listed. Despite the steep increase of the particle density ($\sim 70\%$) in correspondence of the innermost layer, the hit occupancy (number of hit pixels in the chip) will still be sufficiently small (1×10^{-3}), thanks to the large granularity of the detector.

In such conditions, Layer 0 will measure a particle flux around 4 MHz cm^{-2} in case of a Pb-Pb 50 kHz interaction rate: the ALPIDE chip is easily capable to sustain such a value. Despite the fact that the radiation load is also going to increase ($\sim 60\% - 70\%$), it will be still under $1\times$ MeV n_{eq} /cm^2 (NIEL[2]) and 10000 krad (TID[3]). ALPIDE fully maintains its performance under this radiation load value.

[2]Non Ionizing Energy Loss.
[3]Total Ionizing Dose.

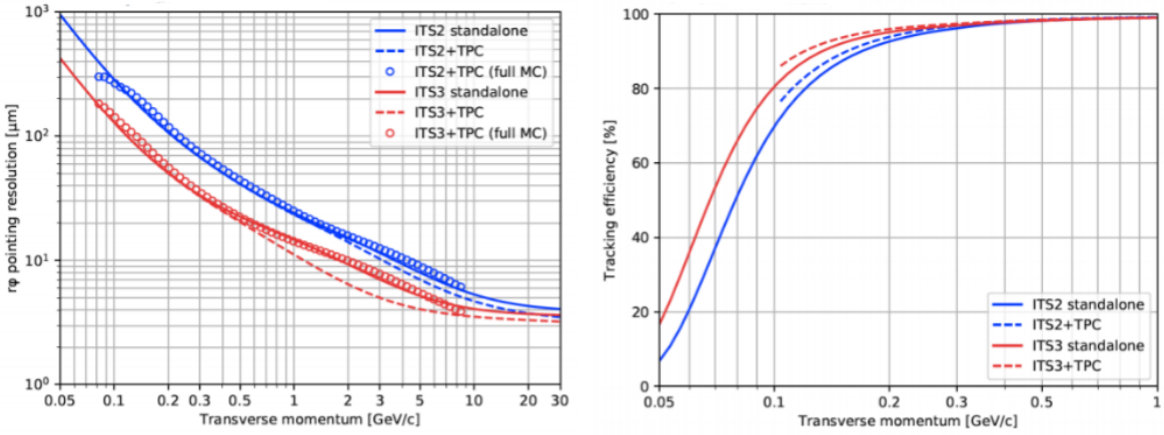

Figure 2.5: Left: Comparison between the simulated ITS2 and ITS3 pointing resolution. LS2 and LS3 ITS upgrades are represented using blue and red lines, respectively. Right: Comparison of the simulated tracking efficiency for ITS2 and ITS3.. [10].

2.3.2 Tracking

A Fast Monte Carlo Tool (FMCT) gives a good estimate of the tracking resolution and efficiency, considering effects as secondary interactions, multiple scattering and also detector occupancy; however, it does not consider the energy loss of the particles inside the beam pipe and the detector [2]. Thanks to this tool many detector parameters like the number of layers and relative radial position, the resolution and the material budget have been set.

In Figure 2.5 a comparison between the calculated values of the pointing resolution in both ITS2 and ITS3 is shown ($\eta = 0.5$, for pions). Solid lines come out from the fit of the tracks only with respect to the ITS layers, the dashed ones instead including both the ITS and the TPC.

It should be noticed that when $p_t = 1$ GeV/c the value of the ITS3+TPC pointing resolution is about two times better than the ITS2+TPC one. Also the Full MC simulations shown in Figure 2.5 confirm this result.

2.3.3 Physics goals

Most of the measurement of the observables studied by ALICE at low p_T will benefit from the improvement in spatial resolution, combined with the lower material budget: in particular, the studies of heavy-flavor production (especially for baryons) and of low-mass e^+e^- (*dielectrons*) - relevant for the ALICE physics goals in the next years - will take advantage from the upgrade.

Λ_c production

To inspect the thermalization and hadronization of charm and bottom quarks in the QCD medium, the study of the charmed and beauty baryons production becomes determinant. During Pb-Pb collisions heavy quarks can recombine with lighter-flavor ones inside the QGP. In this case, a significant increase in the charm/beauty baryons production is expected[4] at low momentum (< 10 GeV/c).

For p_T between 1 GeV/c and 6 GeV/c, an increase of the baryon-to-meson ratio has been observed for light-flavors, in particular for p/π [15] and Λ/K^0_S [16]. This effect can be explained in terms of recombination of light quarks and radial collective flow dependent on the mass of the hadron [16].

Crucial information about the thermalization and hadronization of the c quark inside the QGP can come out from a precise measurement regarding the charm sector. Moreover, further evidence of charm quarks deconfinement in the fireball can come out from these measurements.
Experimentally, the main problem comes when measuring the very short lifetime of charmed baryons: for instance, Λ_c has a $c\tau \sim 59\mu$m, which is about 2 times smaller than the one of D^0 meson. The most detectable decay channels for the Λ_c are:

$$\Lambda_c^+ \to pK^-\pi^+, \qquad \Lambda_c^+ \to pK^0_S.$$

In the first case, the three-prong combinatorial background is large, while in the second case the K^0 has a too long decay length, so it is not possible to precisely determine the decay vertex.
The $\Lambda_c^+ \to pK^-\pi^+$ is the benchmark channel for the ITS2 development [2] and also for the ITS3 IB upgrade because optimal and precise tracking and spatial resolution are required since the distance of the decay tracks from the major interaction vertex is typically only about few tens of microns. Therefore, the Λ_c measurement is a perfect test for the assessment of the improvement introduced by the ITS3, especially regarding the heavy-flavor physics performances.

As mentioned above, the same studies carried out for the ITS2 have been done for the ITS3 case, using the same method as described in [2], applying a correction to the geometry parameters of the ITS2 to reproduce the pointing resolution of the ITS3 configuration, as shown in Figure 2.5. The same has been done for the simulated performance of the Λ_c reconstruction, as illustrated in Figure 2.7.

A precise measurement of the p_T-integrated yield of Λ_c production is the key to determine the total $\sigma_{\bar{c}c}$ cross-section since it should test the enhancement of the relative Λ_c abundance with respect to D mesons. The total charm-anticharm cross-section is crucial for calculations of charmonium regeneration models in the QGP framework, so

[4]Compared with the same momentum region in pp collision measurements.

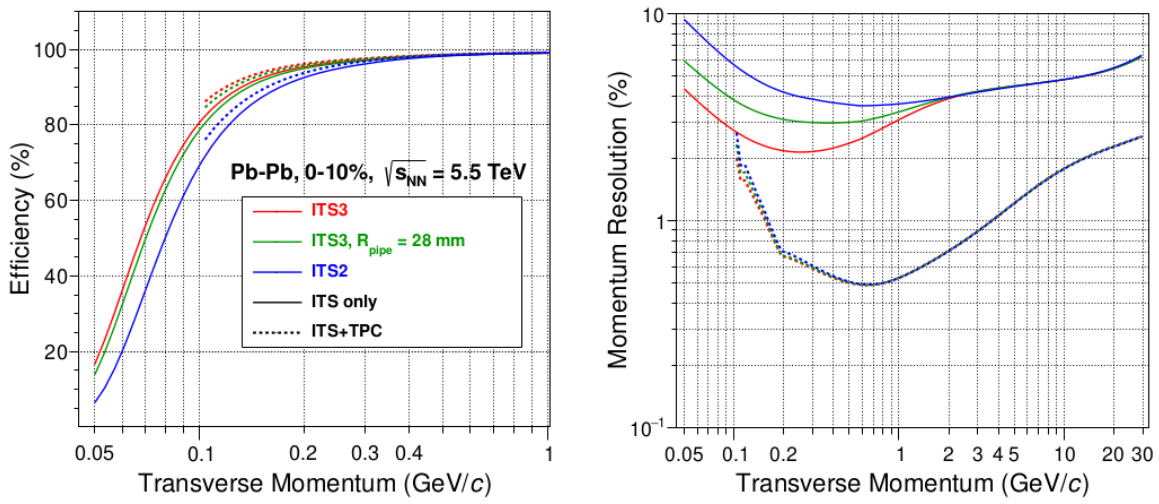

Figure 2.6: Comparison between the ITS3 and the ITS2 in terms of track finding efficiency and transverse momentum resolution [10].

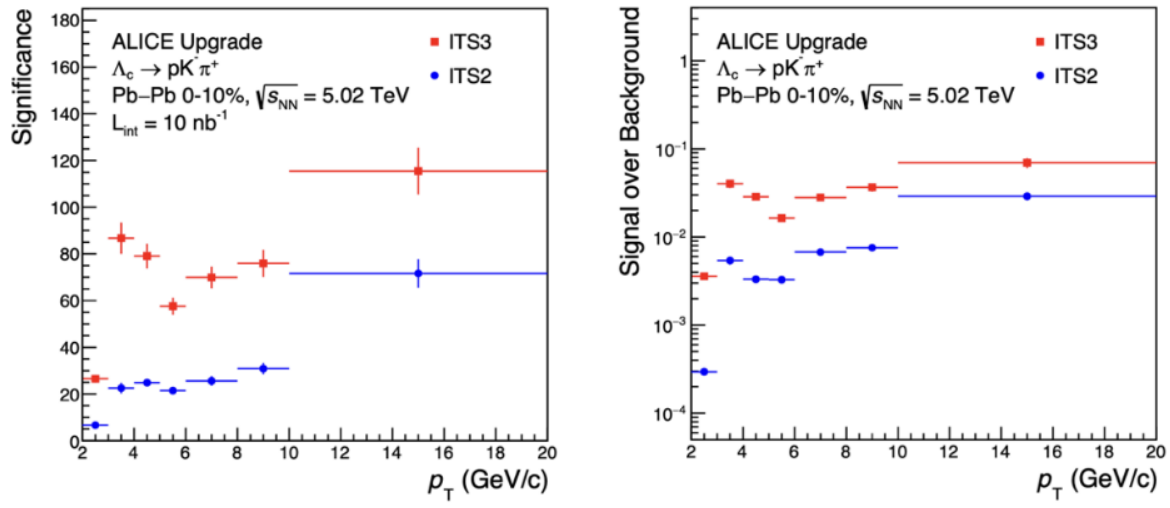

Figure 2.7: Simulated performance of the Λ_c^+ reconstruction for ITS2 and ITS3. Statistical significance (left) and S/B ratio (on the right) are plotted versus p_T. Figure from [10].

also the quarkonium studies will benefit from the significance increase in low transverse momentum regions.

Thermal Dielectrons

It is possible to detect the EM radiation coming out from the high-T system arising in heavy-ion collisions thanks to low-momentum real photons, or virtual ones generating dilepton pairs with low invariant mass. The ALICE central barrel can detect them down to $p_T < 100$ MeV.
However, their production rate value is tiny, because suppressed by the $1/\alpha_{EM}^2$ proportionality, so a high-performing electron identification is needed to overcome the combinatorial background where a hadron of the pair is wrongly identified as an electron.

The thermal dielectron pairs measurement performance will benefit from the ITS3 upgrade. Firstly, this becomes possible thanks to the lower material budget (by the 30% for the beam pipe and six times lower for the first IB layer), so that the number of produced electrons by photon conversion will decrease about three times before the first point of the measured track.

Chapter 3

Corryvreckan

Introduction

Data reconstruction of a test beam requires high flexibility because of the large variety of data acquisition conditions present in a single setup, so to reconstruct particle tracks an event reconstruction algorithm/data analysis framework is required. *Corryvreckan* [17] is a framework, written in C++, used for test beam data reconstruction and analysis, which performs offline event building also in data-taking conditions with high complexity. The required external dependencies are minimal and the execution is fast and lightweight. In this chapter, the fundamentals of the Corryvreckan working operation flow are illustrated. All the plots provided as examples in this chapter are taken from the data analysis I have performed of the August beam test by using this framework and thanks to further modifications that I have written to the Corryvreckan source code.

3.1 Analysis observables in beam test

The purpose of a beam test of a tracking/vertexing detector is usually to measure its **detection efficiency** and **spatial resolution**. Typically, the setup of a beam test consists of a telescope of reference planes and a Detector Under Test (DUT) positioned in a beam of ionizing particles. The position of such reference is designed in order to obtain the best possible tracking resolution.

The **reconstruction chain** of the program is divided into specific modules, depending on the task to be accomplished, ranging from the track reconstruction by the reference planes, to the final analysis of the DUT performance. This modular structure allows the user to modify the source code to add functionalities, for instance when dealing with a new sensor type or novel sensor configurations, to produce the necessary plots.

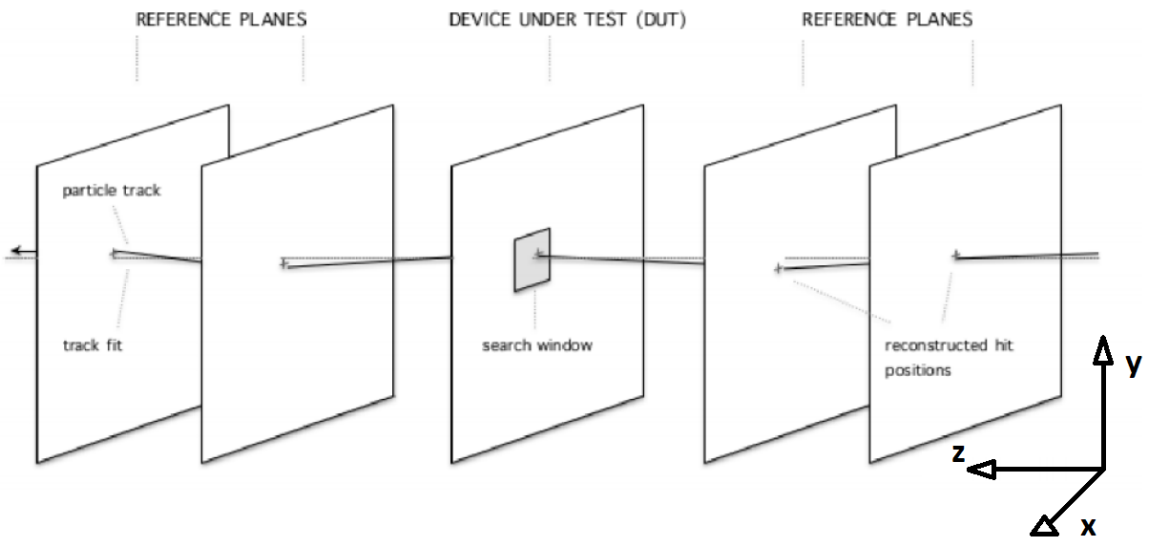

Figure 3.1: Scheme of a test beam setup, with one DUT and four reference planes. In the DUT surface, an example of the search window is shown.

The final data analysis carried by Corryvreckan produces plots using the ROOT[18] data analysis framework. All the numbers presented in this description are also used as a reference for the analysis that has been carried out.

Consider now a simple test beam telescope like in figure 3.1, with a generic $m_{rows} \times n_{columns}$ pixel detector as DUT. Given the raw data file produced and stored at the end of a single test beam run, Corryvreckan analyses the data file and extracts the plots by following these steps:

- **Masking**: identification and masking of the pixels of the DUT fired at a rate higher[1] with respect to the average firing rate of a pixel considering a single run.

- **Prealignment**: correlation of the hits on all the planes of the telescope with the hits on the first reference plane, using as input for the position the manually measured coordinates of the geometry file. Then the planes are aligned along x-shift and y-shift using the Gaussian fit mean of the hit position and the geometry file is updated...

- **Clustering**: since more than 1 pixel can be fired with a single particle hit, a group of contiguous fired pixels with a charge collection larger than a fixed *threshold*[2] are named **clusters**. The hit position is then estimated using the center-of-gravity technique.

[1] In this work, this rate value was set as 1000 times higher than the average.

[2] In this analysis, the threshold changed depending on the considered run, where each run counted about 300k events.

- **Pre-tracking**: building of straight-line pre-tracks using the cluster on all the detectors, including also the DUT.

- **Alignment**: the pre-tracks in 3 degrees of freedom (x-shift, y-shift, z-rotation) are used to align the detectors, using the updated geometry coordinates from the prealignment procedure.

- **Tracking and tracking association**: for each event, the clusters in the reference planes are used to reconstruct the straight-line tracks. Then, a χ^2 test is used for the goodness-of-fit. Then, the tracks are associated with the respective clusters identifying the latter on the surface of the DUT within a circular window centered on the track intercept. In the data analysis presented in this thesis, the window radius has been set to 250 μm.

- **Residuals**: the spatial residuals in the (x, y) plane of the DUT, defined as the (*row, column*) distance $(x_{track} - x_{hit}, y_{track} - y_{hit})$ between the associated cluster and the intercept of the track, are calculated.

- **Efficiency calculation**: a track is considered as efficient when the hit falls inside a pre-defined *search window*[3], as in Figure 3.1. So the **detection efficiency** is computed as $\epsilon = k/n$, where k and n corresponds to the numbers of efficient and total tracks, respectively.

The **spatial resolution** is computed in a second time after the Corryvreckan data processing. It is calculated as the difference between the variance[4] σ^2_{res} of the gaussian fit of the residual distribution and the square of the track resolution σ_{track}[5]:

$$\sigma^2_{sp} = \sigma^2_{res} - \sigma^2_{track} \tag{3.1.1}$$

Usually, the spatial resolution and the efficiency are plotted versus the charge threshold of the pixel or the cluster size, with the aim to determine the performance of the sensor.

3.2 Corryvreckan Modules for Data analysis

Corryvreckan execution is divided, as mentioned in Section 3.1, into several modules executed in chain. At the end of each module execution a corresponding .root file,

[3]The determination of the size of the search window depends on the experimental setup and the chosen particle beam type and energy. For instance, in the case of higher multiple scattering typically the size is larger.

[4]The variance σ^2 is defined as $E[X^2] - E[X]^2$, where $E[X]$ is the expectation value of the distribution.

[5]σ_{track} depends on the reference planes intrinsic resolution and other uncertainties, due for example to multiple scattering.

containing many plots, is produced as output. In this section, the most relevant modules used for the data analysis of this thesis work are presented. In addition, during the analysis, some modifications have been applied to the source code to produce new plots. At the end of this section, the modifications and the relative plots are shown and explained.

Coordinate systems and Geometry file

Local coordinate systems and a global reference frame, for the planes and the full setup respectively, are defined inside the framework. The global reference frame is always a right-handed Cartesian frame. The beam direction in general determines the positive z-axis. The origin of the 3-axis systems typically is fixed depending on the position of the detectors inside the setup. Also, the local reference frames of the detectors are Cartesian and right-handed: the sensor plane corresponds to the (x_{local},y_{local}) plane.

Before running Corryvreckan, the **geometry file** configuration of the detector must be set. Inside it, as shown in Figure 3.2, the data related to the intrinsic performance of the various telescope planes are entered, as well as the relative distances between the planes within the experimental setup. The Corryvreckan execution reconstructs the event and performs the analysis taking the geometry file as a first input.

In addition, is possible for each sensor to define a **Region Of Interest** (ROI). The ROI allows the tracks and the cluster to be labeled as within a certain region of the plane of the sensor or not. This additional information is particularly useful during analysis and especially efficiency computation because it is possible to put some restrictions in tracks/clusters to eventually exclude from the analysis some known bad regions of the chips. In case of a rectangular chip, the four corners can be provided to define the ROI. So the ROI is defined as follows inside the code, using the `roi` keyword as in Figure 3.2:

```
roi = [0, 0], [0, 512], [1024, 512], [1024, 0],
```

where 1024 $\times$ 512 corresponds to the *rows* $\times$ *columns* configuration of an ALPIDE chip.

[Prealignment] and [Alignment]

The z position of the detector planes must be measured **manually** in the test beam setup, then entered in the geometry configuration file for the analysis. On the other hand, x and y positions and the rotations are not precisely measurable in this way, despite having a large influence on tracking: also a little misalignment might correspond

```
[ALPIDE_0]
type = "ALPIDE"
position = 0um,0um,-94.5mm
number_of_pixels = 1024,512
pixel_pitch = 29.24um, 26.88um
spatial_resolution = 5.00um, 5.00um
time_resolution = 2us
material_budget = 0.001
coordinates = "cartesian"
orientation_mode = xyz
mask_file = "../masks/ref-plane0.txt"
# roi = [0, 0], [0,512], [1024, 512], [1024, 0] # wide
roi = [200, 100], [200, 400], [800, 400], [800, 100] # strict
# roi = [100, 50], [100, 450], [900, 450], [900, 50] # not-so-strict
# roi = [400, 200], [400, 300], [600, 300], [600, 200] # very strict
role = "reference"
```

Figure 3.2: Particular of a geometry file with the defaults for the first tracking plane of ALPIDE type in a beam telescope. The file includes specifications like the z position in the global coordinate system, the role (*reference*) of the plane, and information about intrinsic features of the sensor like the number of pixels and the intrinsic spatial resolution.

to a large shift in terms of pixel coordinates. Therefore, during the analysis an alignment procedure is necessary. Corryvreckan has specific modules to accomplish it and to increase the tracking performance.

More specifically, the **track residuals** of each plane must be centered around 0 and their distribution must be the narrowest possible, so the final goal of the alignment procedure is to force the adjustment of the distribution of the residuals improving the precision of the initial manually inserted position values for the planes. The width of the residuals distribution depends on the **tracking resolution** of the detector and other factors like the **beam energy**, the **material budget** of the planes, and the **distance** between the telescope planes, as explaned in Section 3.1.

The `[Prealignment]` module produces the **spatial correlation plots**. They are filled with the spatial difference between the cluster on a given plane minus the position of **any** cluster on the other planes. These plots do not have to be centered at 0, because they might reflect somehow a *physical displacement* of the plane with respect to the reference plane, but it is useful to check if these shapes are Gaussian-like and sufficiently symmetric before proceeding with the other steps of the analysis. In Figure 3.3 a correlation plot for the DUT is shown.

The `[Alignment]` procedure is automatic: to increase the tracking quality of the telescope, the shift and rotation of the planes are iteratively repeated relative to the reference plane. Upon completion of the alignment procedure, the residuals for the reference planes are calculated and their distributions plotted. An example is shown in Figure 3.4.

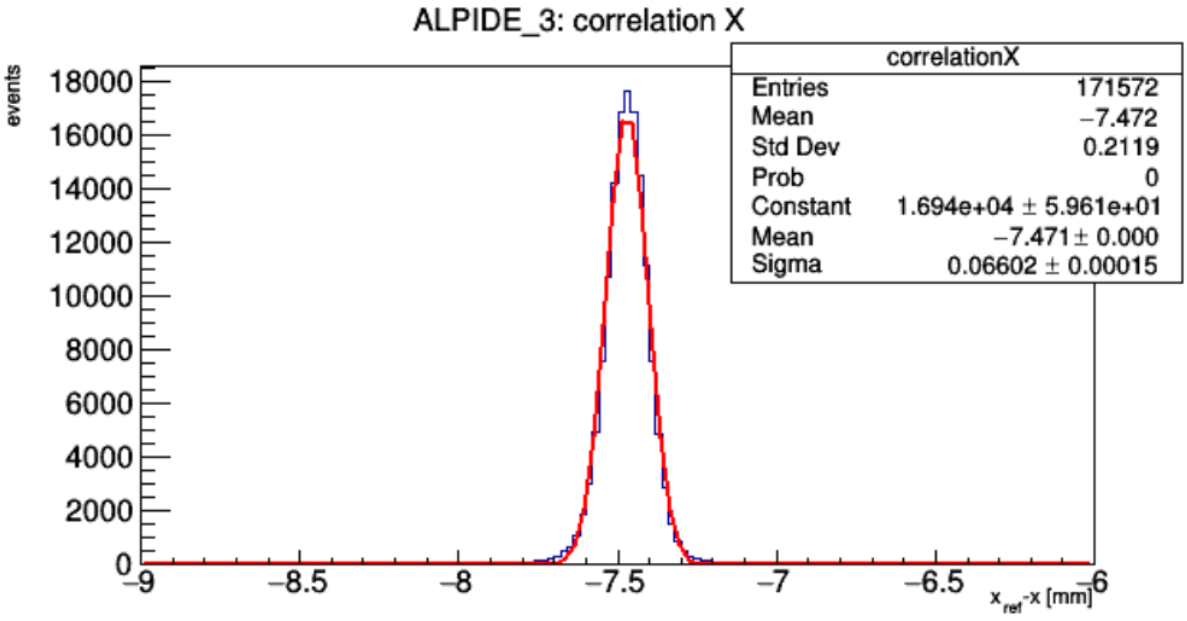

Figure 3.3: Correlation plot of a DUT ALPIDE chip in the x direction $x_{ref} - x$, the input data for the position of the detector planes are taken from the geometry file. The red curve is the Gaussian fit, as it is performed by Corryvreckan.

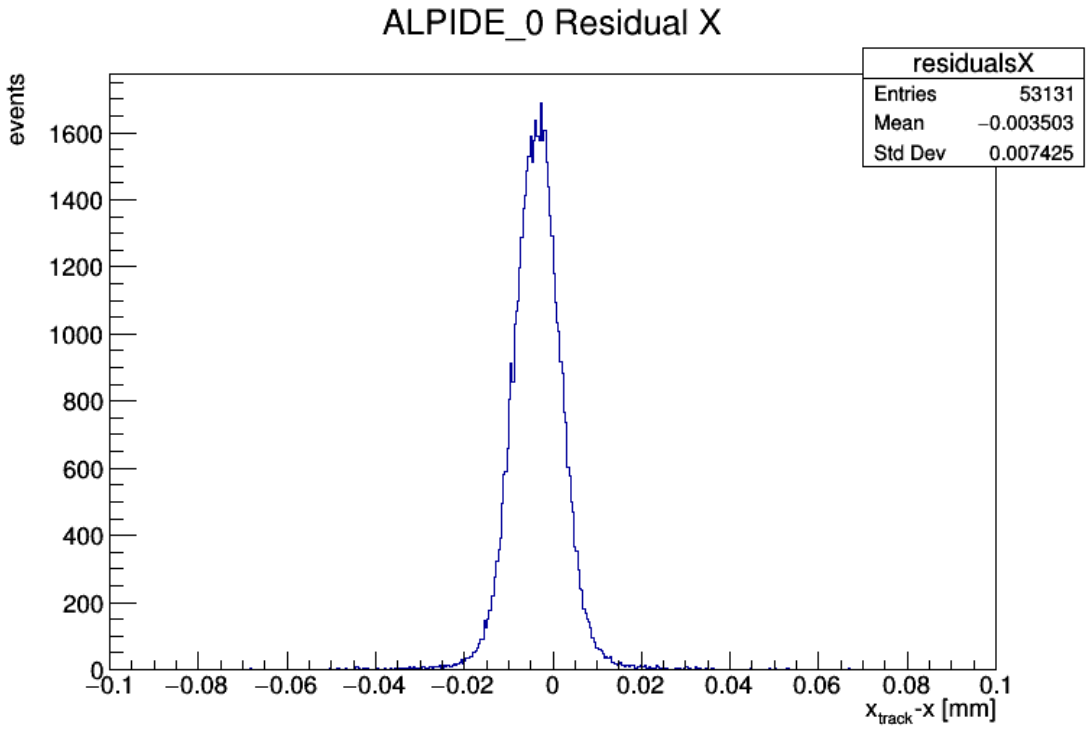

Figure 3.4: Plot of the residuals distribution, in x direction, for a reference plane, as it is returned by the [Alignment] module of Corryvreckan. The Gaussian shape suggests that the alignment procedure has been completed in the right way.

```
[ALPIDE_0]
mask_file = "../masks/ref-plane0.txt"
material_budget = 0.001
number_of_pixels = 1024, 512
orientation = -0.740949deg,-0.327732deg,-0.0127197deg
orientation_mode = "xyz"
pixel_pitch = 29.24um,26.88um
position = -0.004um,-0.465um,-93.2144mm
roi = [[0,0],[0,512],[1024,512],[1024,0]]
role = "reference"
spatial_resolution = 5um,5um
time_resolution = 2us
type = "alpide"
```

Figure 3.5: Particular of an updated geometry file for the first tracking plane of ALPIDE type in a beam telescope. After having completed the alignment procedure, the precise information on the position is updated and used for the analysis.

Once the alignment procedure is complete, a new geometry file is produced taking into account the displacements of the relative positions between the planes and of the rotation in the x, y plane that could not be measured manually, and the geometry is not changed anymore. An example is shown in Figure 3.5.

This file constitutes the input file for the final analysis procedure of the DUT, which is essentially divided into the `[AnalysisDUT]` and `[AnalysisEfficiency]` modules. From now on, the updated geometry file is used to reconstruct tracks with the reference planes: then, the tracks are matched to clusters on the DUT surface. Not all the reconstructed tracks are used as reference tracks for the DUT data analysis. During the alignment procedure, all tracks that have a reduced χ^2 greater than 3 are rejected.

[AnalysisDUT]

This Corryvreckan module aims to measure tracking-related quantities for the DUT, but above all the residuals in the x and y directions are calculated and plotted. These plots have been largely studied during the analysis, because of their strict relation with the spatial resolution, as described in Section 3.1. In Figure 3.6 the residuals distributions in the x and y directions are shown.

In a second time, I have implemented further plots by directly modifying the source code of Corryvreckan. Then, the program was recompiled. In particular, the histogram of the residuals (both in x and y) in 3D as a function of the (*row, column*) plane of the DUT has been implemented, using the `TH3F` ROOT class [18], such that Corryvreckan automatically can produce this plot when running the `[AnalysisDut]` module. An example is shown in Figure 3.7. The projection of this graph has been produced and

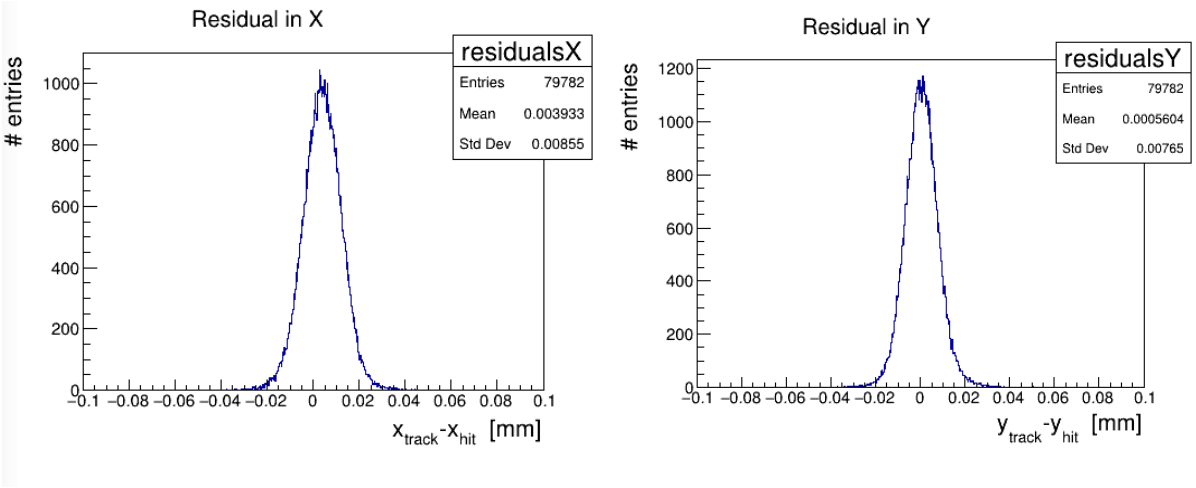

Figure 3.6: Example of the distribution of the residuals, in x and y, for the DUT of the beam test studied in this thesis.

analyzed in a second time and will be discussed in Chapter 4.

[AnalysisEfficiency]

The main purpose of this part of the Corryvreckan flow, which is also the last in the order of execution, is the study of the detection efficiency of the DUT. In particular, during the analysis, the total efficiency value (which is returned as a percentage by the Corryvreckan computation) and the 2D total efficiency map of the chip surface were examined. An example of the latter is illustrated in Figure 3.8. It is particularly useful when it comes to identifying any inefficient areas due, for example, to misalignment problems or a non-optimal description of the setup geometry.

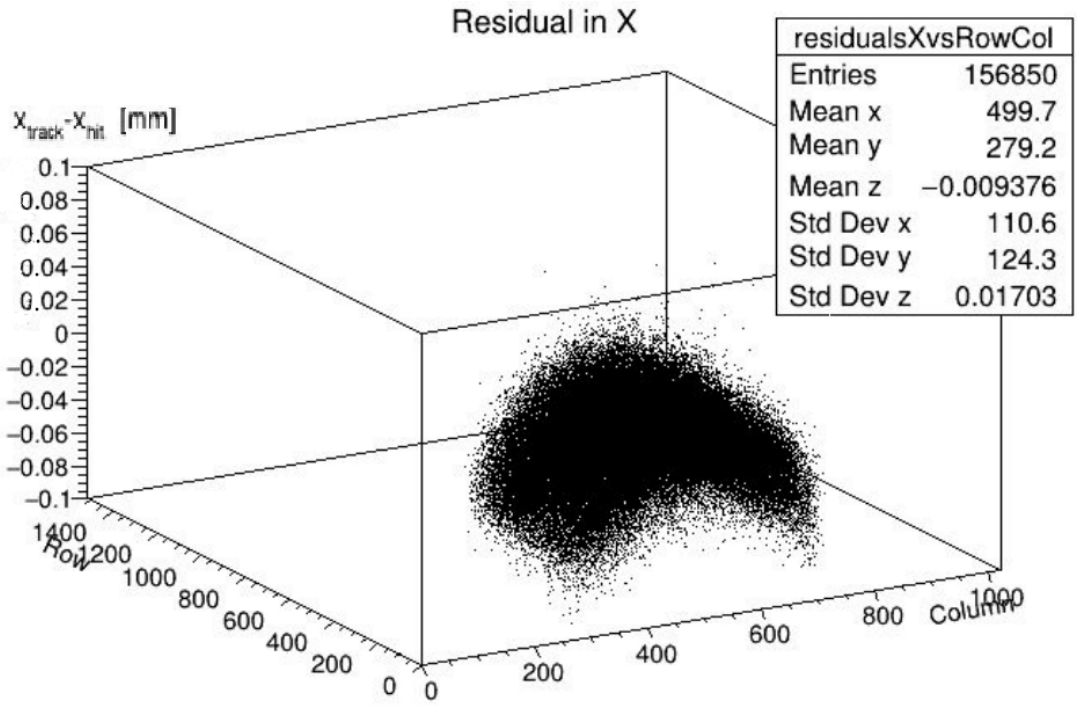

Figure 3.7: 3D distribution of the residuals in X, as a function of row and column of the DUT surface.

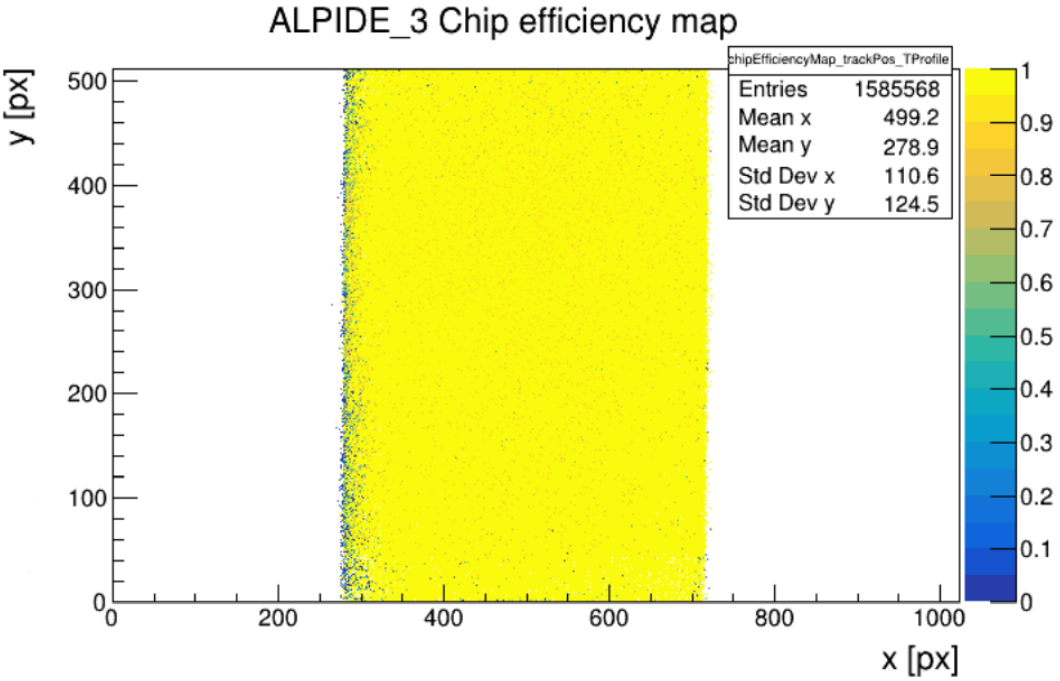

Figure 3.8: 2-dimensional Efficiency Map of an ALPIDE chip used as DUT. On the right the color scale of the efficiency values. The yellow colors refer to efficiency values over the 99% on the shown region. Plot took from the data analysis.

Chapter 4

Data Analysis of bent ALPIDE beam test performance

In this chapter, we will discuss the analysis of the data obtained during the August 2020 beam tests at DESY on curved ALPIDE chips. The analysis consists of the evaluation of the performances of a bent ALPIDE chip placed inside a telescope, which was composed of a total of 7 ALPIDE planes (6 reference planar planes + 1 bent Detector Under Test, DUT).

4.1 Experimental Setup

The beam test was performed at DESY beam test facility using a 5.4 GeV electron beam. The beam was produced by e^+/e^- pair conversion of bremsstrahlung photons using the e^+/e^- synchrotron DESY II. The particle type and energy selection was carried by a dipole magnet [19].

The experimental setup consisted of 7 ALPIDE chips, numbered from 0 to 6. The DUT ALPIDE_3 was placed in the center of the setup, bound to a cylinder with a radius R = 18 mm. The DUT place onto the cylinder can be seen in detail in Figure 4.1, while the detail of the setup is shown in Figure 4.2. In addition, a 3D model of the setup in scale is presented in Figure 4.3.

In FIGURE4.3, a 3D view of the setup is shown. The beam goes along the z axis, while the DUT vertical position (y axis) is adjustable so that the beam could be centered on different regions and uniformly hit the chip. All the reference planes work at $V_{bias} =$ 0V, while the DUT works at $V_{bias} = 0$V.

Two scintillators plus photomultipliers put in coincidence - placed before and after the telescope - constitute the trigger system. The separation time between the events, limiting the rate of the trigger is $\Delta t = 100\mu$. In addition, there is a veto 50 μs on triggering after a scintillator output signal.

The data acquisition process was based on the `EUDAQ2` [20] framework, with runs

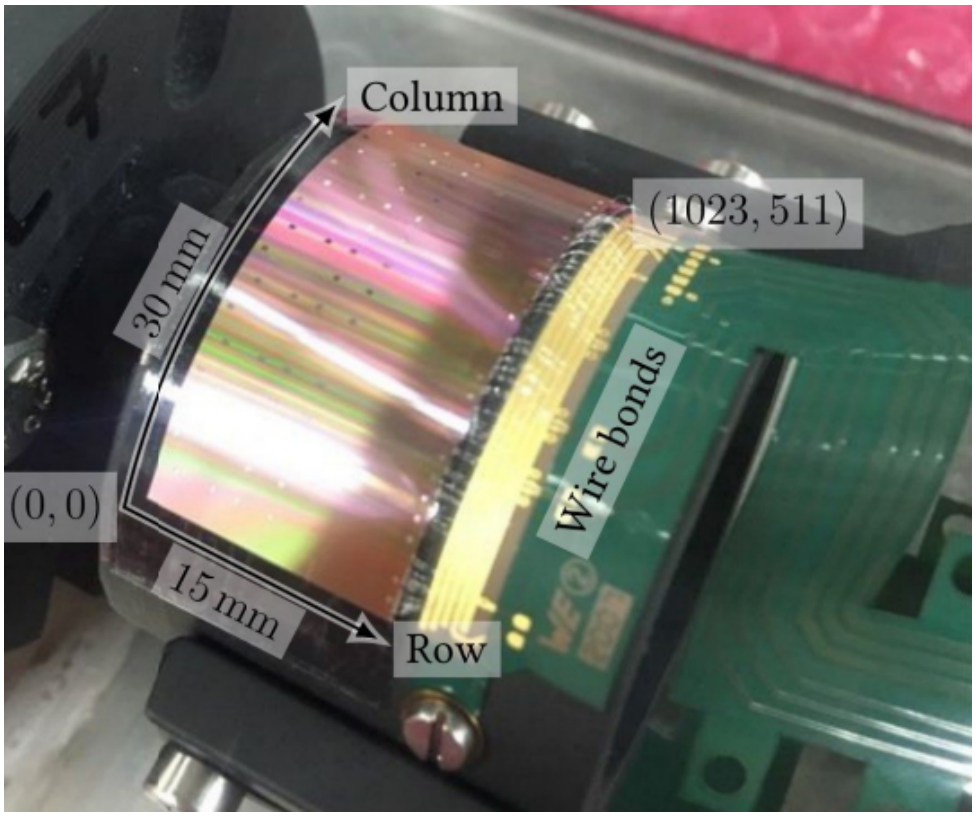

Figure 4.1: Detail of the DUT ALPIDE chip used in the beam test.

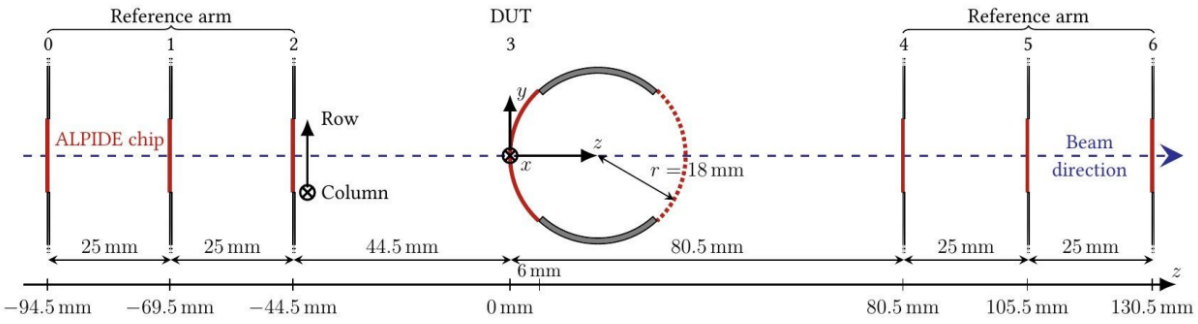

Figure 4.2: Scheme of the setup of the beam test.

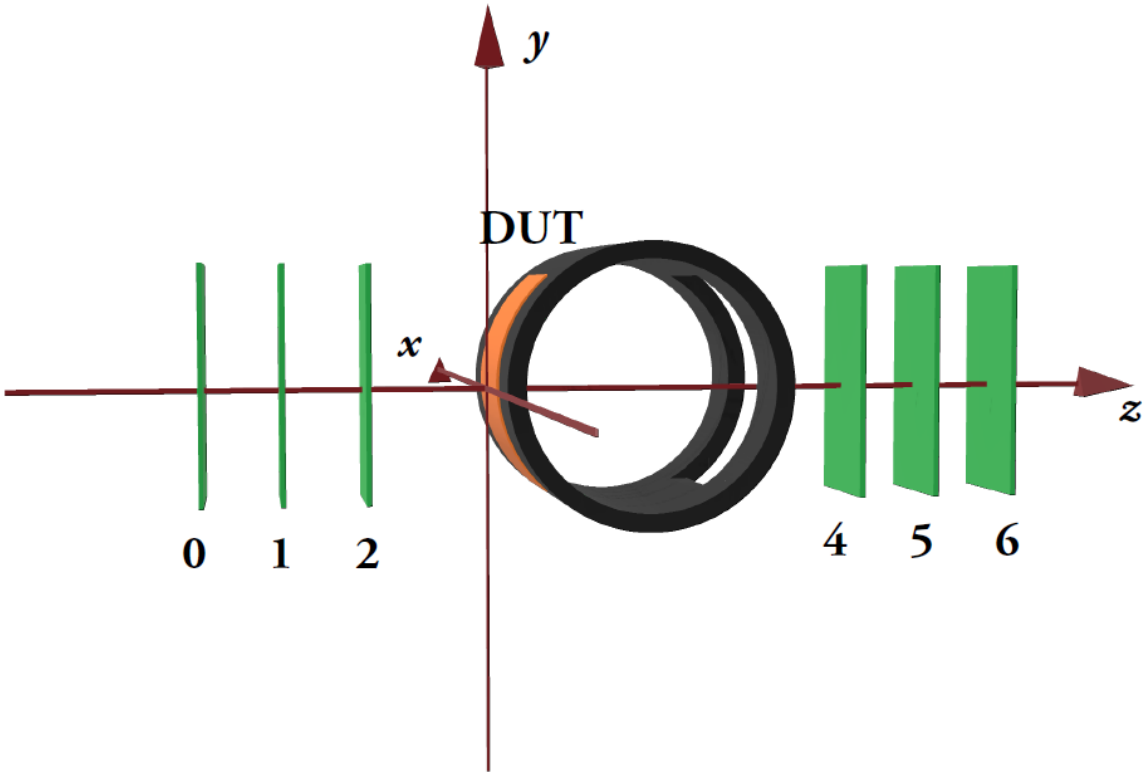

Figure 4.3: 3D scale scheme of the August 2020 beam test setup.

each one made up of about 300k events. Each run takes data scanning the whole DUT surface. In the context of this thesis work, 32 runs have been analyzed.

4.2 Update to geometry description

Since the geometry of the experimental setup is also described within Corryvreckan, the part of the source code related to the geometry description had to be updated. Therefore, I have directly modified the source code to better describe and finally match the bent geometry of the DUT, implementing a coordinate transformation written in C++. In this section, the contribution to the final geometry code description and the related tests will be presented.

4.2.1 Coordinate System and Geometry file

The coordinate system, as anticipated in the section on the description of the setup, sees the beam running along the z axis and the DUT free to rotate around the x axis thanks to the cylindrical support with radius R = 18mm. Recall that the *global coordinates* correspond to the $(x_{global}, y_{global}, z_{global})$ set of the laboratory reference frame, while the *local coordinates* describe the pixel position (x_{local}, y_{local}) on the surface of the DUT, in unit of pixel number.

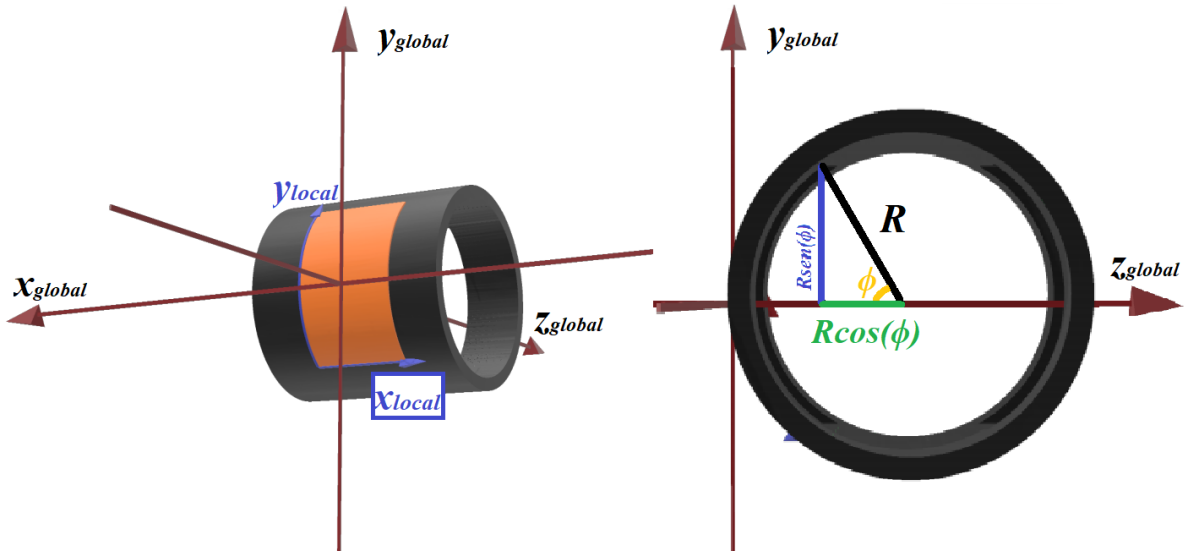

Figure 4.4: On the left, 3D representation of the global and local reference frames, the one of the laboratory system and the DUT plane, respectively. On the right, projection of the cylindrical support on the (y, z) plane.

It is possible to describe the position of a hit $(x_{0,local}, y_{0,local})$ on the ALPIDE surface in global coordinates, thanks to a simple change of variable that takes into account the bent geometry of the DUT as a function of the angle ϕ, as represented in Figure 4.4.

The change of coordinates is the following:

$$\begin{cases} x_{global} = -x_{local} P_x \\ y_{global} = R sen(\phi) \\ z_{global} = R - R cos(\phi) \end{cases} \tag{4.2.1}$$

where

$$\phi = \frac{y_{local} P_y}{R}. \tag{4.2.2}$$

P_x and P_y are the pixel pitches in x and y directions on the chip plane. The change of coordinate of eq. 4.2.1 has been translated in C ++ and implemented in the source code of Corryvreckan, in a specific module named `detector` and devoted to the geometrical description of the setup and the Detector Under Test.

To accomplish this task, a pre-existing coordinate transformation called `local_to_global` and the corresponding inverse function named `global_to_local` have been updated.

Consequently, the program was recompiled with the updated geometry: the resulting geometry has then been plotted with ROOT and it is shown in Figure 4.5. In Figure also a sample reconstructed track is represented, with the associated clusters used for the reconstruction.

Moreover, a test run was chosen and intensively analyzed to check the total efficiency of the sensor (see Section 3.1 and the values of the residuals in x and y coordi-

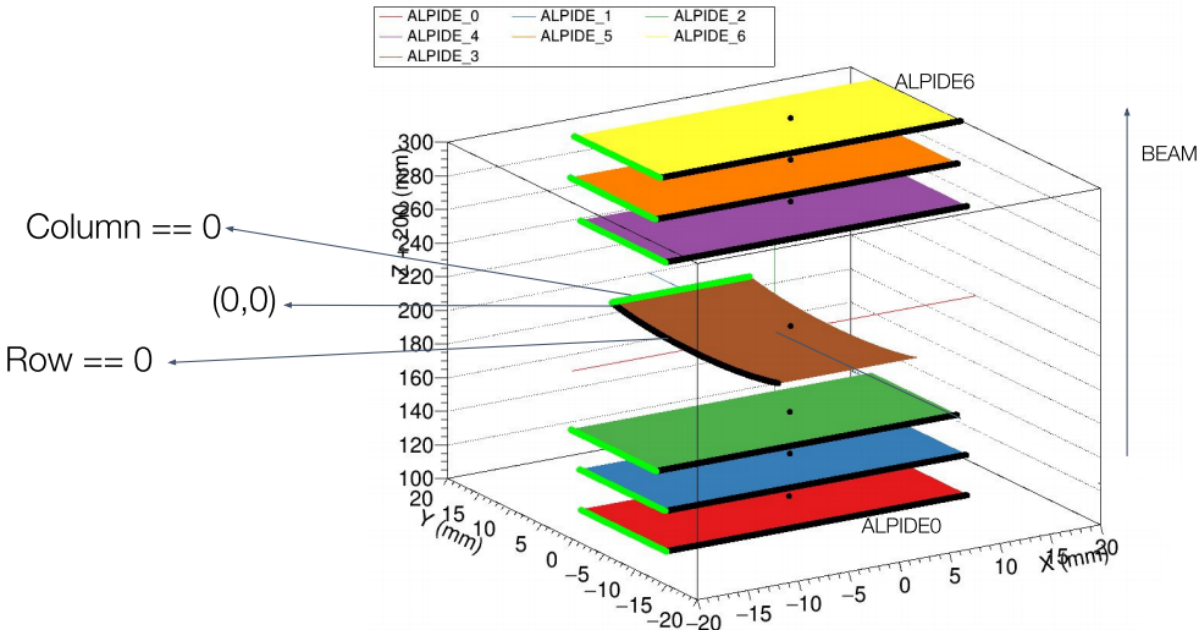

Figure 4.5: 3D plot of the geometry of the system after the modification in the Corryvreckan code. The origin of the laboratory system (global coordinates) coincides with the center of the bent chip, tangent to the cylindrical support. The black dots on the chip surfaces correspond to the clusters associated with a single track reconstruction.

nates. In Figure 4.6 the 2D efficiency map of the DUT, after the change in the geometry implementation, is shown. All the efficiency values presented after the update are over the 99%. In addition, in Figure 4.7 the plot of the residuals in x direction after the update is shown.

All the results of this thesis have been obtained with the updated geometry description, and they will be discussed and presented in the following sections.

4.3 Data Analysis

4.3.1 Analysis Strategy

In the following section, the most significant results of the performance of the DUT studied during the beam test of August 2020 will be presented.

The goal was the study of the efficiency and spatial resolution of an ALPIDE chip for the first time curved down to a radius of 18 mm, to check if there were deviations from the case of non-bent ALPIDE sensors in terms of performance. To do this, the new bent geometry has been implemented by deeply modifying the Corryvreckan source code as described in Section 4.2. In addition, a program in ROOT C ++ was also written to be able to perform the analysis of the Corryvreckan output .root files to study the DUT performance.

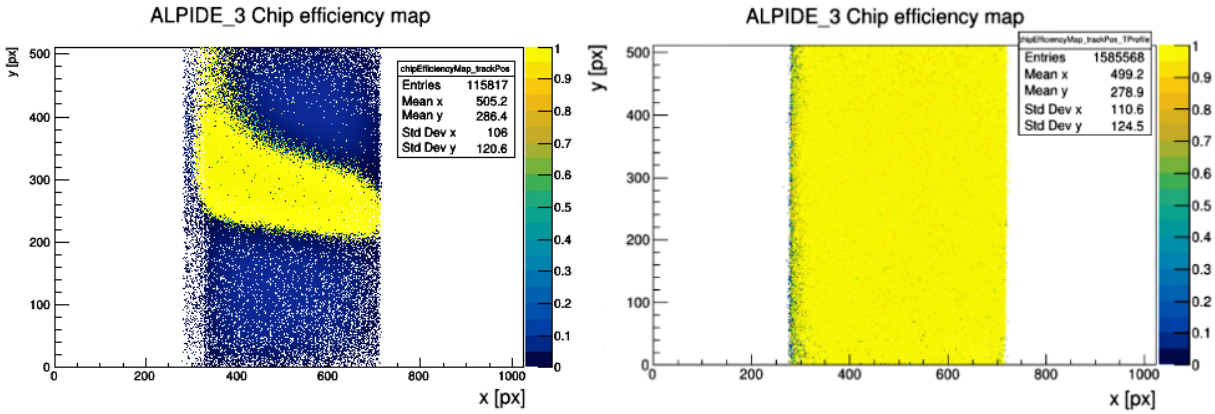

Figure 4.6: Left: efficiency map of the DUT, in a single run, before the update to geometry description implementation. Right: after the geometry update, the map shape becomes uniform and the efficiency is over the 99% on the whole chip surface.

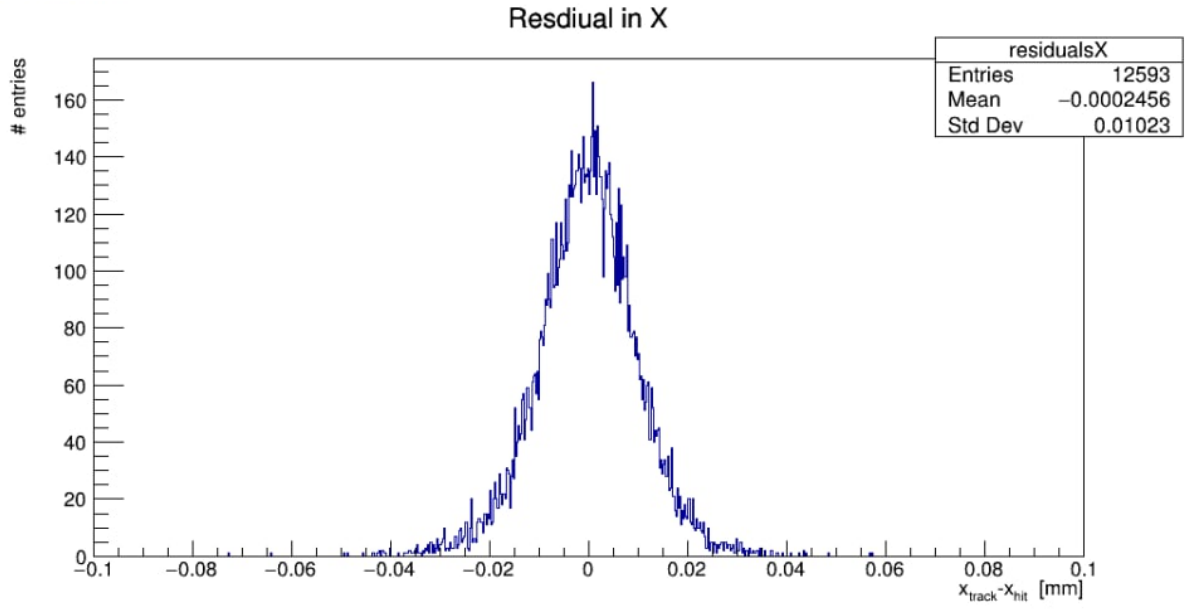

Figure 4.7: Distribution of the residuals in x of the DUT after the update to geometry description. The full chip surface, without cuts, has been considered for the efficiency analysis.

The program has aims to extract the physical quantities required for data analysis, such as the cluster size, the residuals sigma σ_{res}, the detection efficiency and the spatial resolution of the detector. Since the run number is high, it is not convenient to extract data one-by-one by terminal or by using ROOT `TBrowser` [18]. Therefore, the framework has been specially implemented for the simultaneous analysis of multiple runs - each presenting different threshold and average cluster size values - according to these specific needs.

Firstly, a macro-block in ROOT C++ devoted to the multiple input-output management of `.root` files have been developed: this is the core of all the others because it allows opening a variable number .root files inside the folder/path of interest and loops every type of operation over the file set.
When opening a `.root` file, the program extracts the run number and the mean of the cluster size corresponding to that run. In this way, **each run is labeled** using a string containing the run number and it is possible to analyze multiple files in parallel, distinguishing the runs among each other depending on their run number and the associated threshold or average cluster size value.
Therefore, each macro starts from this block and then completes its specific task, like the extraction of the residuals or of the total efficiency. Once the run number or the cluster size of the runs are known, the program lists them in a `.csv` file, which can be read or modified a second time. This file constitutes the input for the other programs of the framework and allows for a comparison of many variables (residuals, efficiency) as a function of the run number[1] or the cluster size, over different runs.

This approach allows to study of the behavior of many quantities as the run number changes, but only with one execution of the program.

The **charge threshold** is a key parameter defining the ALPIDE performance. The threshold can be adjusted by changing some parameters, namely `ITHR` and `VCASN`. These parameters are related with the ALPIDE in-pixel electronic circuitry [21]. Higher values of the first correspond to higher charge threshold values, while as `VCASN` decreases, the charge threshold decreases, too. It is possible to study the relationship between charge threshold performing a *threshold scan*; in Figure 4.8, the threshold scan of the bent ALPIDE used as DUT is shown. For the aim of this work, then from now and on, I will always refer to the charge threshold (without further details on `ITHR` or `VASN`). Moreover, an additional separate set of runs with higher statistics has been used to perform the preliminary studies, which will be described in detail in Section 4.3.2. As anticipated above, each run session corresponds to a different threshold value and takes data scanning the whole DUT surface. As the threshold changes, also the mean of the cluster size on the chip surface does, too: when the first increases, the cluster size in the chip decreases.

[1] It is also possible to select only a certain run number range/data taking period of interest.

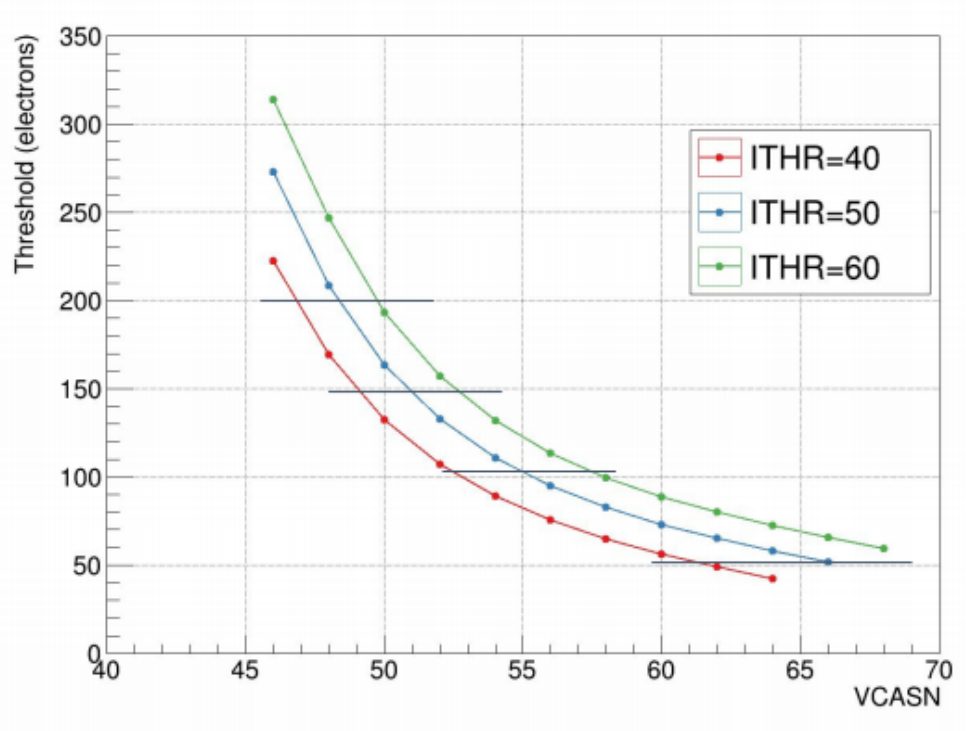

Figure 4.8: Threshold scan plotted as a function of VCASN for the ALPIDE chip used in the August 2020 beam test.

The main steps of the data analysis workflow are the following, each one corresponding to a different code devoted to the specific task:

- **run checking**: quick checks of the chip performance over a variable number of runs by extracting some fundamental plots from .root Corryvreckan output files. In the early steps of the analysis, many checks on a single run have been made to adjust many parameters related to the geometry and the alignment using Corryvreckan.
- **cluster size**: the trend of the cluster size was first studied as a function of the run number and the threshold and several plots were produced to study the dependence on the average cluster size.
- **residuals**: as mentioned in Section 3.1, their study is fundamental to derive the spatial resolution. For this reason, their behavior has been studied in-depth writing dedicated programs.
- **efficiency**: study of the total value of the detection efficiency of the detector, as previously defined in Section 3.1. The efficiency value has also been studied as a function of the run number and cluster size.
- **resolution:** the resolution is computed as in equation 3.1.1. The tracking resolution of the beam test telescope was computed by using a dedicated tool [22].

4.3.2 Run checking

At first, a block of code was developed to be able to perform a quick check of the quality of the output files and plots as they are returned by running Corryvreckan on the raw files. The program extracts the plots from the .root files: the most significant are the **2D efficiency map** of the chip (which allows a global check of the total efficiency value over the chip surface, an example is shown in Figure 4.9) and the distributions of the **residuals** in x and y (which are expected to be Gaussian, see Figure 3.6), which were repeatedly checked and analyzed especially when the part of the Corryvreckan code describing the geometry of the DUT was updated.

Determination of the ROI

Once the most appropriate geometric description was decided, the chip showed uniform efficiency values on several runs and always above 99%.

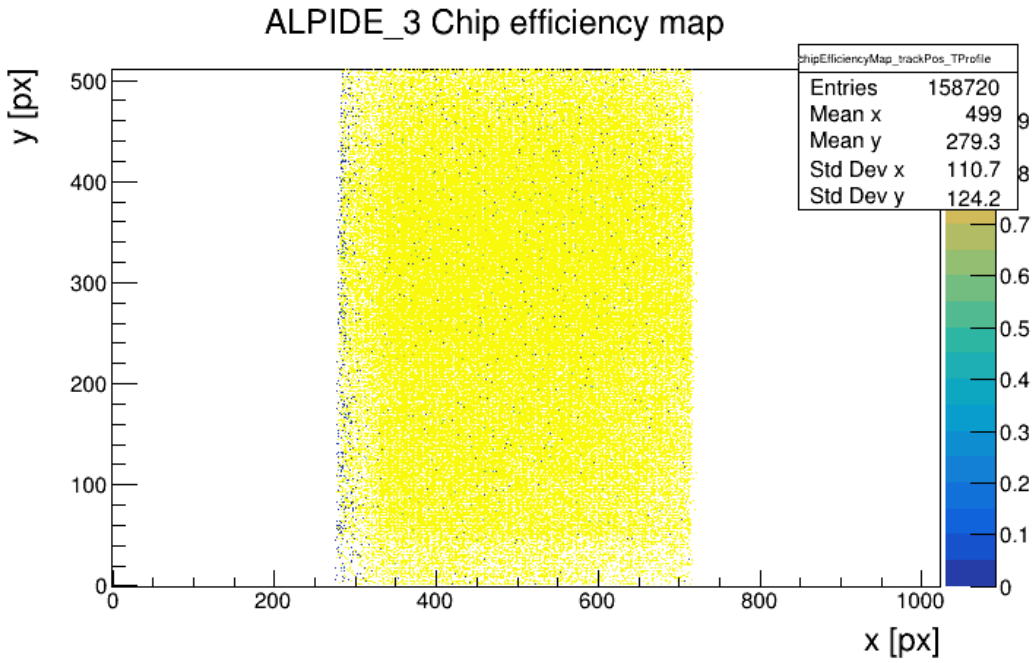

Figure 4.9: 2D efficiency map of the DUT before the application of the windows size as ROI. The efficiency value is attested over the 99% on the whole chip surface.

After passing this first test, the study of the residuals in both x and y directions has been performed. The reduction of the width of the residual distribution "as much as possible" is fundamental as it largely affects the effective value of the spatial resolution. At the same time, the behavior of their sigma on the surface of the chip was studied in order to determine the **Region Of Interest** (ROI). This work was necessary since not all the chip surface was "free"[2], but a large part was superimposed on the cylindrical

[2]We recall that the whole ALPIDE surface accounts for 1024×512 pixels.

support to which the DUT was bound, thus resulting in a higher material budget in correspondence of the cylindrical support and a **window** free from that, being approximately 5 mm wide, as it is shown in Figure 4.10. The study of residuals is particularly appropriate in this case because a much lower σ_{res} is expected in correspondence of the window, due to a lower material budget, which as described in Section 1.4.1 largely affects the spatial measurements in tracking.
Therefore, this study also made it possible to accurately determine the coordinates of the ROI, which values have been then provided as input to the geometry file during the final analysis via Corryvreckan.

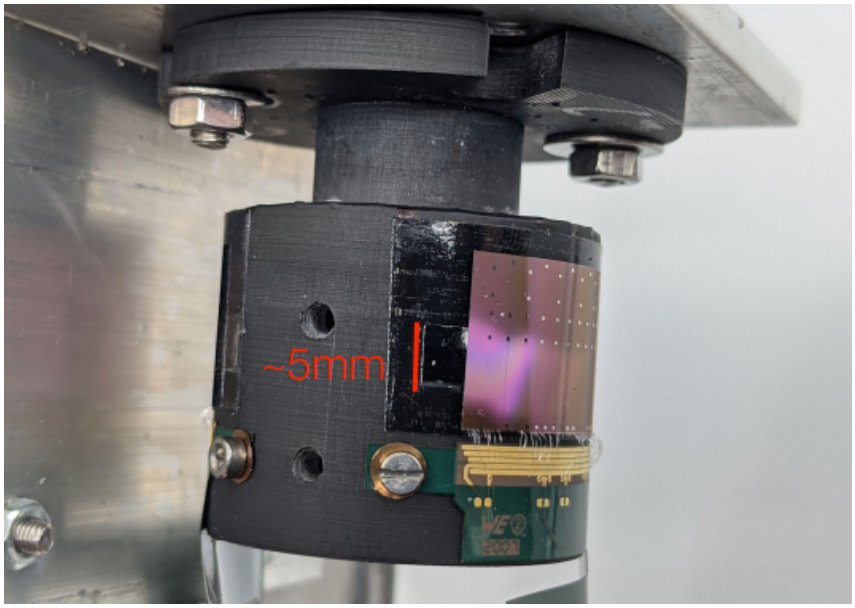

Figure 4.10: Photo of ALPIDE placed on the cylindrical support. The height of the material-free window in the cylindrical support is highlighted in red.

To study this effect, 10 runs from the August 2020 data-set with **higher statistics**, were chosen and studied to this purpose. Then, the single .root files of every single run from this dataset have been merged using the ROOT `hadd` function[3], to study the associated σ_{res} and see if there could be improvements due to the higher statistics (10 runs versus single run).
To reach this goal, I have modified Corryvreckan (see Section 3.2) in the analysis phase. I have written and added to the source code a 3D plot of the residuals as a function of the (*row, column*) position, such that Corryvreckan returns it now as an output plot when executing the module `[AnalysisDUT]`. Then, I have performed the 1D and 2D projection, with respect to the z axis and the $x - y$ plane, of the sigma of the residuals σ_{res} from the 3D new histogram created before. The results of these projections have been plotted and studied.

[3]This function allows adding together ROOT histograms plotting the same quantities from different .root files.

The first produced plot was the DUT **2D σ_{res} map**, produced thanks to the ROOT function `FitSlicesZ()`[18], that allows performing a fit to a 3D graph, directly plotting the 2D distribution of the residual sigma on the surface of the DUT, as shown in Figure 4.11. As the number of runs considered at a time increases, the shape of the window becomes more easily visible, like in Figure 4.12 and the ROI can be easily determined. At the end of the process, the coordinates chosen for the ROI were the following:

```
roi = [0, 237], [0, 423], [1024, 423], [1024, 237].
```

A particular of the new geometry file after the implementation of the new ROI is shown in Figure 4.16, where also the positions of the clusters associated to a single track are shown as black dots. The whole window is highlighted on the DUT surface. In Figure 4.13 the 2D efficiency map of the chip after the selection of the ROI inside of the Corryvreckan analysis is shown.

The second plot the σ_{res} **1D-projection** on a **single bin** of the DUT. It allows checking in a sensible way the variation of the sigma as a function of the lower or higher statistics. Figure 4.14 shows the σ_{res} value for a single run, projected on a single bin located in-window. Figure 4.15 shows the same plot for the whole high statistics run dataset, with a sensible improvement due to the higher available statistics, so that the shape of the window becomes more distinguishable.

4.3.3 Cluster Size

As anticipated in Section 3.1, the *cluster size* is the number of pixels of a single cluster: in Figure 4.17 the distribution of the cluster size referred to the associated tracks for a single run is shown.
In this thesis, crucial quantities like the total efficiency and the spatial resolution of the DUT have been studied as a function of the chip cluster size. Therefore, the behavior of the cluster size as a function of the charge threshold has been studied to check the consistency with the expected ALPIDE cluster size trend. The size of the clusters created on the chip surface should decrease as the charge threshold of the pixels increases [4], as it is shown in figure 4.18.
Since the cluster size follows the predicted behavior plotted as a function of the threshold, it is possible to produce plots of the other quantities under study as the function of the cluster size. The values of the mean of the cluster size distribution for the whole analyzed dataset are listed in Table4.1.

[4]In ALPIDE, is possible to change the charge threshold for all pixels at the same time by changing the pixel amplifier parameters.

Run Number	Threshold $[\#e^-]$	Mean of the cluster size distribution
355212049	169	2.48
355212050	132	2.88
355212051	107	3.22
355212052	89	3.53
355212053	75	3.83
355212054	64	4.12
355212055	56	4.40
355212056	49	4.71
355212057	42	5.06
355234406	273	1.82
355234407	208	2.19
355234408	163	2.56
355234409	132	2.91
355234410	110	3.20
355234411	95	3.47
355234412	82	3.72
355234413	73	3.96
355234414	65	4.21
355234415	57	4.47
355234416	51	4.79
356095953	313	1.62
356095954	246	1.94
356095955	193	2.30
356095956	157	2.62
356095957	131	2.92
356095958	113	3.18
356095959	99	3.42
356095960	88	3.64
356115029	80	3.85
356115030	72	4.06
356115031	65	4.30
356115032	59	4.60

Table 4.1: In this table, the run number and the related values of threshold, and the mean of the cluster sizes to the associated tracks for the DUT are reported for all the analyzed data-set.

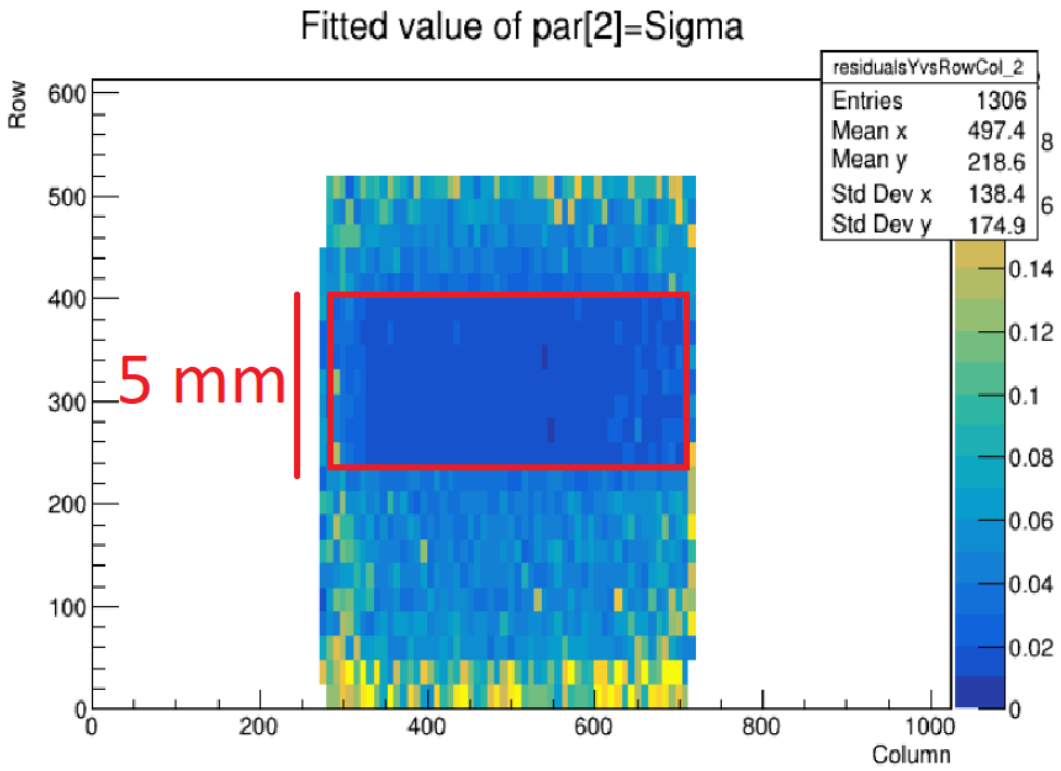

Figure 4.11: 2D projection of the residuals y sigma on the DUT surface (see color scale on the right). The plot refers to a single run with high statistics. The height of the window is highlighted in red.

4.3.4 Residuals

The study of the residuals is closely linked, as already mentioned in eq. 3.1.1 of Section 3.1, to the value of the spatial resolution of the sensor. The distribution of the residuals on the chip surface for both x and y direction should follow a Gaussian: lower the sigma σ_{res}, then better the resolution of the detector. In particular, for each run the plot of the residuals has been extracted from the .root Corryvreckan output file, then the distribution has been fitted with a Gaussian and the sigma has been extracted, like in Figure 4.19. The fact that the distribution is Gaussian and centered to zero tells that the geometry positions are correct and the alignment procedure was performed in the right way. The plot in Figure 4.20 shows the behavior of the σ_{res} in x as a function of the run number and the cluster size, respectively. As expected, an increasing cluster size leads to a better residuals value (due to *charge sharing*) up to a value of the cluster size mean $\sim$3. After this value, they get worse, probably due to the too low threshold, which means that too much noise might have been detected in this region.

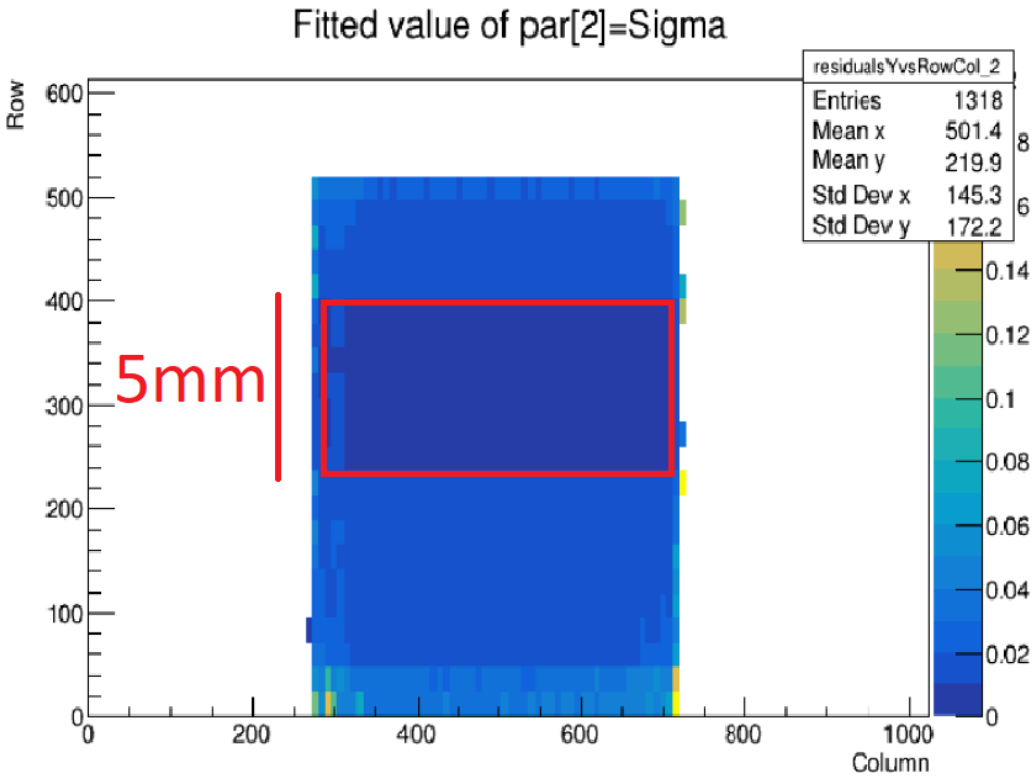

Figure 4.12: 2D projection of the residuals y sigma on the DUT surface (see the color scale on the right). The plot refers to 10 runs with high statistics, whose root files have been merged before creating the histogram. The height of the window is highlighted in red.

4.3.5 Resolution

The study of spatial resolution is of fundamental importance, because together with efficiency, as already mentioned, it provides the most reliable parameters regarding the performance of the DUT. In this analysis, the residuals are defined as $x_{track} - x_{hit}$ and the value of the resolution is computed with equation 3.1.1, as anticipated in Section 3.1. The exact computation of σ_{track} was performed through a framework specially developed for this purpose, in which it was possible to enter the exact distances between the tracking sensors and obtain the tracking resolution for the DUT [22]. In Figure 4.21, the tool with the August beam test setup configuration is shown: as indicated in the configuration, in the original setup there were 2 DUTs, but only the first has been studied, since the second was not working. However, the presence of the second DUT has to be taken into account in the σ_{track} computation, too.

Analogously to the study of the residuals, also the resolution has been studied: once the residuals were extracted and their sigma calculated, the resolution was calculated and plotted using equation 3.1.1. The plots of the resolution in x direction as a function of the cluster size are shown in Figure 4.22: the trend as expected is the same as the one presented by the residuals but shifted down. When compared to the flat chip case

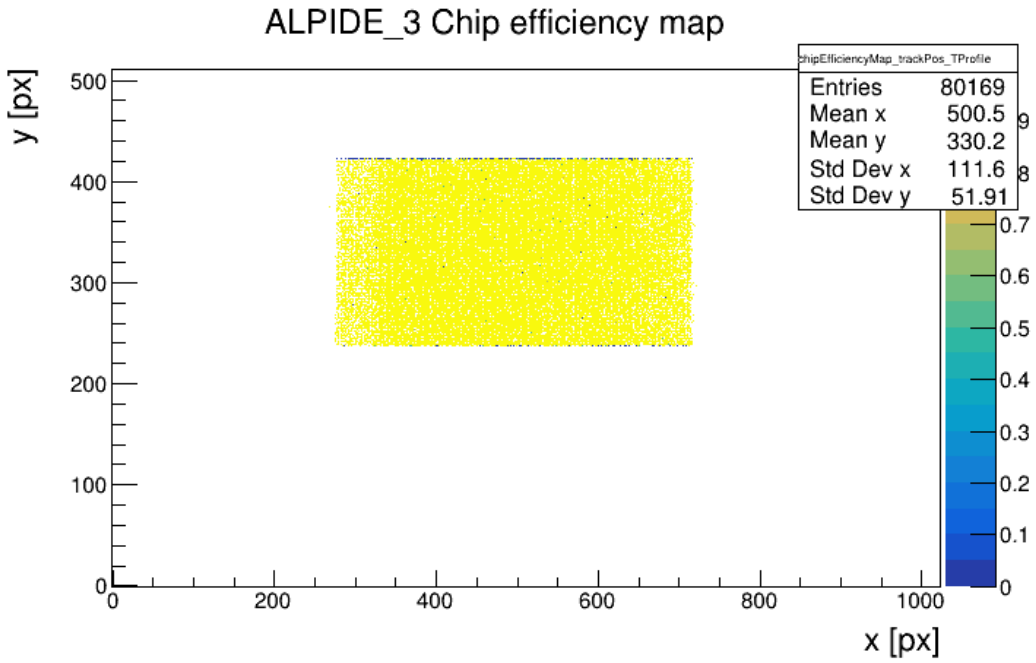

Figure 4.13: 2D efficiency map of the DUT after the application of the windows size as ROI. The efficiency value is attested over the 99% on the whole chip surface.

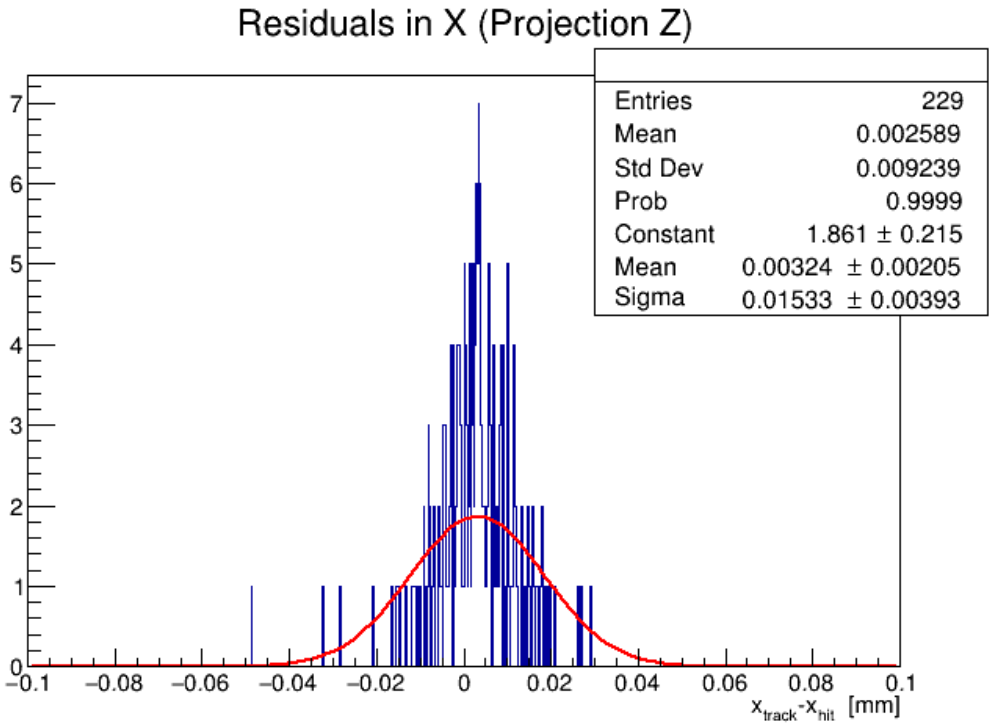

Figure 4.14: Projection of the residuals x as a function of row and column onto a single bin located inside the window. The plot is taken from the high statistics run dataset.

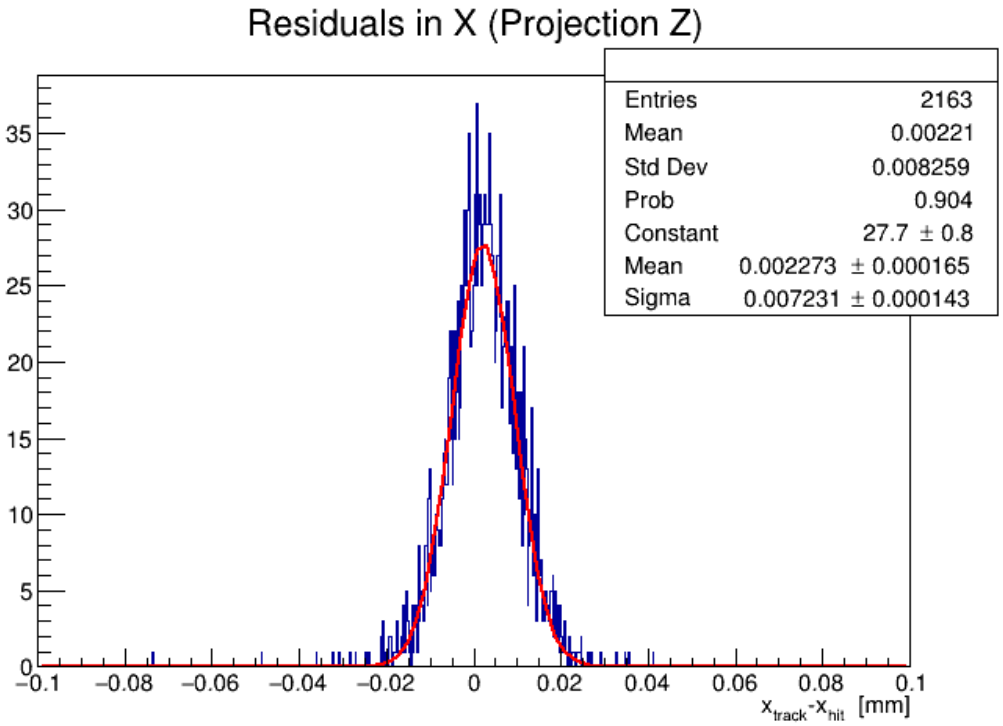

Figure 4.15: Projection of the residuals x as a function of row and column onto a single bin located inside the window. The plot is taken from the whole high statistics run dataset merged in a single .root file, showing a sensible improvement in the σ_{res} value.

```
[ALPIDE_3]
type = "ALPIDE"
position = 0mm,0mm,0mm
number_of_pixels = 1024,512
pixel_pitch = 29.24um, 26.88um
spatial_resolution = 5.00um, 5.00um
time_resolution = 2us
material_budget = 0.0005
coordinates = "cartesian-bent"
orientation = 0deg,0deg,270deg
bent_axis = "column" #or row (short side)
radius = -18.11mm
flat_part = 0mm
# y_0 = 0mm
# radius = 18mm
orientation_mode = xyz
mask_file = "../masks/dut-plane3.txt"
# roi = [100, 50], [100, 450], [900, 450], [900, 50] # strict
# roi = [0, 0], [0,512], [1024, 512], [1024, 0] # wide
# roi = [0, 163], [0, 349], [1024, 349], [1024, 163] # inside-window, too low
roi = [0, 237], [0, 423], [1024, 423], [1024, 237] # inside-window
role = "DUT"
```

Figure 4.16: Detail of the DUT input parameters in the final version of the Corryvreckan geometry file after the ROI determination.

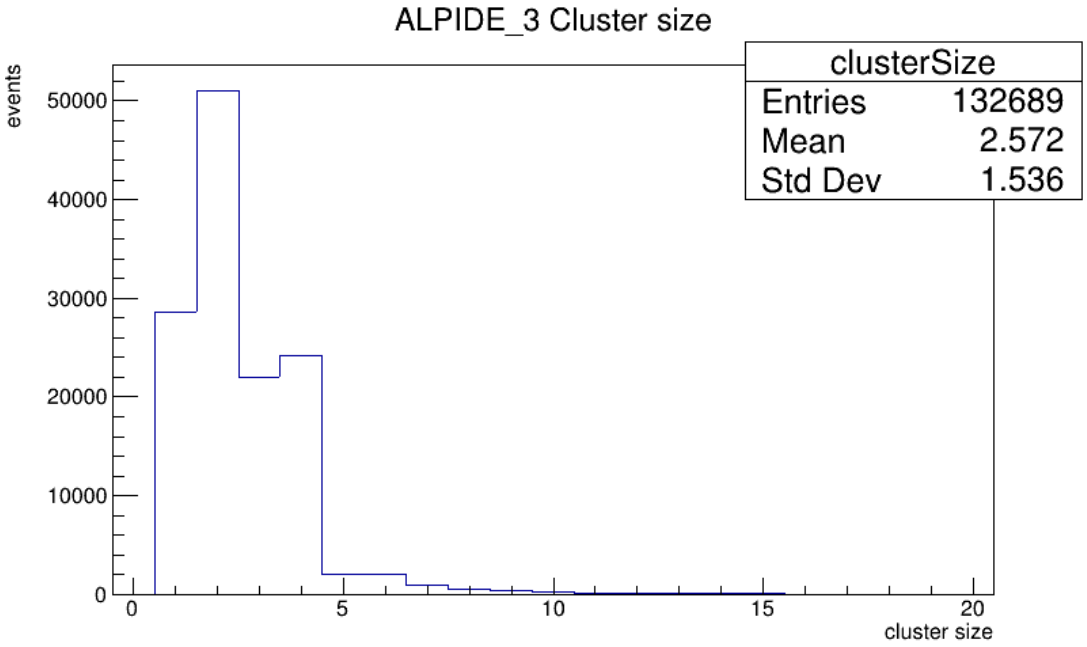

Figure 4.17: Distribution of the Cluster Size of the tracks for a single run.

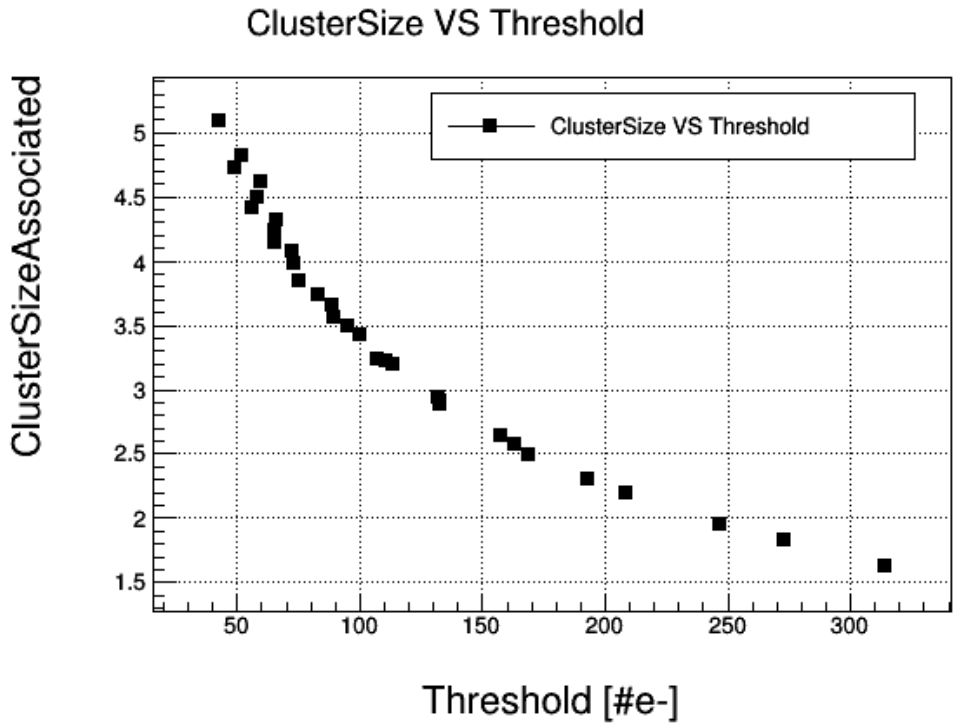

Figure 4.18: Mean of the cluster size distribution for the whole dataset, plotted as a function of the charge threshold. Each point represents a single run. The curve follows the same decreasing trend as for the flat case chips.

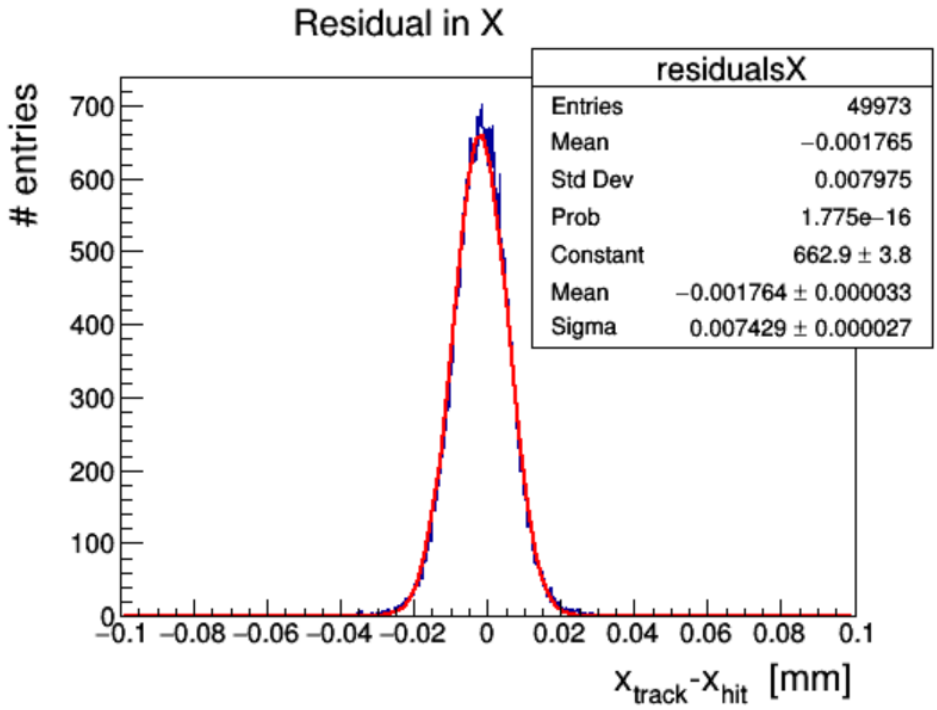

Figure 4.19: Plot of the DUT residuals distribution in x direction for a single run, calculated as the difference between the track intercept with the DUT surface and the position of the cluster associated to that track. The red curve represent the result of the gaussian fit.

(Figure 4.23), a similar trend can be observed. The minimum of the bent chip resolution is 1 μm higher with respect to the flat chip case: this small difference is still under study and might be caused by factors like a non-optimal implementation of the bent geometry for the DUT, or might be due to some misalignment. But in general, it can be said that a good agreement has been reached between flat and bent configuration.

4.3.6 Efficiency

Finally, below are the values of the efficiencies as the value of the cluster size varies, as shown in Figure 4.24. The efficiency values found for the DUT after the change in the framework describing the geometry have always been above 99 %, with a further improvement up to peaks of 99.55 % after the input of the final ROI in the geometry file of Corryvreckan. As expected, the trend at low cluster size values can be explained by the corresponding too high threshold. The bent chip has good performances showing uniform efficiency values almost everywhere, with no deviations and in agreement with the flat chips performances. In general, it must be evidenced that the best working operation interval for these chips is around the threshold of 100 $\#e^-$, at which the spatial resolution and the efficiency are optimized.

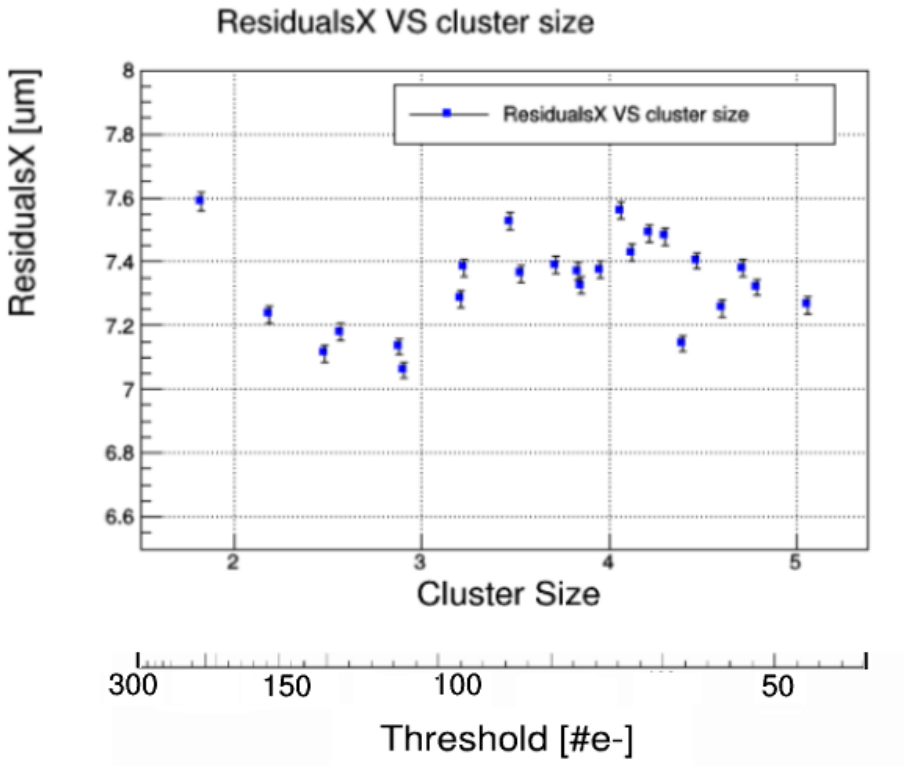

Figure 4.20: Sigma of the DUT residuals distribution in x direction as a function of the mean of the cluster size distribution. Each point corresponds to a single run. The plot includes the whole run data set.

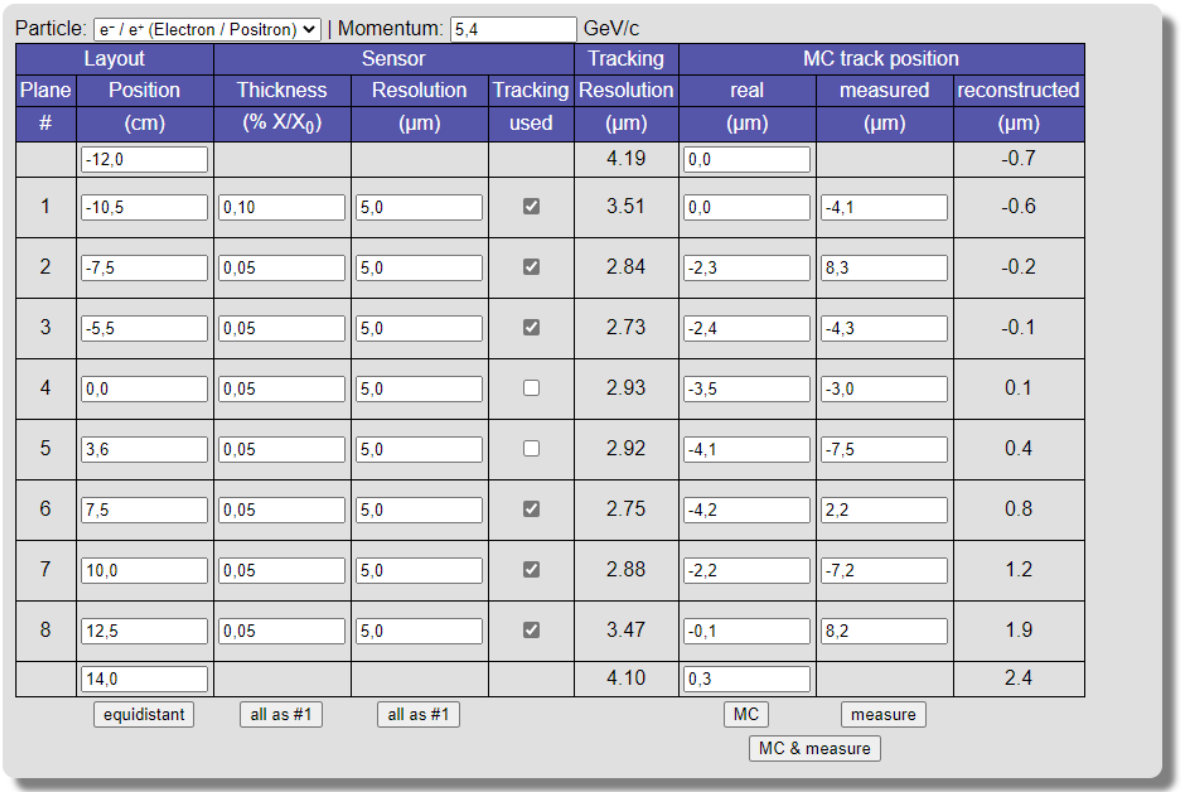

Particle: e⁻ / e⁺ (Electron / Positron) | Momentum: 5,4 GeV/c

Layout		Sensor			Tracking	MC track position		
Plane	Position	Thickness	Resolution	Tracking	Resolution	real	measured	reconstructed
#	(cm)	(% X/X_0)	(μm)	used	(μm)	(μm)	(μm)	(μm)
	-12,0				4.19	0,0		-0.7
1	-10,5	0,10	5,0	☑	3.51	0,0	-4,1	-0.6
2	-7,5	0,05	5,0	☑	2.84	-2,3	8,3	-0.2
3	-5,5	0,05	5,0	☑	2.73	-2,4	-4,3	-0.1
4	0,0	0,05	5,0	☐	2.93	-3,5	-3,0	0.1
5	3,6	0,05	5,0	☐	2.92	-4,1	-7,5	0.4
6	7,5	0,05	5,0	☑	2.75	-4,2	2,2	0.8
7	10,0	0,05	5,0	☑	2.88	-2,2	-7,2	1.2
8	12,5	0,05	5,0	☑	3.47	-0,1	8,2	1.9
	14,0				4.10	0,3		2.4

equidistant | all as #1 | all as #1 | MC | measure | MC & measure

Figure 4.21: Tool used for the telescope tracking resolution estimation. Image from [22].

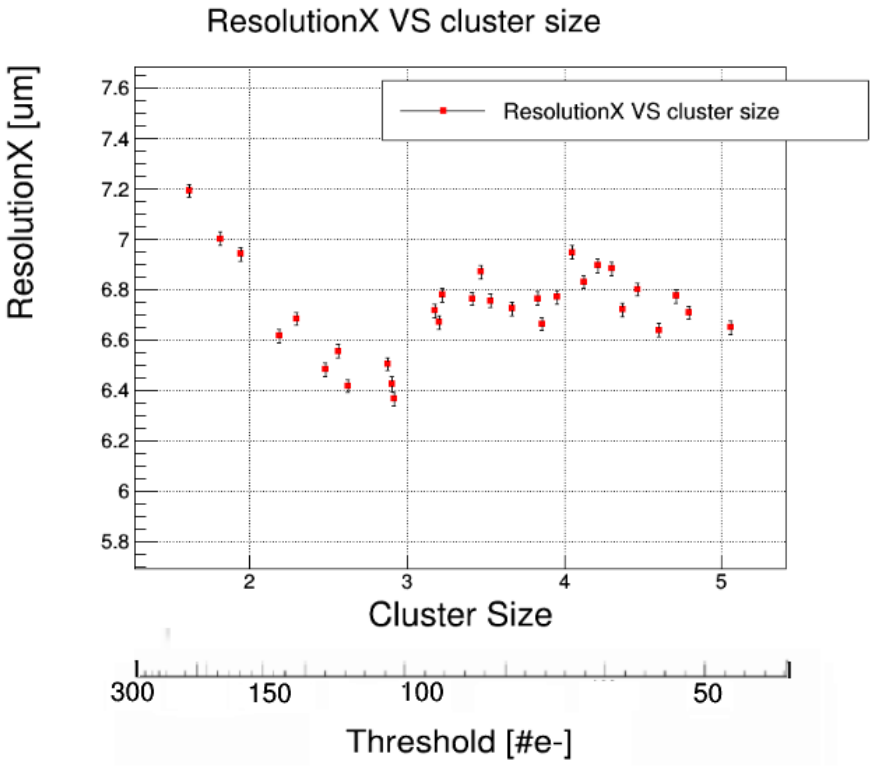

Figure 4.22: Spatial resolution in x direction of the bent DUT, plotted as a function of the cluster size. The minimum value of $\sigma_{sp} \sim 6.5$ μm is reached in the interval [2,3] of the mean of the associated cluster size distribution, corresponding to a 100÷150 $\#e^-$ threshold range. The plot includes the whole run data set. On bottom, also the threshold axis is present.

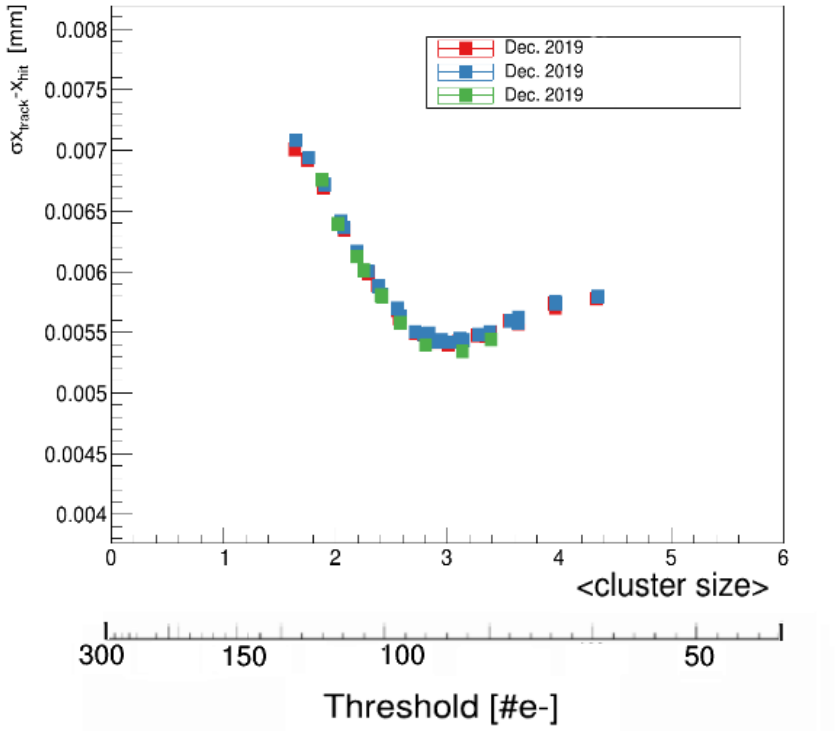

Figure 4.23: Spatial resolution of the flat ALPIDE chips in x direction, plotted for different runs as a function of the cluster size. On bottom, also the threshold axis is present.

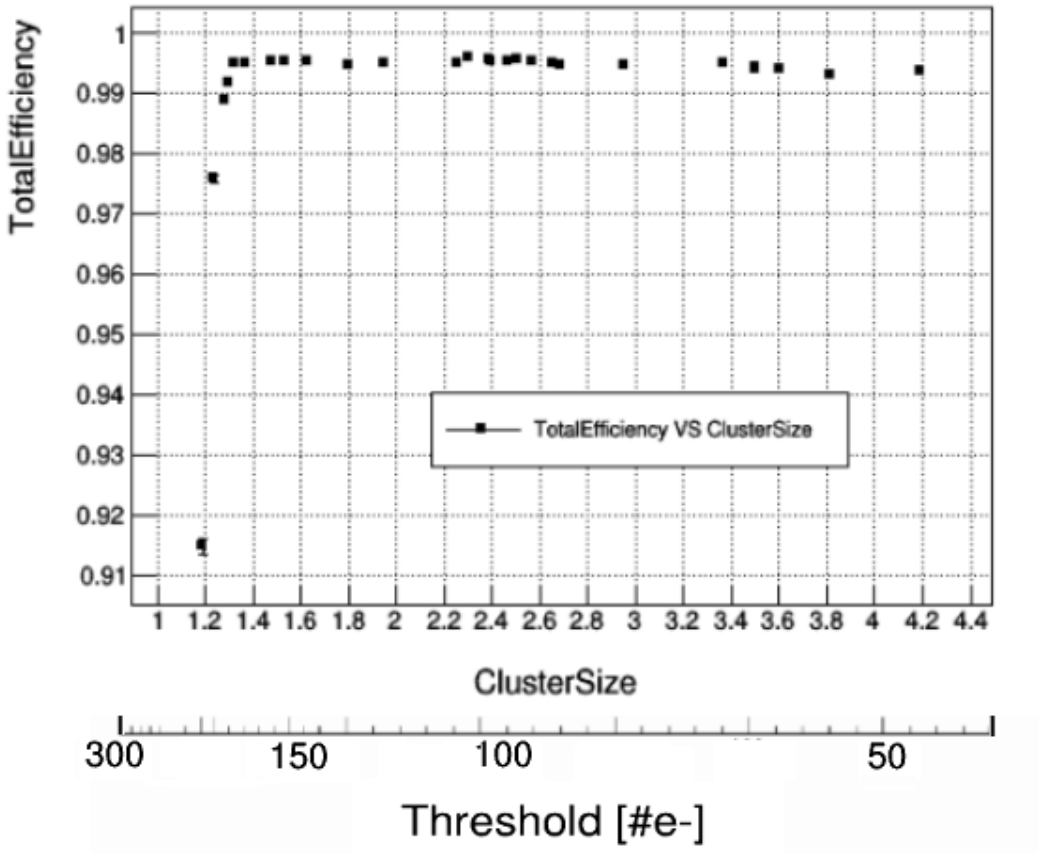

Figure 4.24: Total efficiency of the DUT plotted as a function of the mean of the cluster size distribution; each point represents a single run. Also the axis with the threshold values is indicated. The plot includes values from the whole data set. The efficiency values and their errors are returned by Corryvreckan by using the TEfficiency ROOT class functions[18].

Conclusions

The upgrade of the ALICE Inner Tracking System 2, the ITS3, is scheduled for the next Long Shutdown (LS3) of the Large Hadron Collider (LHC) at CERN.
The three innermost layers of the current ITS2 will be replaced by 3 layers of large-scale bent silicon sensor, curved around the beam pipe. The new detector, thanks to a new thinner and closer beam pipe and the reduced thickness of the new sensors and the new configuration, will greatly reduce the material budget. This, together with the greater proximity to the Interaction Point, will allow to dramatically increase the resolution on the impact parameter, radically improving the physics performance of the detector.
In the present work, the performance of an ALPIDE sensor in bent configuration was studied, with the data analysis of a test beam in which the chip was curved down to a radius of 18 mm, corresponding to the closest ITS3 layer to the IP.
Data analysis was carried out in two stages. First of all, the Corryvreckan framework was used to produce some fundamental plots for the analysis starting from the raw files containing the data recorded during the beam test. Moreover, Corryvreckan has also been modified at the source code level to update the new bent geometry and to define further new histograms useful for the final analysis, to be produced by the framework. Once the output files with the updated version of Corryvreckan have been produced, a ROOT code framework has been written to intensively analyze the outputs and the plots obtained by Corryvreckan. This program allows to simultaneously analyze several sessions of data, comparing the trend of some observables as a function of specific parameters of the chip, such as the cluster size.

The two main results of the present thesis are the following:

- the trend of the mean of the cluster size distribution has been studied as a function of the charge threshold, resulting in a decreasing trend curve and thus confirming the expectation based on the flat ALPIDE chips behavior.

- the performance of the chip in terms of spatial resolution and efficiency were studied as a function of the cluster size. Both spatial resolution and efficiency have shown promising results. The former showed a trend in accordance with a flat ALPIDE and a minimum value of $\sim 6 \mu$m, slightly higher than the 5 μm

foreseen. The latter has been found higher than 99%, in agreement with the non-bent result.

The results here reported then represent a very first proof of concept of the bent-principle at the core of the ITS3 upgrade.

Appendix A

Silicon detectors

A silicon detector is a semiconductor apparatus which works as a solid state ionization chamber. They are largely used in particle detection thanks, among other characteristics, to their high density and integration, sensitivity, radiation hardness, relatively low production costs. In the following sections, we intend to explore the basic working principles and functionalities.

A.1 Doped Silicon Detectors

Silicon is an element of the fourth group, its **gap energy**[1] is about 1.1 eV at room temperature and in a crystalline structure it forms covalent bonds with four other atoms. Silicon at room temperature has an intrinsic charge concentration of 1.45×10^{10} cm^{-3}; the thermal energy is sufficient to break some bonds and pass electrons in the conduction band of the semiconductor. The excited electron is free to move in the crystal and leaves free a position called *hole* [23].

Silicon, like other semiconductors, can be **doped** (Figure A.1). This is possible by adding it some *impurities*, consisting of atoms with a different numbers of valence electrons. For example, for group IV semiconductors such as Silicon, typical impurities consist usually of elements of group III and V. Depending on the type of impurity used, holes (group III impurities) or electrons will then be added to the crystal. If doped with acceptor atoms, i.e. with a lower atomic number, they are called *p-type* semiconductors; those doped with donor atoms are instead called *n-type* semiconductors.

Therefore, for standard doping levels[2], the charge carriers are mainly due to doping and these are electrons in n-doped crystals and holes in p-doped crystals, respectively.

[1] The *band gap* or *gap energy* of an insulator or (not doped) semiconductor is the energy range that is closed/forbidden to electrons, i.e. the difference between the valence band and the conduction band.

[2] Standard doping levels are of the order of one impurity atom for every $10^6 \div 10^8$ semiconductor atoms.

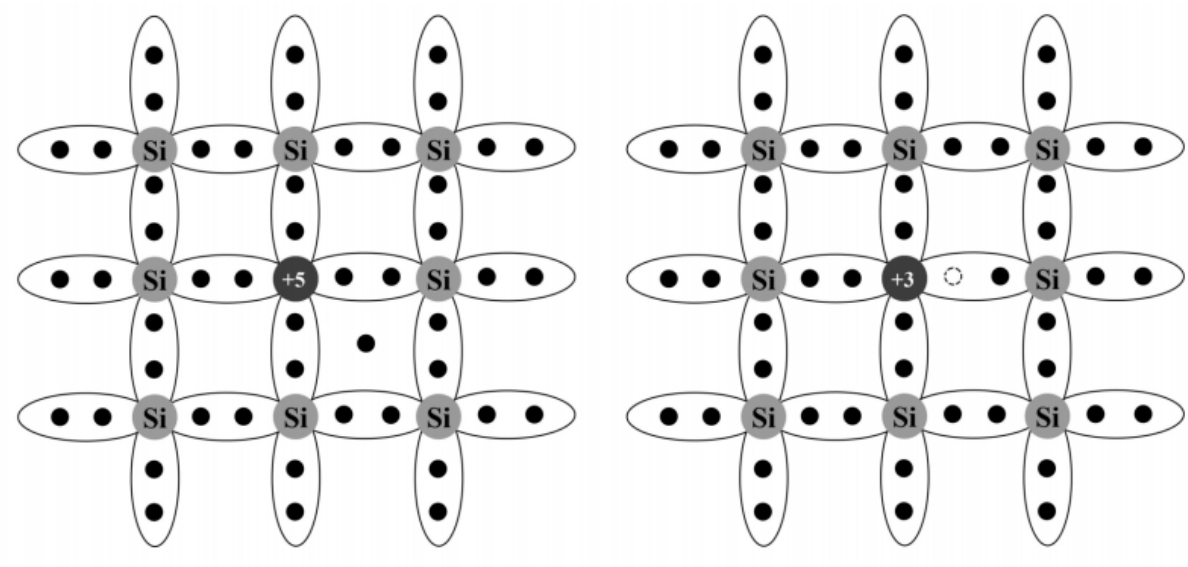

Figure A.1: Left: n-doped Si crystal. Right: p-doped Si crystal.

p-n junction ad I-V characteristic

However, the doping by itself is not sufficient for particle detection, as the signal would be totally obscured by the thermally generated pairs. Since it is difficult to reduce the thermal pairs only by decreasing the temperature, the other way is the **depletion of the silicon volume** from the free charge by applying a reverse bias voltage.

By contacting a p-doped semiconductor and an n-doped semiconductor, a new structure is formed, called *p-n* junction. The difference in electron and hole concentrations near the junction triggers a spontaneous current of electrons from the n-type to the p-type region and holes in the opposite direction. After passing into the region in which they are a minority, they recombine with the present majority carriers, leaving positive charges in the n region and negative charges in the p region (due to the presence of ions of the atoms used for the doping) and creating what is called **depletion region** (Figure A.2). Therefore, an electric field is generated in the region of the junction; the process stops when this becomes strong enough to prevent the motion of the majority charges between the two regions. Typically, the depletion region with the isolated p-n junction is about $10^{-2} \div 1\mu$m thick.

When applying an external voltage V_{bias}, the depletion region and the junction potential barrier increase or decrease depending on the polarization (direct or reverse bias operation).
A silicon detector works in **reverse bias** operation mode, thus the V_{bias} applied to the *n* side of the junction is larger with respect to the *p* one. Therefore, the potential barrier gets higher and the depletion region is wider. The total voltage is given by:

$$V = V_{bias} + V_{bi} \tag{A.1.1}$$

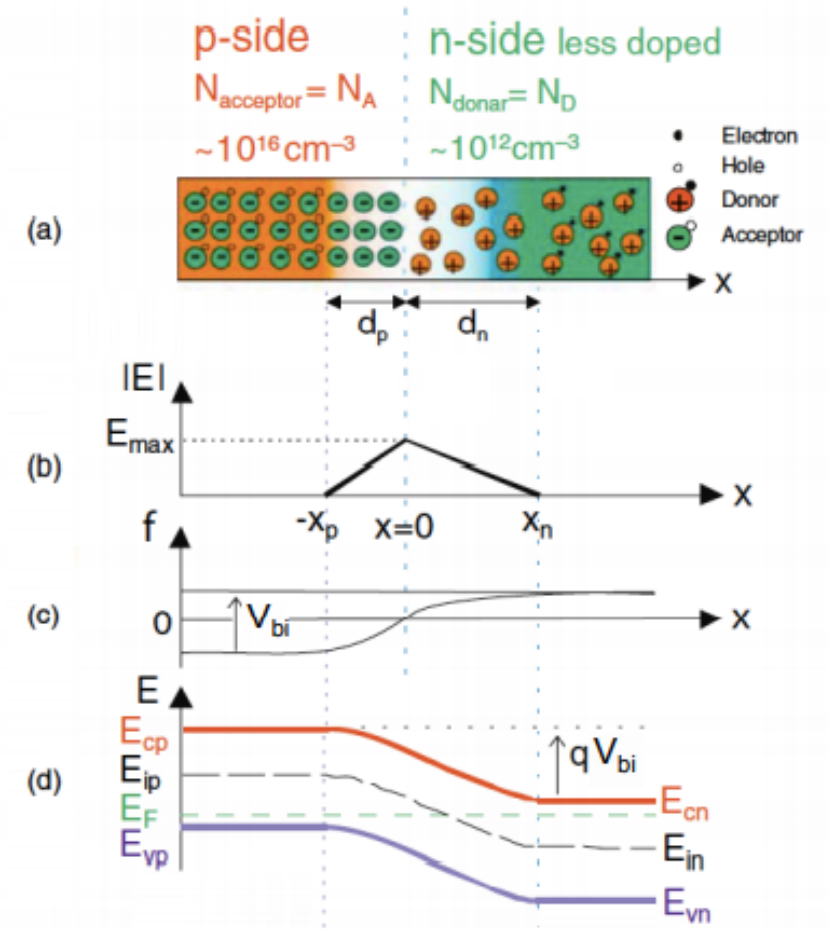

Figure A.2: From above to bottom: (a) scheme of the atomic configuration of the *p-n* junction, (b) the relative *E* field and (c) the corresponding potential. (d) represents the band configuration at the junction equilibrium.

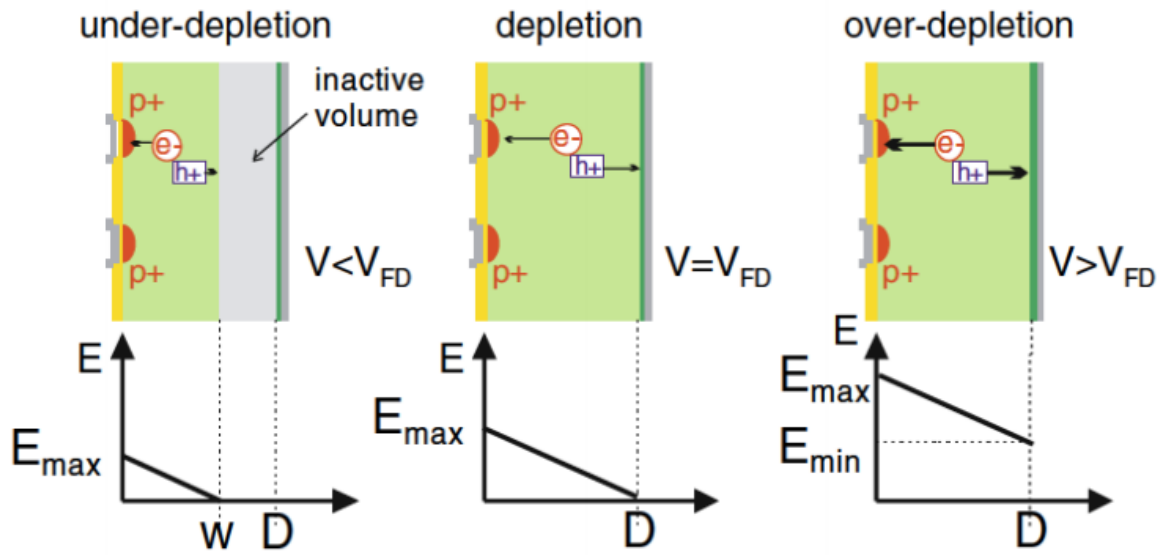

Figure A.3: Representation of the E field and the depletion region given different values for V_{bias} with respect to V_{FD}. Figure from [24].

where V_{bi} is the *built-in* voltage of the semiconductor[3].

The **characteristic** curve of a *p-n* junction shows the trend of the current as a function of the applied voltage to the ends of the junction in the I-V plane. The study of the characteristic of a device allows to predict its operation in a certain application context. In Figure A.4 the characteristic of a Silicon diode in the reversed bias region is shown. The right region is characterized by a sharp increase in the current due to the presence of an electric field so intense as to generate pairs of charge carriers in an uncontrolled manner due to the Zener effect or avalanche production. By increasing the reverse bias voltage too much, the junction is compromised irreversibly.
The trend of the current I as a function of the voltage V in the regions outside of the Breakdown in an ideal junction, is described by the Shockley equation:

$$I = I_m(e^{V/\eta V_T} - 1) \tag{A.1.2}$$

where I_m is the *inverse saturation current* (i.e. the current generated by the minority carriers created within the junction), η is a constant called *ideality factor* and V_T is the thermal voltage (25 - 26 mV at 300 K).

Si detectors and charged particle interaction

The characteristics of doped semiconductors and the ability to create electron-hole pairs with very low energy injections make them particularly suitable in the field of particle detection. Consider a portion of a doped semiconductor immersed in an elec-

[3]In case of $N_D \sim 10^{12}$ cm^{-3} and $N_A \sim 10^{16}$ cm^{-3} doping concentrations, $V_{bi} \sim 0.5$ V.

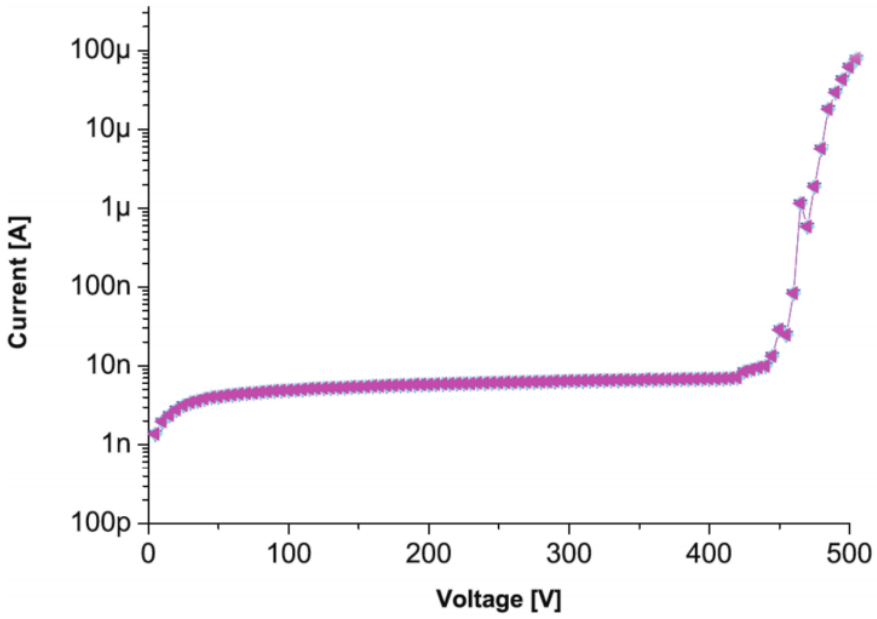

Figure A.4: Characteristic curve of a Si diode in the reversed bias region. Current and voltage are shown in absolute values. Figure from [24].

tric field like in Figure A.5; as the particle passes through the crystal, it will release a certain amount of energy to the electrons it encounters in its path, making them pass in the conduction band. A certain number of electron-hole pairs will therefore form which, under the action of the electric field, will generate a measurable current. The presence of majority charge carriers, however, makes the process inefficient due to the rapidity with which recombination occurs. If, on the other hand, an reverse biased p-n junction is used, in the depletion region there are no majority charge carriers, this can therefore be used as a sensitive area.

The width W of the depletion region is given by the following expression:

$$W = W_p + W_n = \sqrt{\frac{2\epsilon}{e}(\frac{1}{N_A} + \frac{1}{N_B})V} \tag{A.1.3}$$

and considering then the typical case with $N_A >> N_D$[4], the previous equation becomes:

$$W \simeq W_n \simeq \sqrt{\frac{2\epsilon V}{eN_D}} = \sqrt{2\epsilon V \rho \mu_e} \tag{A.1.4}$$

where ϵ represents the absolute dielectric constant of the semiconductor, e is the elementary charge, N_A and N_D density of acceptor and donor atoms in the doped crystals, V the total voltage, ρ the resistivity of the material and μ_e the mobility of the electrons. By increasing the reverse bias voltage up to a value V_{FD}, the depletion

[4] At least by one order of magnitude.

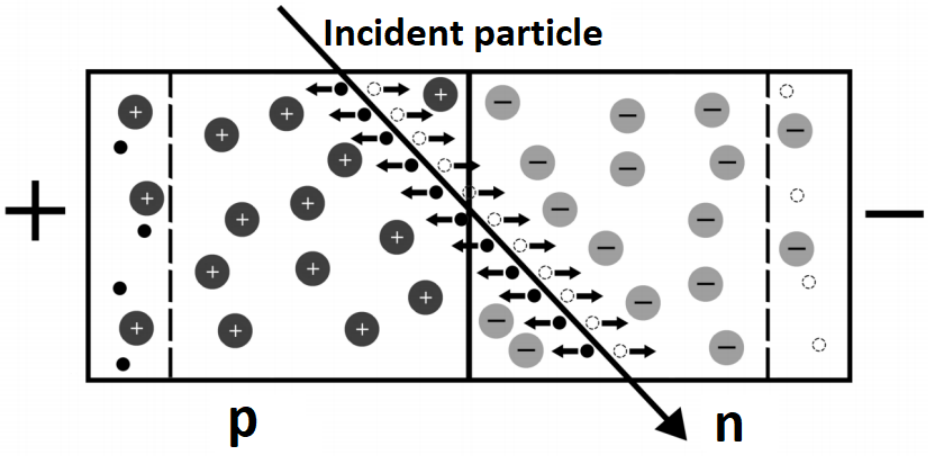

Figure A.5: Interaction between a ionizing particle and a reverse biased p-n junction.

region increases until it occupies the entire junction (full depletion region condition). The voltage V_{FD} required to reach the fully depleted junction with thickness d is given by:

$$V_{FD} = \frac{qd^2}{2\epsilon\mu\rho} \tag{A.1.5}$$

When the bias voltage is higher than V_{FD}, the overbias voltage $V_{bias} - V_{FD}$ adds by consequence an offset $E_{field} = V_{overvoltage}/d$. The **signal** in a detector of this type can be described with the Shockley-Ramo theorem [25]. The theorem states that the current induced by the motion of the charge q on the single electrode k is described by:

$$I_k(t) = -q\vec{v}(x) \cdot \vec{E}_k(x) \tag{A.1.6}$$

with $\vec{v}$ velocity of the charge q and $\vec{E}_k$ the weighting field obtained by setting the potential of the *k-th* electrode to 1 and the other to 0. In the approximation of a detector as a flat-faced capacitor, the density of the field lines on the electrodes depends on the position of the particle.

References

[1] The ALICE collaboration, *The ALICE experiment at the CERN LHC*, vol. 3, 2008, S08002, DOI: 10.1088/1748-0221/3/08/S08002.

[2] ALICE Collaboration, *Technical Design Report for the Upgrade of the ALICE Inner Tracking System*, tech. rep., 2014.

[3] John W. Harris and Berndt Müller, *The Search for the Quark-Gluon Plasma*, vol. 46, 1, Annual Reviews, Dec. 1996, pp. 71–107, DOI: 10.1146/annurev.nucl.46.1.71, URL: http://dx.doi.org/10.1146/annurev.nucl.46.1.71.

[4] The ALICE collaboration, *The ALICE TPC, a large 3-dimensional tracking device with fast readout for ultra-high multiplicity events*, vol. 622, 1, 2010, pp. 316–367, DOI: https://doi.org/10.1016/j.nima.2010.04.042, URL: https://www.sciencedirect.com/science/article/pii/S0168900210008910.

[5] P Cortese, *ALICE Time-Of Flight system (TOF): addendum to the Technical Design Report*, Technical design report. ALICE, Geneva: CERN, 2002, URL: http://cds.cern.ch/record/545834.

[6] *ALICE Time-Of-Flight system (TOF): Technical Design Report*, Technical design report. ALICE, Geneva: CERN, 2000, URL: https://cds.cern.ch/record/430132.

[7] The ALICE Collaboration, *Performance of the ALICE experiment at the CERN LHC*, vol. 29, 24, 2014, p. 1430044, DOI: 10.1142/S0217751X14300440.

[8] The ATLAS Collaboration, *The ATLAS Experiment at the CERN Large Hadron Collider*, vol. 3, 08, 2008, S08003–S08003, DOI: 10.1088/1748-0221/3/08/s08003, URL: https://doi.org/10.1088/1748-0221/3/08/s08003.

[9] The CMS Collaboration, *The CMS experiment at the CERN LHC*, vol. 3, 08, 2008, S08004–S08004, DOI: 10.1088/1748-0221/3/08/s08004, URL: https://doi.org/10.1088/1748-0221/3/08/s08004.

[10] Luciano Musa, *Letter of Intent for an ALICE ITS Upgrade in LS3*, CERN-LHCC-2019-018. LHCC-I-034, Geneva, Dec. 2019, URL: https://cds.cern.ch/record/2703140.

[11] P. Yang et al., *Low-power priority Address-Encoder and Reset-Decoder data-driven readout for Monolithic Active Pixel Sensors for tracker system*, vol. 785, 2015, pp. 61–69, DOI: https://doi.org/10.1016/j.nima.2015.02.063, URL: https://www.sciencedirect.com/science/article/pii/S0168900215002818.

[12] D.A. van den Ende et al., *Mechanical and electrical properties of ultra-thin chips and flexible electronics assemblies during bending*, vol. 54, 12, 2014, pp. 2860–2870, DOI: https://doi.org/10.1016/j.microrel.2014.07.125, URL: https://www.sciencedirect.com/science/article/pii/S0026271414003278.

[13] Magnus Mager, *The LS3 upgrade of the ALICE Inner Tracking System based on ultra-thin, wafer-scale, bent Monolithic Active Pixel Sensors*, Dec. 2020, URL: https://indico.cern.ch/event/813597/contributions/3727803/.

[14] Corrado Gargiulo, *Space Frame and Cold Plate Characterization*, URL: https://indico.cern.ch/event/518710/.

[15] B. Abelev et al., *K^0_S and Λ Production in Pb-Pb Collisions at $\sqrt{s_{NN}} = 2.76$ TeV*, vol. 111, 22, American Physical Society (APS), Nov. 2013, DOI: 10.1103/physrevlett.111.222301, URL: http://dx.doi.org/10.1103/PhysRevLett.111.222301.

[16] B. Abelev et al., *Production of charged pions, kaons and protons at large transverse momenta in pp and Pb–Pb collisions at $\sqrt{s_{NN}} = 2.76TeV$*, vol. 736, Elsevier BV, Sept. 2014, pp. 196–207, DOI: 10.1016/j.physletb.2014.07.011, URL: http://dx.doi.org/10.1016/j.physletb.2014.07.011.

[17] Simon Spannagel Morag Williams and Jens Kroger, *Corryvreckan User Manual*, 2020.

[18] *ROOT*, URL: https://root.cern.ch/.

[19] R. Diener et al., *The DESY II test beam facility*, vol. 922, 2019, pp. 265–286, DOI: https://doi.org/10.1016/j.nima.2018.11.133, URL: https://www.sciencedirect.com/science/article/pii/S0168900218317868.

[20] Y. Liu et al., *EUDAQ2—A flexible data acquisition software framework for common test beams*, vol. 14, 10, IOP Publishing, 2019, P10033–P10033, DOI: 10.1088/1748-0221/14/10/p10033.

[21] Miljenko Suljic, "Study of Monolithic Active Pixel Sensors for the Upgrade of the ALICE Inner Tracking System", Nov. 2017, URL: http://cds.cern.ch/record/2303618.

[22] Magnus Mager, *The Telescope Optimizer*, URL: https://mmager.web.cern.ch/telescope/tracking.html.

[23] William R Leo, *Techniques for nuclear and particle physics experiments: a how-to approach; 2nd ed.* Berlin: Springer, 1994, DOI: 10.1007/978-3-642-57920-2.

[24] F. Hartmann, *Evolution of silicon sensor technology in particle physics*, 2009, URL: https://cds.cern.ch/record/1100830.

[25] W. Shockley, *Currents to conductors induced by a moving point charge*, vol. 9, 1938, p. 635.

Ringraziamenti

Ringraziare non è una cosa solita.
Spesso si dà per scontato o ci si dimentica di farlo, presi come siamo dal turbinio dei pensieri e delle mille cose da fare. Ciò che avviene oggi, giunto alla fine del mio percorso di laurea, preme con insistenza affinché io mi fermi un istante di fronte alla grandezza di quanto accaduto negli ultimi anni, durante i quali è avvenuto qualcosa che ha stravolto la mia vita da cima a fondo. É accaduto come incontrando uno sguardo: ricordo nel minimo dettaglio la prima volta, e come è stato tutte le volte dopo. Innumerevoli le sfide della vita che questo Sguardo ha stravolto, le gioie e i dolori che ha stravolto, i desideri che ha compiuto, così come tutti i desideri che ancora rimangono un mistero. Mi piace spesso ripetere e ri-accorgermi che questi passi costituiscono la cosa *meno solita* che mi è accaduta nella vita.

Di fronte al grande miracolo che è stata, ed è tuttora, la mia storia, non posso permettermi di non soffermarmi, fosse anche solo per un attimo, di fronte a tutti i volti amici che in questi anni mi hanno sostenuto e amato: sono il denominatore comune e il segno umanissimo di un unico Volto misterioso e buono che mi ha voluto qui fin dall'inizio. Per questo, sperando di non dimenticare nessuno (perdonatemi in anticipo!), ringrazio uno ad uno:

Agne Campi, perché credevo di conoscere Bologna...poi ho conosciuto te, e ho accettato di ri-stupirmi ancora.
Agne Nanni, perché ci siamo persi di vista ma con la coda dell'occhio la nostra amicizia è sempre lì pronta, con grande serietà.
Agne Pao, per tutto ciò che abbiamo condiviso e condividiamo tutt'ora nel canto e nell'amicizia.
Albi, perché condividiamo la passione per la fisica e per la vita.
Alexander e **Lukas**, per avermi reso partecipe, assieme agli altri, del vostro cammino di ricerca e della vostra passione.
Alvaro, perché cantando mi insegni che servire è amare, e che amare è servire, instancabilmente.
Andre Silvi (La Rumba, Lubamba, Lavagetto...), perché anche se ci sentiamo poco (perché io sono un disgraziato) siamo sempre compagni di cammino.

Annina, perché sai attendere, ascoltare, accogliere e amare i miei piccoli e grandi passi.
Antuan, perché mi insegni a stupirmi delle cose.
Barbara Renzetti, per avermi sgridato e al contempo valorizzato quando era necessario.
Beppe Placucci, per la grande stima e la grande curiosità che ho visto rinascere nel nostro rapporto.
Bianco, perché quando mi hai spronato a continuare Fisica ci hai visto lunghissimo. E per avermi fatto capire che essere un po' nerd non basta, ma serve l'inter-esse per ciò che si studia e l'umiltà di chiedere aiuto.
Bidoz, perché mi vuoi bene e non meriterei nemmeno la metà della stima che tu mi accordi.
Botte, perché non smetti mai di cercarmi e di raccontarmi di te e di ciò che scopri. E per tutto quello che abbiamo condiviso.
Brigno, per avermi insegnato in modo sanguigno ad amare ciò che studio e il posto in cui sono.
Carabo, perché sei amico e padre.
Cardo! Perché mi hai stimato anche quando ero soffocato dal mio nulla. E da lì è fiorito tutto. Grazie bestiaccia!
Catta, per avermi fatto vedere che la vita è una roba pazzesca!
Cave, perché il tuo sì per me rimane misterioso e grande da guardare.
Ceci Fracassi, perché riesci sempre ad accompagnarmi con le tue mille domande.
Cerne, l'uomo dal cuore più grande che io conosca (accorgitene!). Oltre che un grandissimo musicista (accorgetevene, voi altri!).
Chiara Bassani, perché da quando ti conosco sto imparando piano piano a diventare essenziale in ciò che desidero e ciò che faccio.
Ciamma, perché da te imparo la fedeltà vera.
Clari, per avermi insegnato che il mio cammino aveva valore anche se con gli esami non ero al top.
Claudio Chieffo, perché in fondo non te ne sei mai andato!
Cocca, perché quando sei con me sai sempre come colpire nel segno.
Cuca, perché - a tua insaputa - mi hai fatto tanta compagnia in un momento importante della mia vita. E per il rapporto schietto e sincero che è nato con te.
Dima, per avermi insegnato cos'è la vera speranza e perché ti ricordi tutto di me, fino al minimo dettaglio.
Don Emanuele, perché mi hai voluto bene fin da quando sono nato!
Don Enzo, perché la tua sincerità, la tua passione, le tue sgridate e la tua compagnia mi hanno fatto crescere tantissimo.
Don Luca, perché il tuo desiderio di amicizia e la tua stima sono travolgenti.
Don Marco, perché mi sproni a puntare più in alto di quanto io non farei.

Dora, perché mi sei compagna nel cammino per diventare grande.
Ede: il tuo punzecchiarmi mi ha sempre aiutato a crescere!
EleRo, perché il fiorire imprevisto della nostra amicizia è stata la grande scoperta e la grande compagnia degli ultimi mesi.
Elia, perché non ci siamo mai persi di vista ed è sempre chiaro Chi ci tiene uniti ancora oggi, attraverso le sfide della vita.
Eli di Parma, per i primi anni, e anche per avermi accompagnato nei passi degli ultimi mesi. Ah, e per aver tirato un cocomero in testa allo Zazzo.
Le **Famiglie Melandri** e **Falcini**, perché stare con voi **è** essere a casa.
Federica Orlati, per la stima nata durante il liceo e per non aver smesso di accompagnarmi in tutti questi anni.
Flavio Pioppelli, per la pazienza che hai avuto nell'ascoltare e valorizzare le mie incertezze e le mie stupidaggini al pianoforte.
Fra Ferrati, perché se tu non ci fossi, dovrebbero inventarti! Dobbiamo tornare a cantare insieme.
Francesca Carnesecchi, per essere stata la miglior tutor che potessi desiderare, avermi guidato in questi mesi ed essere diventata mia amica.
Franci Mancuso, per la semplicità, la sincerità e la grandezza con cui mi offri la tua amicizia.
Frappa, per aver condiviso con me tanto (anzi, tutto) e avermi insegnato un po' di più cosa sia la pazienza. PS: best chitarrista ever della diaconia 1, ragazzi. Milanesi avvisati.
Gae, per non avermi mai perso di vista in questi anni, nemmeno per un secondo.
Gianpiero Vignola, per aver condiviso assieme un appassionante rush finale!
Gio Rava, perché vederti suonare è roba da matti. Ma suonare con te...è un assaggio del Paradiso come ci è promesso. E grazie anche per tante altre cose!
Giuli Amadori, perché non ci rimediamo mai, ma ci vogliamo bene lo stesso e andiamo sempre al punto.
Giulia Faletti e **Giovanni Campri**, per aver condiviso l'avventura fantastica dello studio assieme.
Giulia Ferrante, perché non hai paura di guardare in faccia ciò che ti sta a cuore.
Graziano Servizi, perché sono certo che ora mi stai proteggendo da lassù, molto più di quanto tu mi abbia cazziato quando eri quaggiù.
Jonj, perché non ti stanchi mai di cercarmi.
Justin, per la compagnia e l'amicizia nate quest'anno (e i dialoghi con bicchierino annesso). Grazie! Firmato: *il Nonno*.
Ila Pomps, perché quando canti tu mi ricordi che Dio esiste, eccome!
Lara, perché sono grato anzitutto di averti ritrovato, sappiamo che non è accaduto per caso. E perché, in fondo, se appartengo al Movimento è proprio grazie a te.

Laura Roncuzzi, per aver servito assieme i ragazzi di Scholé in questi anni.
Laura Zavatti, perché sono troppo grato della sincerità e della grandezza che abbiamo riscoperto nella nostra amicizia.
Lea, per avermi esplicitamente fatto capire che la fatica non è obiezione, ma strada.
Lollo Moretti, perché anche se ogni tanto sparisci sai sempre leggermi dentro come pochi altri.
Luca Cami: che avventura grande la nostra amicizia! Grazie per aver condiviso assieme il servizio del canto nel Movimento in questi anni.
Luca Loreta, per avermi fatto capire che suonando potevo servire il Movimento con tutto me stesso.
Luce, perché se tu non ci fossi il mondo sarebbe veramente un posto tristissimo! E anche per aver costruito insieme in questi anni un pezzettino del Regno di Dio, servendolo col canto e la grande Musica. Grazie.
Lucia Pace, per avermi accompagnato instancabilmente e pazientemente negli anni di liceo.
Mage, perché l'amicizia con te è stata il mattoncino della costruzione di qualcosa di ancora più grande.
Manuel Colocci, perché hai sempre avuto a cuore me, e non solo il mio lavoro di tesi.
Marco Errani, perché mi hai preferito mostrandomi il tuo amore per la conoscenza.
Margherita Mathieu, perché pur essendo io un bambinetto delle medie, a modo tuo mi hai sempre valorizzato e trattato da adulto.
Marti Zava, perché guardandoti agire ho imparato tante cose.
Matte Palmeri, perché mi insegni ad essere me stesso e a tirare fuori ciò che mi sta a cuore.
Mezza, perché sei l'amico che ho sempre desiderato di avere.
Nicolò Jacazio, per avermi fatto capire che la ricerca bisogna sapersela davvero godere, e non è un vuoto spingere sull'acceleratore. Cerchiamo risposte, ma senza dimenticarci che si parte sempre da una domanda.
Nonna Massima, perché continui con passione a tenermi d'occhio da lassù. E mi pare che tu ci stia riuscendo proprio bene.
Nonna Nori, perché nessuno al mondo sa attendermi come sai fare tu, ogni volta, da 26 anni.
Paola Truppi, per avermi insegnato la bellezza del vivere una serietà e una costanza in ciò che si fa. E l'importanza del sacrificio nello studio.
Paolo Valli, per avermi fatto intuire la bellezza della matematica. E per avermi stimato prima ancora di conoscermi.
Peco, per tutto quello che abbiamo condiviso in questi anni nel servizio alla comunità e nella nostra amicizia. E per la tua fantastica pazzia.
Pengu, perché dal preparare un semplice documento pdf può nascere una grandissima

amicizia.
Pippo, perché negli anni hai sempre avuto una attenzione in più per me, e per ciò che abbiamo vissuto assieme. E anche perché sono proprio curioso di vedere cosa accadrà da adesso!
Pier, perché sai guardare la realtà con la giusta leggerezza che ogni tanto io mi perdo!
Pollo, perché da quando sei il capo dei tecnici mi sento un po' della ST pure io. E poi, quanto è bello poter servire assieme qualcosa che si ama!
Richi Barozzi, perché mi insegni cosa vuol dire voler bene donando se stessi con gratuità, stando davanti ai miei mille difetti con ironia e pazienza. E per i dolci della domenica sera. *Alooooora?*
Richi Giurato, per aver invitato la mia voce indisciplinata a seguire e servire una Strada Buona.
Rosario Nania, perché mi dici sempre ciò che pensi con grande disponibilità e pazienza. Unico. Grazie!
Samma, perché mi ricordi quanto è bello essere semplici e sinceri col proprio cuore.
Sanni, perché oltre ad essere una grande amica, sei la mia segretaria preferita!!
Santo, perché quest'anno con te è stato un viaggio veramente appassionante.
Sarona, per aver scritto una Veglia del CLU al posto m... ahem! - avermi aiutato con la Veglia di Natale. E per l'amicizia che c'è sempre stata.
Scan, per avermi fatto riscoprire la grandezza della mia storia.
Smilzo, per tante cose che sai. Ma anche perché, tornando alle origini, offrendomi la tua amicizia mi hai riavvicinato alla musica Vera una volta per tutte.
Sofi, per quella telefonata in cui mi facesti capire che l'inizio dell'università e del CLU mi avrebbe potuto cambiare la vita. Così è stato! E perché in un qualche modo mi hai sempre fatto sentire il cuginetto preferito, in tutti questi anni.
Speedy, perché il giorno in cui ci siamo (ri)trovati il mio cuore ha messo su una festa!
Stefano Calandrini, per avermi fatto compiere i primissimi passi nella musica.
Tommi Mela, per tutto quello che abbiamo condiviso e per la serietà e l'ironia che ogni volta hai nel guardarmi.
Valerio Mugnai perché forse, guardandomi suonare la prima volta, avevi già capito tutto.
Virgi, perché tra un tira e molla e l'altro non hai mai mollato la presa su di me. E te ne sarò grato per sempre.
Zia Rosi, perché senza di te il mondo andrebbe a scatafascio. **Zio Franco**, perché vorrei avere anche solo un centesimo della tua pazienza!
Zia Iulia e **Zio Paolo**, perché non avete mai dubitato di me per un secondo che fosse uno.

Desidero tuttavia rivolgere un ringraziamento ad alcuni di voi in particolare.
Tra di noi, ci sono tanti tipi di amicizie, così come il volto di ognuno di voi mi è caro nella sua unicità e diversità.
Se in particolare desidero ringraziare voi fra tutti, è proprio perché con la vostra presenza siete arrivati a forgiare anche il carattere e il volto dell'uomo che sono ora.
Per questo, ringrazio:

Gilda, perché hai a cuore il mio destino più di quanto non lo abbia io. Sei guida, amica, maestra. Grazie!
Chicco: i perché sarebbero così tanti da scriverci un libro (un libro che farebbe ridere, probabilmente). Il vero grande *perché* è che l'incontro con te ha cambiato tutto.
Mati, perché non ti tiri mai indietro, mi vuoi bene così come sono e mi spingi sempre ad essere sincero e serio col mio cuore.
Ele Mariotti, perché il tuo arrivo quest'anno mi ha scombinato tutte le carte in tavola. Ma proprio tutte. Atomica!
Bronx, (soprattutto) per quella volta a programmare la mia sessione sulla panca a Fisica. E per tutto quello che è accaduto dopo.
Maddi Carmo, perché sei uno dei più grandi regali che abbia mai ricevuto nella vita.
Cate, per non esserti mai risparmiata con me e per avermi sempre voluto bene davvero.
Jack e **TeX**, perché aver condiviso tutto con voi in questi due anni è stato il dono più grande. Si cammina al Destino, mai soli!
Zazzo: potevo, in mezzo a questa squadra di matti, desiderare un compagno di avventura migliore? Nessuno meglio di te! Citava una rima tempo fa: *Messi assieme dalla fisica che indirizzò i lor sentieri, per portarli alla scoperta di sentirsi amici veri!*
Gigi Bernardi, **Marta** e **Ciocca**: la nostra amicizia non va raccontata a parole.
Va cantata!
Gigi Zallio, perché per me sei un fratello. Non serve aggiungere altro.
Mamma, **Babbo** e **Ste**, perché mi insegnate ad amare!

Infine, un ringraziamento speciale va a tutta la comunità del CLU di Bologna, a ognuno degli amici lì incontrati, e a chi in questi anni l'ha guidata, perché questa vita sostiene e permette concretamente il passo che compio oggi.
In particolare, desidero ringraziare chi con me è stato partecipe di alcuni luoghi che mi hanno costruito come uomo: innanzitutto, tutti coloro che hanno condiviso con me la tavolata (quando ancora si poteva) di Sala Acquaderni. Poi, la comunità di Scienze, il Coro *Beatae Virginis*, la Segreteria e i Tecnici, e ultimamente persino (!) i CP. Chi ha dato e dà le sue forze per servire questa vita incontenibile, anche chi conosco meno, è responsabile, e spero anche partecipe, con me, della gioia che vivo oggi.
Grazie di cuore a tutti!